INVESTIGATION OF FEED LINE EFFECTS ON FIELDS FROM BROADBAND OVER POWER LINE COMMUNICATIONS

A Dissertation

Presented to

the Faculty of the Department of Electrical & Computer Engineering

University of Houston

In Partial Fulfillment

of the Requirements for the Degree

Doctor of Philosophy

in Electrical Engineering

by

Anthony Lau

December 2013

INVESTIGATION OF FEED LINE EFFECTS ON FIELDS FROM BROADBAND OVER POWER LINE COMMUNICATIONS

Anthony Lau

Approved:

Chair of the Committee
Dr. David R. Jackson, Professor
Electrical & Computer Engineering

Committee Members:

Dr. Stuart A. Long, Professor
Electrical & Computer Engineering

Dr. Donald R. Wilton, Professor
Electrical & Computer Engineering

Dr. Ronald H.W. Hoppe, Professor
Mathematics

Dr. Lowell T. Wood, Professor
Physics

Dr. Suresh K. Khator
Associate Dean of Graduate Programs
Cullen College of Engineering

Dr. Badrinath Roysam
Department Chair and Professor
Electrical & Computer Engineering

Acknowledgements

My profound gratitude to the committee members involved with the dissertation and in supporting an environment conducive to creativity. I am thankful to Drs. Stuart Long, Ronald Hoppe, and Lowell Wood for participating in the dissertation committee and for their perspectives throughout the process. Dr. Donald Wilton not only has my thanks for his time on the dissertation committee, but also for the many discussions that formed the basis in some of the approaches taken to address specific technical issues. I am grateful for the counsel and inspiration by Dr. David Jackson. His support made possible the privilege of my arrival at this point as well as the good fortune to be associated with members of the Applied Electromagnetics Laboratory.

At this moment, I wish to note the appreciation I have of my aunts, uncles, and cousins as well as members of the Applied Electromagnetics Laboratory for their kindness and support. Further, I would like to recognize the Gates Millennium Scholars Program for its significant role in facilitating my pursuit of higher education. The journey to this point may not have been practical without their assistance.

The following work is dedicated to my parents. I would not have had such an opportunity without the dedication they have been placing so many years ago in building toward such a moment.

INVESTIGATION OF FEED LINE EFFECTS ON FIELDS FROM BROADBAND OVER POWER LINE COMMUNICATIONS

An Abstract

of a

Dissertation

Presented to

the Faculty of the Department of Electrical & Computer Engineering

University of Houston

In Partial Fulfillment

of the Requirements for the Degree

Doctor of Philosophy

in Electrical Engineering

by

Anthony Lau

December 2013

Abstract

With the advent of broadband over power line (BPL) for high-speed data transmission and the emerging interest in grid modernization, the appeal of signal transmission on a power line above the earth is significant. One important issue is the nature of the fields in the vicinity of the power line, since regulatory agencies (such as the FCC) place restrictions on the field level. Models used in previous studies have yet to include the influences of the feed lines that carry the radio-frequency currents from the electronics to the power lines. In the present work reported in this dissertation, the field surrounding the feeding structure and power lines over an earth is examined. Different feeding methods and earth models are used in the investigation, ranging from very simple to more sophisticated. In the simplest approach, the earth is modeled as a perfect conductor, and image theory is used. A more sophisticated approach uses the spectral domain immittance method to account for the finite conductivity of the earth. Results allow for the identification of the mechanisms involved with the field emission as well as a determination of the maximum power level of a BPL source that will meet existing FCC guidelines.

Table of Contents

List of Figures

List of Tables

Chapter 1

Introduction

In March 2004, a technology agenda to diversify the availability of broadband carriers was released by the White House that spurred the deployment of broadband over power line (BPL) technology. Its promise lies in the prospect that it will promote "economic productivity and offer life-enhancing applications, such as distance learning, remote medical diagnostics, and the ability to work from home more effectively" [1]. Based on the concept of a competitive market, the agenda noted that an increase availability of choices in the broadband market would bring forth cost-effective world-class quality broadband service. This is evident with the emerging prominence of 3G, WiMax, 4G, and LTE. However, such technologies typically operate around urban centers with growing bandwidth consumption. Thus, BPL remains a viable low-cost option in providing broadband access to rural locations and additional urban bandwidth.

With the June 2011 White House grid modernization initiative [2], BPL has gained a part in the development of a clean-energy economy. The general concept is that a clean-energy economy needs real-time energy and asset management as well as operation capability, which Smart Grid may provide. In September 2010, the IEEE-SA Standards Board approved IEEE Std 1901-2010 [3] noting the role of BPL in Smart Grid networks. Hence, BPL supports the advancement of a clean-energy economy by enabling integration of remote renewable energy sources in rural locations to urban centers [4] while reducing load on existing urban bandwidth consumption.

Amidst all the appeal of BPL, the primary issue with the technology revolves around the fields emitted. For example, the American Radio Relay League (ARRL) is

concerned with BPL deployment due to "its high potential for causing interference to radio communication" [5]. Another aspect regarding BPL emissions involves IEEE Std 1775-2010 that covers testing and measurement methods of BPL equipment for EMC requirements. It was mentioned by ARRL in January 2011 that "the IEEE Standards Board approved publication of the standard over the technical concerns of the SDCom" [6], which is part of the IEEE EMC Society. There was also the matter of "lacking an unambiguous scientific basis for a single value that would be equally valid across the entire frequency range from 1.7 to 30 MHz" in regards to the "extrapolation factor for measuring emissions at distances other than 30 meters from the power line" [7]. Beyond ARRL, other entities potentially affected by BPL emissions include the U.S. Coast Guard (e.g., distress and safety communications), U.S. Customs Border Protection (e.g., over-the-horizon enforcement network), U.S. Department of Defense (e.g., over-the-horizon radar systems), and radio astronomers, [8] since there is overlap in the operating frequencies. Radio astronomers are particularly susceptible since their instrumentation is specialized to have sensitivity that exceeds typical communication and radar equipment in order to detect the minute signals from celestial sources.

Given the potential impact surrounding BPL emissions, an examination of the electric field emitted by a BPL source on feed and power lines is performed. An investigation into some of the basic physics involved in these emitted fields is also presented herein.

1.1 Background

BPL systems are basically using a technology that overlays radio frequency (RF) signals on transmission lines designed for electrical utility frequencies. BPL operates

across a band from 2 to 30 MHz [9] for its orthogonal frequency-division multiplexing modulation while power distribution operates around 50 or 60 Hz (60 Hz in the U.S.). Since BPL uses power lines as its waveguiding structure, the broadband signal is essentially being transmitted on a structure intended for a lower frequency that differs by several orders of magnitude and is typically not shielded. Aside from the emission characteristics of being a non-enclosed waveguide, the feed lines that connect the signal source device to the power lines have the potential to be effective field emitters given that their physical lengths are comparable to a wavelength. Due to the fact that BPL is classified to be a current-carry system under the FCC part 15 unlicensed devices regulations [10], the primary mode should be electrical conduction rather than radiation. Hence, the BPL emission produced may cause corresponding interference issues as well as complication with regulatory restrictions.

Indications of such concerns include studies that had been performed from a wire antenna perspective [11]-[13], which existed before the 2004 technology agenda. In an instance after the technology agenda, high-level technical considerations in implementing BPL [9] was discussed but was based on analysis that used direct application of transmission line theory. Another research had investigated the leakage radiation characteristics through a simulation software package as well as scaled measurements under laboratory conditions [14]. For [11]-[14], the investigator had mainly focused on two horizontally aligned phase lines as the BPL transmission pair, which have the same height above ground. Though their selection of power line arrangement was based on minimizing emissions, BPL venders enable a variety of options [15]-[17]. A few of the possible power line arrangements had been explored in [8]. However, one common

aspect among the studies noted would be that the influences of the feeds carrying the RF signal from the signal source device to the power line have yet to be included. As such, it is the intention of the presented dissertation to take an analytical approach by applying electromagnetic theory to the canonical problem of feed lines exciting power lines over an earth.

1.2 Prelude

The dissertation presented herein exemplifies the impact of the feed line arrangement on the overall emission as well as contributions from the power line. The complexity of the analysis increases progressively along each chapter as the configuration become more specific. However, the ability to demonstrate the impact of various emission mechanisms as a canonical principle is retained throughout. This permits the process to be adaptable to the specifics of any particular BPL installation.

In Chapter 2, the ground work to begin the analysis is performed. The electromagnetic model of various components that compose a BPL system is presented. Such models would translate the effects of the physical hardware into items that can be represented as electrical elements for analytical purposes. Two approaches in modeling the earth are described, where one models the earth as a perfect electric conductor (PEC) while the other models it as a semi-infinite region with a finite conductivity as well as a permittivity. The configuration of a practical 12 kV delta tangent utility pole is noted to enable embodiment of the different emission mechanisms involved with a BPL system.

In Chapter 3, the component models are applied to give rise to BPL system models. Five principle connection arrangements are noted, each as an individual case, based on the selected 12 kV delta tangent utility pole. The technique involved with

minimizing reverse propagating currents along the truncated power lines is also described. Emission by the five cases, as well as the process used in obtaining their respective currents, is discussed. From the emitted fields, it is shown that the fourth case would most likely be in conflict with FCC regulations and is therefore selected for a more involved analysis. A listing of input currents for each case allows the power level needed for compliance with FCC to be obtained, which are all below 20 μW at 3 MHz and 0.5 μW at 30 MHz.

In Chapter 4, the identified particular case (case 4) is extended into a multiconductor system and used to find the transmission and feed line currents on the complete system. The modeling and extraction of space-wave and traveling-wave currents along the power lines from the collected data is explained. The results illustrate the benefit in analyzing the currents separately. The minimal effect of the extra (passive) conductors in the multicondutor system with regards to the input power limits for compliance with FCC is noted.

In Chapter 5, effects due to a finite-conductive earth and the presence of a receiving system are explored to illustrate these effects. The first scenario presented will be a system where only the transmitter circuit exists, as in previous chapters, while the second scenario has a transmitter circuit on the utility pole along with receiving circuits on two separate poles. A comparison between earth models is shown where one assumes that the earth is a perfect electric conductor (PEC), as in previous chapters, while the other relaxes the assumption and allows for the earth to have a finite conductivity. The existence of standing wave currents and increased radiation due to the presence of the receivers and the finite-conductive earth, respectively, will be evident.

Conclusions are presented in Chapter 6 along with some final thoughts. Though each of the previous chapters does close with a section discussing the significance of their respective results, the perspectives in this chapter are collective across chapters and integrated. Remarks are made regarding the reasons in viewing a BPL system as a collection of dipole and traveling-wave antennas based on the behavior of the currents and corresponding field emissions.

The parameters in the chapters to follow are consistent in their signal frequencies, relative geometric properties between power line and air-earth interface, and polarization of electric field being observed. The select frequencies of interest are 3 and 30 MHz, which generally covers the extreme ranges for a typical BPL system operating at RF frequencies. Unless it becomes apparent that the field trends are abrupt, the tendencies are assumed to be well behaved between the two frequencies. Hence, most of the results are obtained for only the frequencies of 3 and 30 MHz. The earth is considered as flat relative to the power line with the sagging of the wires neglected, and hence is treated as horizontal. In accordance with FCC measurement guidelines [8], the vertically polarized electric field would be the component observed. It is anticipated that these parameters are sufficient to understand the basic physics and behavior of the fields as well as to establish a worst-case bound.

Figure 1.1 portrays the concept using a single power line conductor in order to illustrate the basic coordinate system. The actual system studied is more complicated, since it involves the modeling of a realistic structure. Note that the top view includes the lines of observation (30 meters horizontally away from the nearest power line) where the FCC regulation of 30 μV/m had been specified (hereinafter as "FCC lines"). For the

purpose of illustration, Figure 1.2 is an illustration of power lines on an overhead utility pole. The actual pole selected for the analysis herein is shown in Chapter 2.

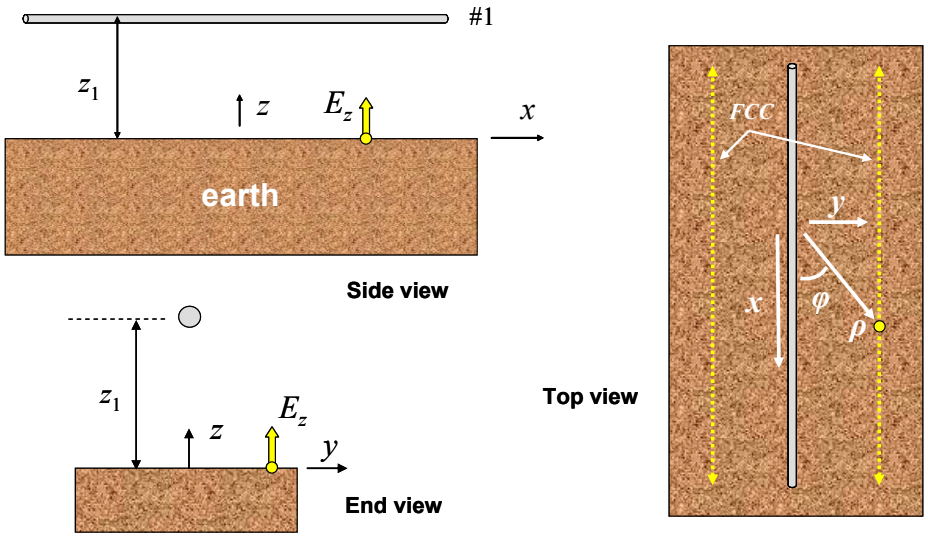

Figure 1.1 Concept of a canonical model for the physical system under investigation with an adopted coordinate system. A single power line conductor is shown for illustration purposes.

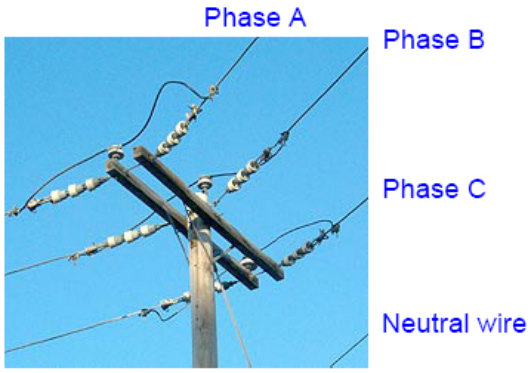

Figure 1.2 An example of a set of power lines that may be seen on an overhead pole.

Chapter 2

Modeling the Components

This chapter describes the electrical modeling of the physical components in order to construct a BPL system model from which analyses can be performed. From an equipment perspective, a BPL system is very straightforward, this being an aspect of the technology's appeal, and consists of a handful of components. In general, it is essentially a BPL device mounted on a utility pole linked to power lines via specialized connectors. Thus, the physical components involved would be the following:

- The earth, which the utility power lines are suspended over
- Wires that compose the power lines as well as the feed lines that carry the RF signal to the power lines
- BPL couplers that connect the feed lines to the power lines
- A BPL device that is composed of the electronics that makes up the transmitting and receiving RF circuits
- The utility pole that supports the power lines and on which the device is mounted.

Each of the sections in this chapter notes the modeling of a particular component and appears in the order as listed.

2.1 Earth Model: Horizontal and Vertical Currents

The next sections present the two approaches for modeling the emitted fields due to a given current above the earth. In accordance with the various possible orientations of the conductors and associated currents that could exist in a BPL system model, each earth model contains a method to address the horizontal and vertical directed components of

the current. To illustrate, Figures 2.1(a) and 2.2(a) would directly correspond to the "end view" of the horizontally-directed line shown in Figure 1.1, while Figures 2.1(b) and 2.2(b) correspond to that of a vertical directed conductor. With interest in the vertically polarized electric field, and given the coordinate system of Figure 1.1, the relevant field component E_z is discussed. The following are the parameters used in Figures 2.1 and 2.2 as well as throughout the study:

- (x, y, z) = coordinate of the observation point
- (x_i, y_i, z_i) = coordinate of the electric current
- $\rho_x = \sqrt{(y - y_i)^2 + (z - z_i)^2}$
- $R = \sqrt{(x - x_i)^2 + \rho_x^2}$

2.2 Earth Model: PEC

In modeling the earth as a PEC, the analysis simplifies through the use of image theory [18]. The excitation will be either a horizontal or vertical directed current that correspond to the orientation of the respective conductor. In applying image theory, the physical model involving a horizontal power line shown in the "end view" of Figure 1.1 can be represented as shown in Figure 2.1(a) while Figure 2.1(b) is for vertically-directed wires, with the $z = 0$ plane serving as the PEC earth boundary.

The simplification in being able to use image theory lies with the ease in finding the scattered fields due to the earth, which can be done by taking the fields produced from the currents on the image conductor. For the horizontal currents shown in Figure 2.1(a), the circle above the boundary represents the physically existing power line conductor, while the circle below is the equivalent mirrored conductor due to the use of

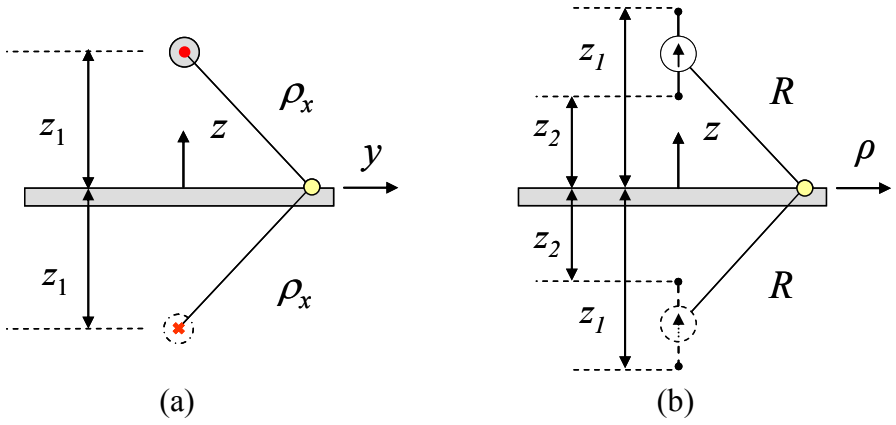

Figure 2.1 End view of the earth model for (a) horizontal and (b) vertical directed conductors, with associated image currents after applying image theory.

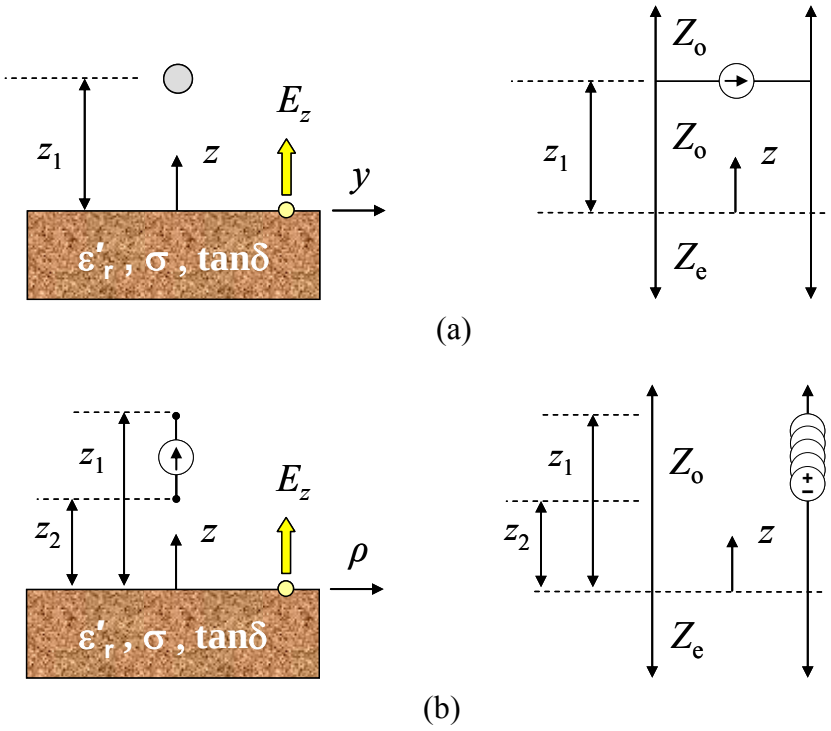

Figure 2.2 End view of the physical system with finite σ earth and corresponding transverse equivalent network (TEN) model for spectral wave components of (a) horizontally-directed currents and (b) vertically-directed currents.

image theory. The scattered fields from the earth in the region on and above the earth would be the free-space fields produced from the image conductor located at $z = -z_1$. The total field at and above the earth for this scenario is found from the superposition of the two fields, one from the physical line current and one from the scattering due to the earth (i.e., from the image current). The same approach applies for the vertical component of current shown in Figure 2.1(b). Should a horizontal and vertical component appear in a given BPL system model, the total field can be found as the collective sum due to the individual physical and image currents.

The E_{ρ_x} field component in accordance with Figure 2.1 for a TM_x wave field [19] (as would be produced by an *x*-directed horizontal electric current) may be expressed in terms of the magnetic vector potential $\psi = A_x$ as

$$E_{\rho_x} = \frac{1}{j\omega\varepsilon}\frac{\partial}{\partial\rho_x}\frac{\partial}{\partial x}\psi \ . \tag{2.1}$$

Direct geometric relations would give the E_z field component as

$$E_z = \frac{(z - z_i)}{\rho_x}\frac{1}{j\omega\varepsilon}\frac{\partial}{\partial\rho_x}\frac{\partial}{\partial x}\psi \ , \tag{2.2}$$

where the general solution for the magnetic vector potential of an arbitrary *x*-varying horizontal line current [19] would be

$$\psi = \frac{1}{j8\pi}\int_{-\infty}^{+\infty} \tilde{I}(k_x)\, H_0^{(2)}\left(k_{\rho_x}\rho_x\right) e^{-jk_x x} dk_x \ . \tag{2.3}$$

The function $\tilde{I}(k_x)$ is a spatial 1D Fourier transform (in the *x* coordinate) of the current, $H_0^{(2)}$ denotes the zero-order Hankel function of the second kind, and

$$k_{\rho_x}^2 = k^2 - k_x^2 \ , \tag{2.4}$$

with k being the wavenumber of the medium surrounding the BPL system (i.e., air).

Should the system model involve vertically-directed currents, the E_z field component for a TM_z wave field [19] (as would be produced by a z-directed vertical electric current) may be expressed in terms of the magnetic vector potential $\psi = A_z$ as

$$E_z = \frac{1}{j\omega\varepsilon}\left(\frac{\partial^2}{\partial z^2} + k^2\right)\psi \ . \tag{2.5}$$

The general solution for the magnetic vector potential of an arbitrary z-varying vertical segment of current along $z_2 \le z_i \le z_1$ can be viewed as the accumulated effect of a continuous distribution of infinitesimal dipoles, and can thus be expressed as

$$\psi = \frac{1}{4\pi}\int_{z_2}^{z_1} \frac{I^{vert}\left(z_i\right)}{R} e^{-jkR} dz_i \ , \tag{2.6}$$

with $I^{vert}\left(z_i\right)$ being the vertical dipole current at $z = z_i$ specific to the system model.

To obtain the vertical field from any horizontal directed segment of current, coordinate transformation can be applied on

$$E_\rho = \frac{1}{j\omega\varepsilon}\frac{\partial}{\partial\rho}\frac{\partial}{\partial z}\psi \tag{2.7}$$

and Equation (2.6) along with direct geometric relations. Thus, the total field from a collection of variously oriented currents can be found via superposition where any given integral is performed numerically.

2.3 Earth Model: Finite Conductivity

Relaxing the assumption that the earth is a PEC and modeling the earth as a finite-conductive semi-infinite region entails the use of the spectral domain immittance (SDI) method [20] to solve for the fields produced by wires over the earth. As such, the physical system can be viewed as a multilayer media that is excited by either a horizontal or vertical current, which provides a good framework for the analysis. One of the benefits of this analysis is that the region representing the earth can be assigned a finite conductivity and a relative permittivity to reflect, to some degree, the actual characteristics. The physical model shown in the "end view" of Figure 1.1 is modeled as illustrated in Figure 2.2(a) in the SDI method, while Figure 2.2(b) portrays the modeling of a segment of vertically-directed conductor, with the $z = 0$ plane representing the earth boundary. The circle above the boundary in Figure 2.2(a) represents the physically existing horizontal power line conductor above the semi-infinite region. The σ and ε_r' for the earth region are 0.1 S/m and 8, respectively, yielding a loss tangent (tanδ) [18] of 74.9 at 3 MHz and 7.49 at 30 MHz.

The general form of the E_z field component for an arbitrary x-varying horizontal surface current is given from SDI analysis [20] as

$$E_z = \frac{1}{(2\pi)^2} \int_{-\infty}^{\infty} \int_{-\infty}^{\infty} \frac{1}{\omega\varepsilon} k_x \tilde{J}_{sx}\left(k_x, k_y\right) I_i^{TM}\left(k_\rho, z, z_i\right) e^{-j\left(k_x[x-x_i]+k_y[y-y_i]\right)} dk_x dk_y \quad . \qquad (2.8)$$

The function $\tilde{J}_{sx}\left(k_x, k_y\right)$ is a spatial 2D Fourier transform (in x-y coordinates) of the surface current corresponding to either a horizontal line or segment of current, while $I_i^{TM}\left(k_\rho, z, z_i\right)$ is a transmission-line term that propagate the fields from z_i to z (detailed in Chapter 5), where

$$k_\rho^2 = k_x^2 + k_y^2 \ . \tag{2.9}$$

For an arbitrary z-varying vertical segment of current along $z_2 \le z_i \le z_1$, the E_z field component would be

$$E_z = \int_{z_2}^{z_1} \frac{-I^{vert}\left(z_i\right)}{2\pi\left(\omega\varepsilon\right)^2} \int_0^\infty J_0\left(k_\rho \rho\right)\, I_v^{TM}\left(k_\rho, z, z_i\right)\, k_\rho^3 dk_\rho dz_i \ , \tag{2.10}$$

with a derivation given in Appendix A. The function J_0 denotes the zero-order Bessel function, $I_v^{TM}\left(k_\rho, z, z_i\right)$ being a propagation term (detailed in Chapter 5), and $I^{vert}\left(z_i\right)$ is the vertical current as defined previously in relation to Equation (2.6).

Thus, the total field from a collection of various currents that are either horizontal or vertical can be found via superposition. Note that the spectral-domain integrals performed numerically.

2.4 Wires

With the next main constituent of a BPL system being the wires that compose the power and feed lines, this section presents the modeling of wires in relation to the current that they conduct. Figure 2.3 shows a small segment of wire as a scaled representation to illustrate the concept, which is applied to the power and the feed line wires.

Since the interest is in observing fields outside of the wire, it would be advantageous to be able to represent the radially-distributed current along the wire as a filament current positioned along the wire axis. This can be accomplished by application of the equivalence principle [19], assuming that the current is symmetric around the circumference of the wire. The skin depth, δ , can be calculated by

$$\delta = \frac{1}{\sqrt{\pi f \mu \sigma}} \ . \tag{2.11}$$

For the frequencies of 3 and 30 MHz, the skin depth is less than 50 μm for both aluminum ($\sigma \approx 3.5 \cdot 10^7$ S/m) power lines and copper ($\sigma \approx 6 \cdot 10^7$ S/m) feed line wires. With a power line radius of 1.13 cm and feed line radius of 0.512 mm (typical values), it is evident that the currents are essentially surface currents. These may be collapsed with good approximation to the wire axis. Hence, it is reasonable to proceed in modeling the wires as filaments of current.

As previously mentioned, the equivalence principle enables the use of filament currents in place of the wires. The process starts, as portrayed in Figure 2.3(a), with the wire itself, which contain currents that may have a radial distribution illustrated in Figure 2.3(c) as a close-up of the cutaway view in Figure 2.3(b). Seeing as the currents basically reside near the surface (δ < 50 μm with wire radius > 0.5 mm), it can be represented by an equivalent surface current, Figures 2.3(d) and (e), that produces an equivalent electric field at and outside of the wire radius. Applying the equivalence principle, the wire itself could be exchanged with the surrounding medium, Figure 2.3(f), as long as the equivalent surface current remains. Should the effects due to the finite conductivity of the wire be significant, an equivalent surface resistance could be incorporated as part of the wavenumber. Nonetheless, it is shown in Appendix B that the conductivity of the wires is sufficient to treat them as PEC. Invoking the equivalence principle once more, the surface current can be substituted by an equivalent filament current, Figure 2.3(g), as long as the electric field at and outside of the wire radius is preserved. Thus, filament

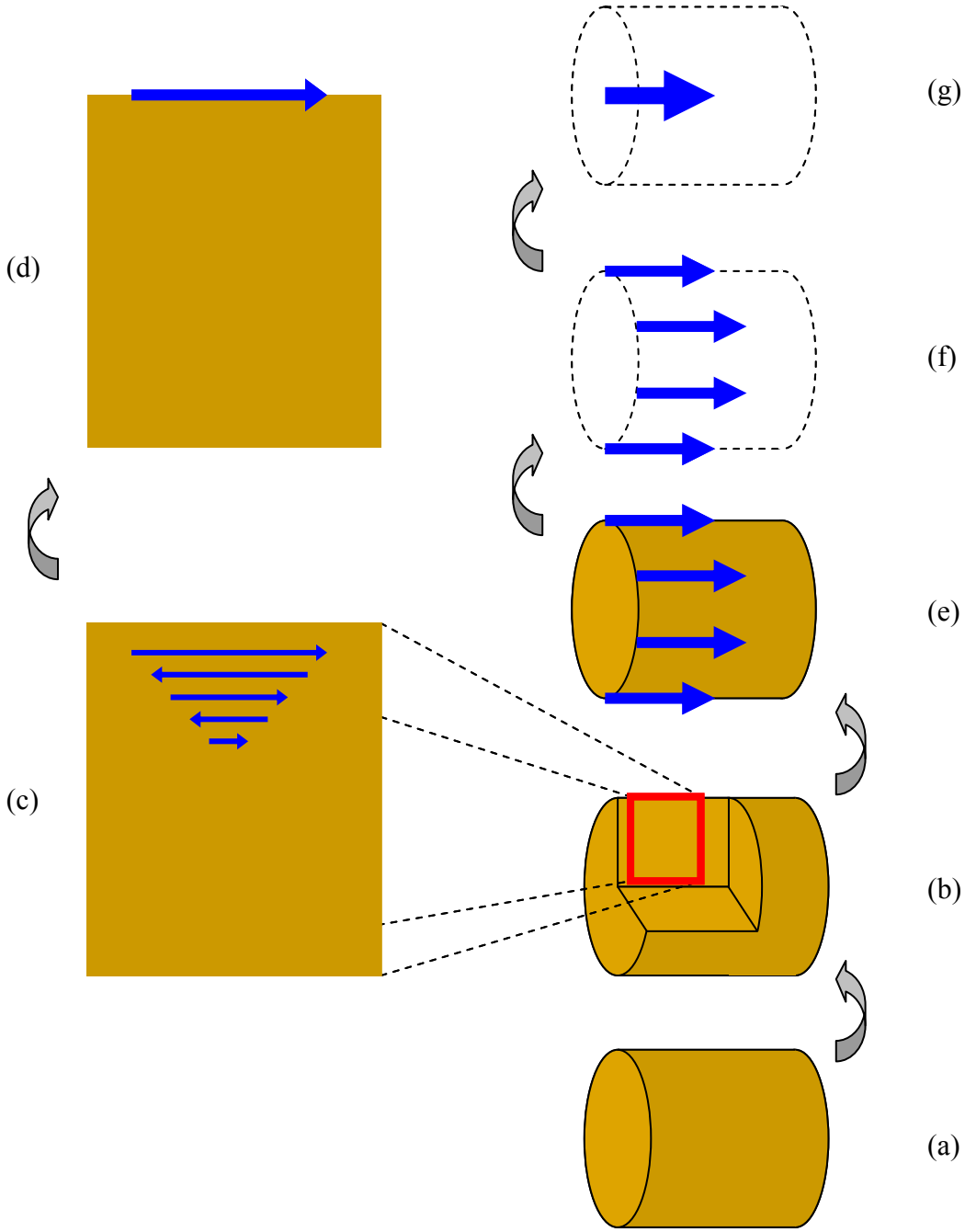

Figure 2.3 Progression of wire model. (a) Small segment. (b) Partial cutaway. (c) Radial distribution. (d) Equivalent current at outer radius. (e) Surface current. (f) Hollow tube current. (g) Filament line current along wire axis.

currents are used to represent the currents on the finite radius wires when calculating emitted fields.

2.5 Couplers

BPL couplers are the sole interface between the feed and power lines and the modeling of two types is presented in this section. The first type is a capacitive coupler, which is connected inline to the feed line conductor wires. Though not required, it is likely that capacitive couplers are used in pairs to transfer RF signals to the power lines. The second is an inductive coupler, which is connected to a pair of feed line conductor wires forming a coaxial cable or a twisted pair. It is possible to use one inductive coupler to transfer RF signals to any of the power lines. Figures 2.4 and 2.5 illustrate a capacitive and inductive coupler along with their circuit models, respectively.

(a)

(b) (c)

Figure 2.4 Example of (a) a capacitive coupler as well as the (b) general and the (c) approximate equivalent model.

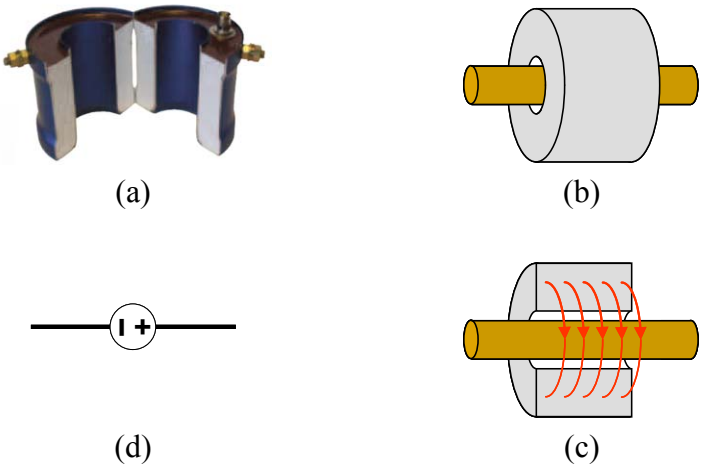

Figure 2.5 Example of (a) an inductive coupler as well as (b) an illustration of the coupler installed on a wire and (c) the associated magnetic field. The coupler can be represented as (d) an inline voltage source.

A capacitive coupler as shown in Figure 2.4(a) from [16] operates as an inline capacitor between the power line and one end of a feed line conductor. Shown in Figure 2.4(b), any RF current that enters the coupler would pass through the hardware with minimal attenuation while presenting a high impedance element at the power frequency (e.g., 60 Hz). Given proper design, which shall be assumed, the high-frequency attenuation should be negligible and thus it is treated as an RF short, where the physical contact point to the power line become an electrical junction. The described model is portrayed in Figure 2.4(c).

An inductive coupler, like the clamp in Figure 2.5(a) from [16], operates as an inline voltage source along the power line. The inductive coupler clamps onto the power line as illustrated in Figure 2.5(b). Fed by either a coaxial cable or a twin lead, the RF current is converted into magnetic fields, as shown in Figure 2.5(c). This in turn acts as

an inline voltage source to excite the RF current along the power line, as shown in Figure 2.5(d).

2.6 BPL Device

All the component models discussed thus far assume the existence of an RF signal current, and this section presents a model of the device from which the excitation originates. Figure 2.6(a) from [17] depicts a BPL device having an enclosure in which the transmitting and receiving electronics reside that typically have preconfigured connector terminals.

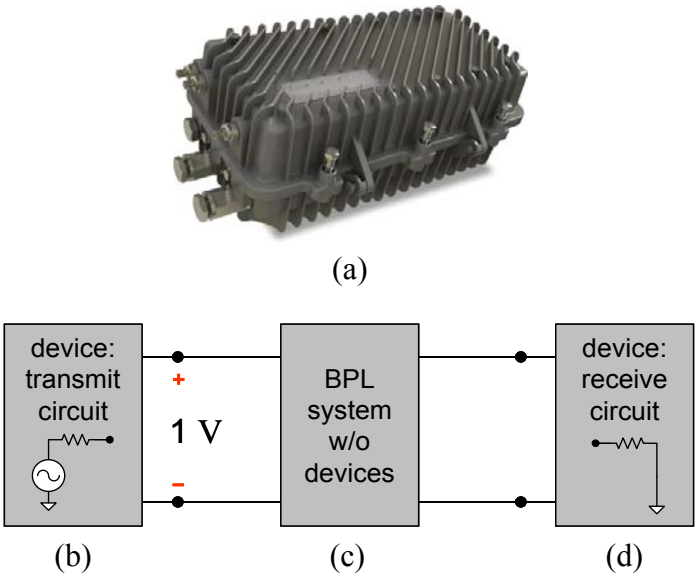

Figure 2.6 Example of a (a) packaged BPL device as well as the device model when (b) transmitting a 1V signal across the (c) BPL waveguiding system to another device that is (d) receiving the signal.

Relative to the wavelength of the signal, the device and associated terminals are quite small and can be treated as lump elements. Exemplified by [17], each dimension of the hardware is less than 50 cm (i.e., less than 0.05 λ_o). As perceived by fields external to the device, it is essentially a lump element. Naturally, the device terminals are smaller

than the device itself. This makes the separation between the conductors for a given terminal adequately small to view the device, when transmitting, as an ideal gap source from the perspective of the other model components, as shown in Figure 2.6(b), while being a lumped load impedance when receiving, as shown in Figure 2.6(d), the signal guided by the various conductors being represented by Figure 2.6(c). Since it is anticipated that the specifics of the device electronics do not directly affect the emitted fields, it is sufficient to model only the terminal properties. Hence, the entire device can be treated as a black box, being either an ideal gap source or load (as needed by the system model). This model is general enough to represent the device of any manufacturer.

2.7 Pole Model

A discussion of the utility pole is presented in this section. With the vast amount of venders, contractors, and utility company specific guidelines, there are numerous pole arrangements available. However, the "12 kV delta tangent pole" configuration by CenterPoint [21], shown in Figure 2.7, provides a good frame to embody the principles of the various emission mechanisms that could exist on a given BPL system. Although this particular pole configuration is henceforth assumed throughout this work, the general conclusions that are reached should apply to other pole configurations and not be limited to any particular site or installation.

Since the utility pole suspends the power lines along with supporting the feed lines and BPL device above the earth, it contains the geometry information to enable analyzing different BPL excitation arrangements. From Figure 2.7, geometry estimates were made as shown in Table 2.1 using the coordinate system of Figure 1.1 with the

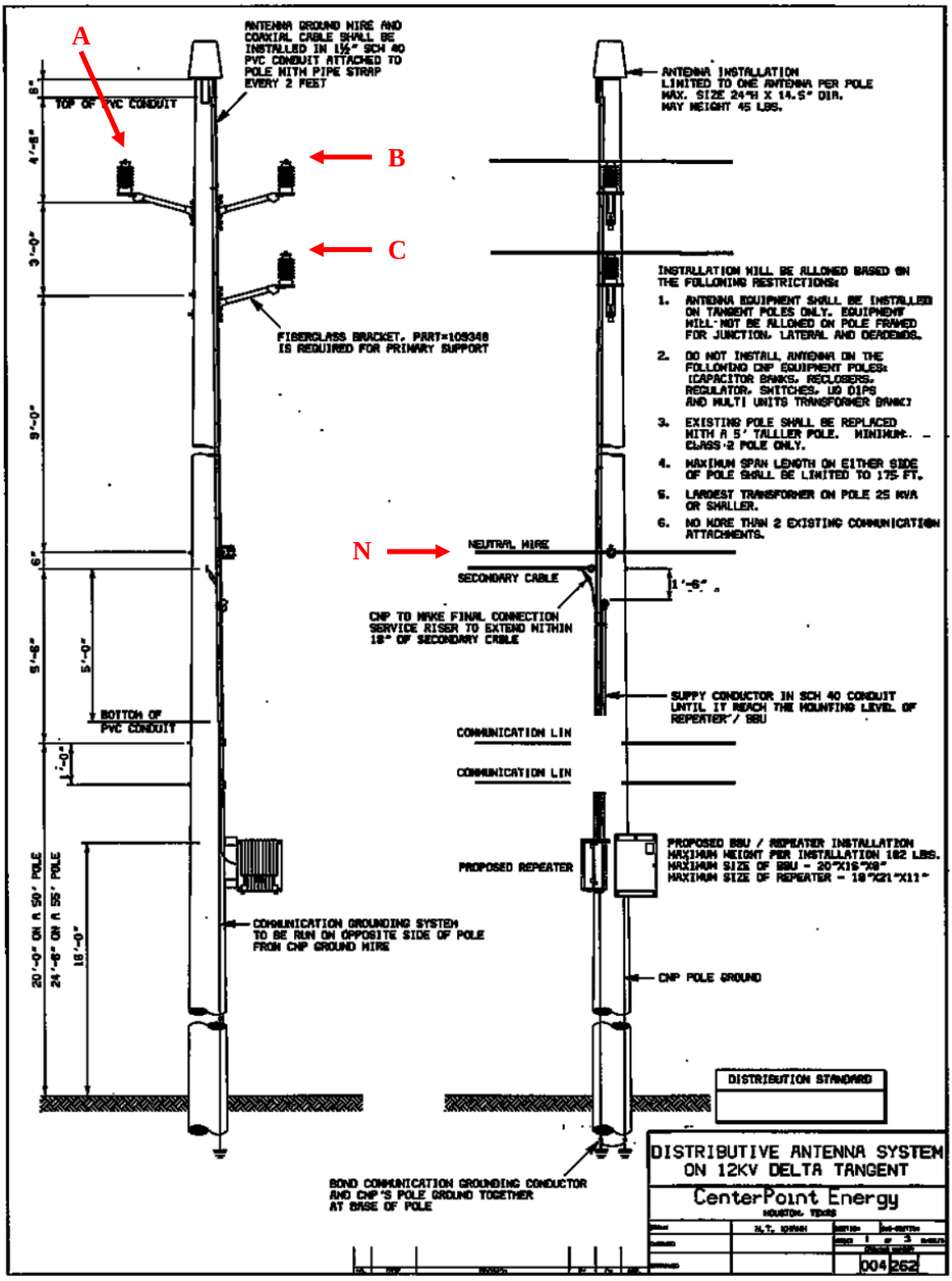

Figure 2.7 Configuration of the 12 kV delta tangent pole used with deployment of antenna systems.

Table 2.1 Wire coordinates (in meters). The estimation is based on Figure 2.7.

@ $x = 0$	Neutral (N)	A	B	C
y	0.1186	-0.7959	0.7959	0.7959
z	7.9248	12.0224	12.0224	11.1080

origin at the center of intersection between the earth and the base of the utility pole. The labeling of the phase lines is arbitrary, being only for referral purposes. In regards to the utility pole itself, the geometry suggests that it is composed of concrete and so is modeled as a 15.24 meter cylindrical dielectric rod with ε_r' between 4.6 and 4.75 for a water-to-concrete volume ratio of 0.2% [22]. At and below 30 MHz, such a rod would propagate fields similar to free space [23], thereby having minute effect on the emitted fields. The power line wires are taken as free-standing lines with anticipation that the fiberglass brackets do not significantly affect the emitted fields. As alluded to in the figure, it is assumed that the neutral wire is connected to the pole grounding wire.

2.8 Summary

A summary of the chapter is presented in this section. The main concepts portrayed in this chapter are as follows:

1) Physical components that constitute a BPL system are the earth, wires, couplers, devices, and the utility pole.
2) For a PEC earth, image theory along with superposition permits the use of simple radiation theory in free space, while the SDI method is needed to address a finite-conductive earth.

3) Wires with current are represented as filamentary line currents when observing the field at or beyond the wire radius.
4) Capacitive couplers are RF shorts while Inductive couplers are ideal inline voltage sources.
5) BPL devices are represented as ideal gap sources and load impedances when transmitting and receiving, respectively.
6) The configuration of the 12 kV delta tangent utility pole provides the geometry information needed for modeling BPL systems studied here, while the pole itself does not significantly affect the emitted fields between 3 MHz and 30 MHz.

Chapter 3

Modeling the System

This chapter describes the modeling of BPL systems that are based on the utility pole configuration and available coupler options. With two types of couplers, four power lines, and earth, there are numerous options in feeding the RF signal from the device to the power lines. However, they can be generally categorized into five principle methods of connecting the device to the power lines and exemplified respectively as individual cases. Since power lines that carry the RF signal are part of a very large grid, the effects from line truncation on the signal current are addressed in order to leverage a practical single cell approach to performing the analyses. For the scenario herein, the BPL cell would be a segment of the power lines that are in proximity to a device above the earth. The currents are observed with the use of software packages that are based on the electric field integral equation (EFIE) method of moment (MoM) technique [24] while the fields are obtained from the methods discussed in Chapter 2.

3.1 Feed Line Cases

As mentioned, there are many ways to feed the RF signal onto power lines given the available physical components, but they can be characterized into five principle methods of feed arrangement as presented in this section. From simply being a single inline voltage feed to the more involved vertical and horizontal phase-phase, phase-neutral, or phase-earth feeds, each case has merits in application, and thus is considered. Since the utility pole itself and associated fiberglass brackets would not significantly

affect the emissions, they are not included in the models. Figure 3.1 portrays the five cases.

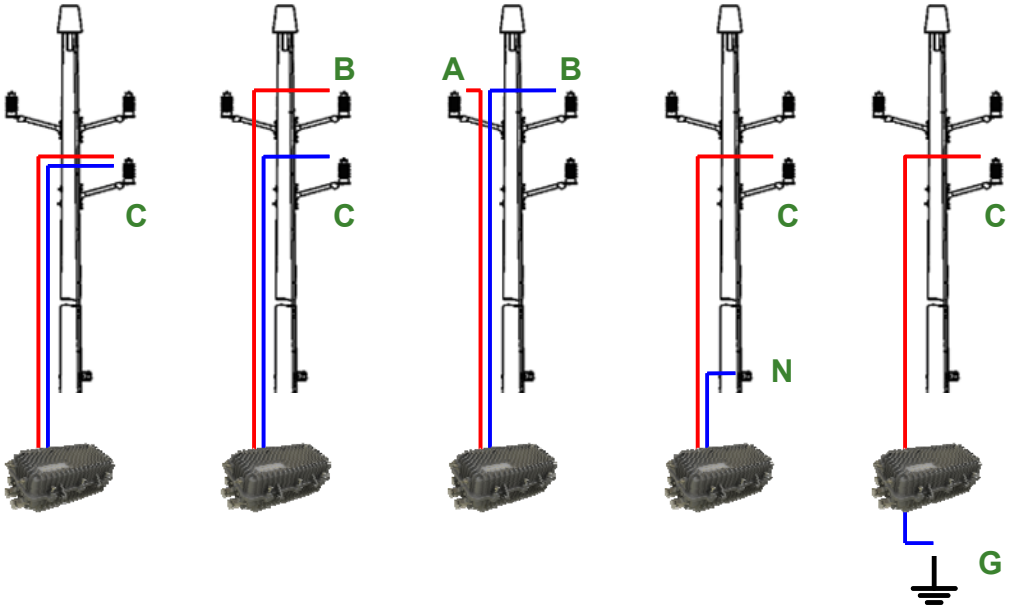

Figure 3.1 Examples comparing the principle feed methods from (a) case 1 through (e) case 5.

The first feed case is an inline voltage feed, shown in Figure 3.1(a), which represents the use of a single inductive coupler, and so could be economically appealing. Though the coupler could be installed on any of the four utility conductors, wire C would be the least emitting option, having the lowest height from earth among the phase wires. As can be seen in Figure 3.2(c), both conductors (i.e., red and blue) from the device terminals would be about the same length and follow about the same path toward the power line. Hence, any field from one feed line current (e.g., red) would be effectively cancelled by the other current (e.g., blue).

Given such a feed pair along with the component models from previous chapter, the device terminal can be translated to the power line where the inductive coupler

resides without affecting emissions. Should the feed pair be a coaxial cable, it is anticipated that the currents along the horizontal power line does not induce significant currents along the vertical cable's exterior surface of the outer conductor and, accordingly, this is not included in model. This reduces the analysis to the fields due to an ideal inline gap source along wire C over the earth as portrayed in Figures 3.2(a) and 3.2(b).

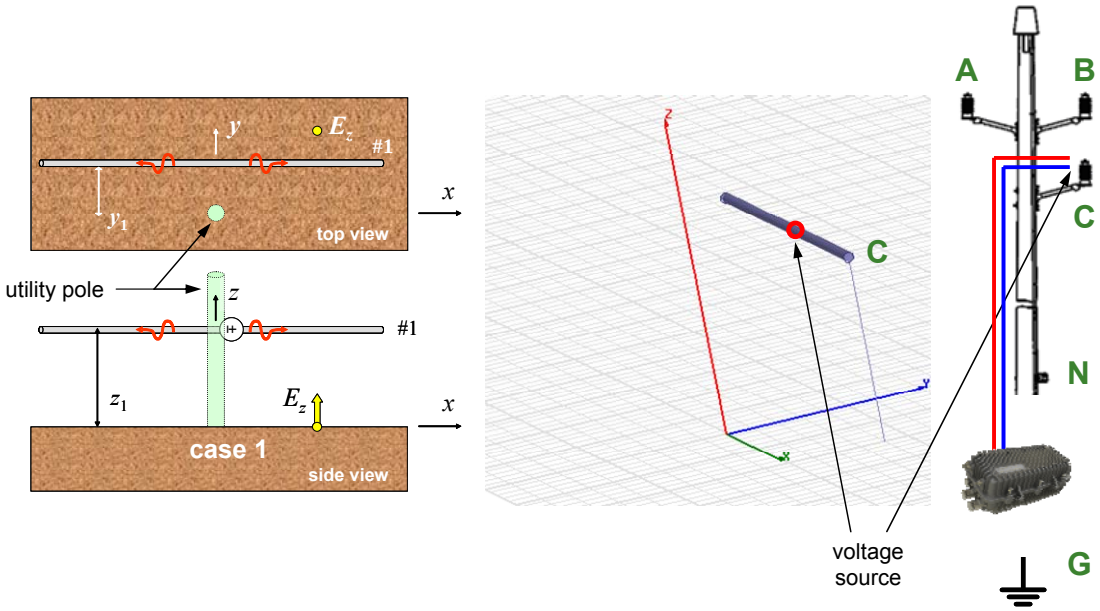

Figure 3.2 Concept of canonical model with (a) top and side as well as (b) 3D perspective views for (c) case 1 feed. Note that the utility pole is included for reference purposes only and is not part of the model.

The second feed case is a vertical phase-phase (B-C) feed, Figure 3.1(b), where feed line effects below wire C are minimal and represents the use of a capacitive coupler on each of the two phase wires. Given the small separation distance between wires B and C, this pair of wires forms a good transmission line pair. Figure 3.3(c) shows that both conductors from the device terminals up to wire C height are about the same length and

follow about the same path. Thus, up to the wire C height, it is similar to case 1 where any fields due to one conductor from the BPL source would effectively cancel the other and hence the device terminal can be translated along the feed pair without affecting the emissions. However, the remaining feed line conductors that travel from wire C to B will emit fields that do not cancel and so this part of the feed wiring is included in the model. This feed situation is depicted in Figures 3.3(a) and 3.3(b) with the red circle being the gap source, wire B being power line 1, and wire C being power line 2.

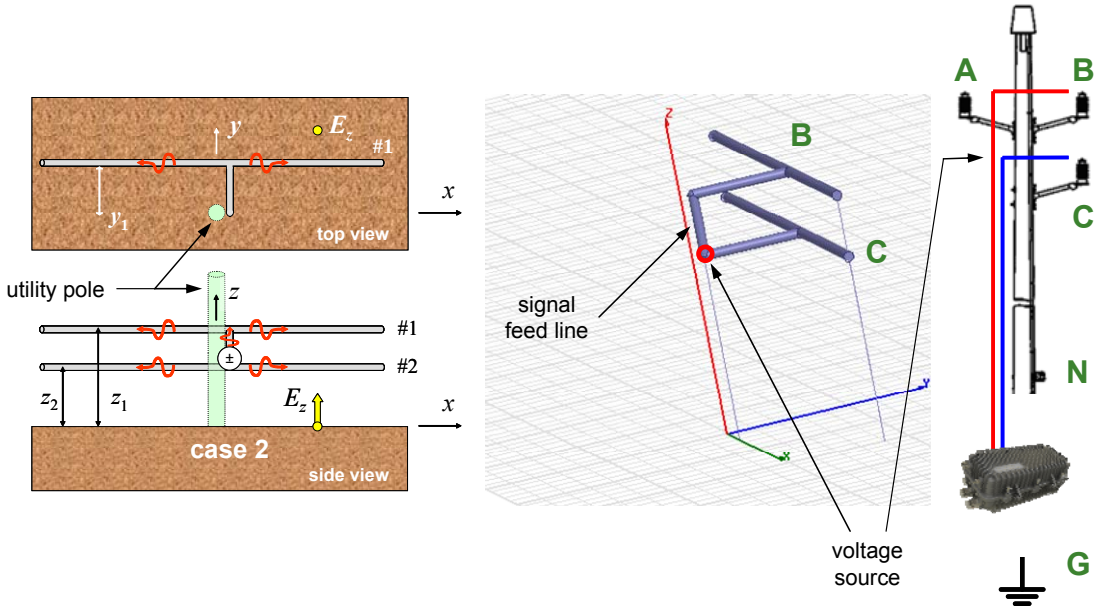

Figure 3.3 Concept of canonical model with (a) top and side as well as (b) 3D perspective views for (c) case 2 feed.

The third feed case is a horizontal phase-phase (A-B) feed, shown in Figure 3.1(c), where feed line effects below wire A or B are minimal and good geometric symmetry suggest that the wire currents would be similar to a balanced transmission line. As shown in Figure 3.4(c), both conductors from the device terminals to wire A or B height are about the same length and follow about the same path. Like case 2, field cancellation

from the two feed wires would occur below wire A and the device terminal can thus be translated. The remaining feed line wires that then capacitively couple to wires A and B would emit fields that do not cancel and, hence, these wires are included in the model. The setup is depicted in Figures 3.4(a) and 3.4(b) with wire A as power line 2 and wire B as power line 1.

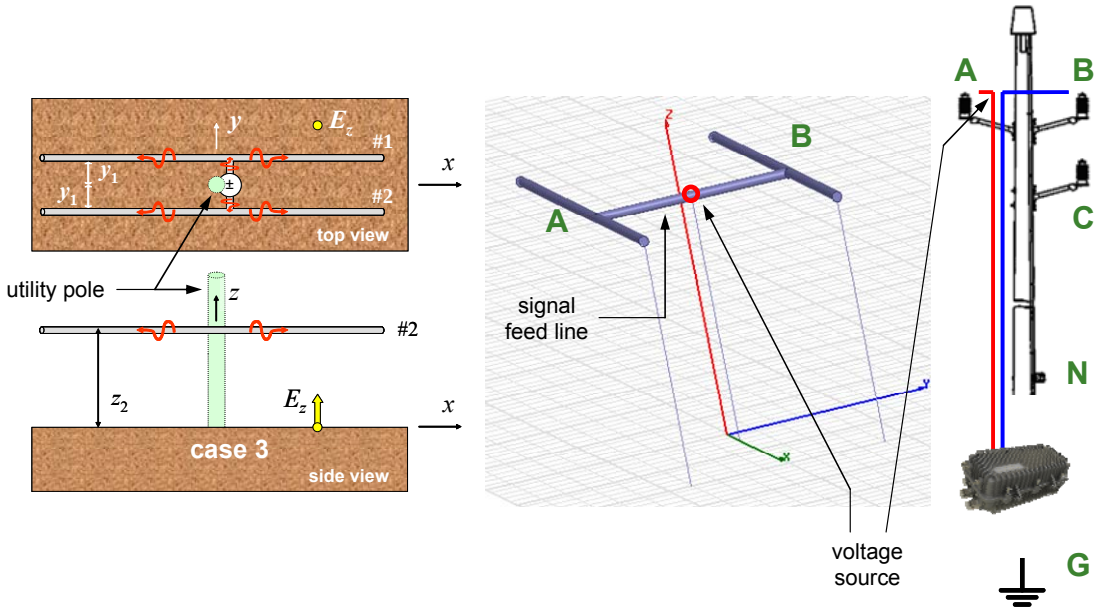

(a) (b) (c)

Figure 3.4 Concept of canonical model with (a) top and side as well as (b) 3D perspective views for (c) case 3 feed.

The fourth feed case is a phase-neutral (C-N) feed, Figure 3.1(d), where feed line effects below the neutral are minimal. In this case only one capacitive coupler is required, as the fed line that is connected to the neutral wire can be connected directly. This could be economically appealing. Given the similarity of Figure 3.5(c) and Figure 3.3(c) of case 2, the device terminal is translated up to the neutral wire height and only the remaining feed line conductors above the neutral wire are included in the model. Furthermore, the utility pole grounding wire is connected to the neutral and, being

unpaired and electrically long it needs to be included as part of the model. Note that the grounding wire is on the direct opposite side of the utility pole from the feed line pair. Figures 3.5(a) and 2.5(b) illustrate the scenario with wire C as power line 1 and the neutral wire as power line 2.

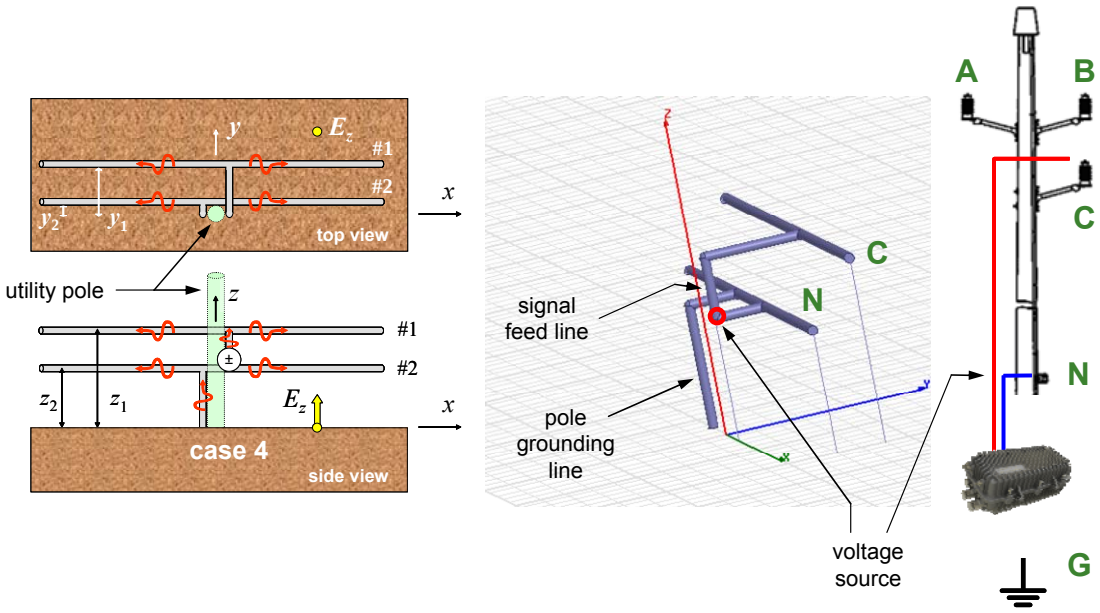

Figure 3.5 Concept of canonical model with (a) top and side as well as (b) 3D perspective views for (c) case 4 feed.

The fifth feed case is a phase-earth (C-G) feed, Figure 3.1(e), where feed line effects are evident in comparison to the previous configurations, but this would correspond to the simplest installation, involving only one capacitive coupler and a direct connection to ground. Unlike any of the prior cases discussed, Figure 3.6(c) shows that the two feed line conductors coming from the BPL source does not share any common route, meaning there is little chance in cancellation of field from the feed pair. Consequently, the entire feed line conductor pair is included in the model and the device terminal remains at the initial height. This feed situation is portrayed in Figures 3.6(a)

and 3.6(b) with wire C as power line 1, the neutral wire as power line 2, and the device height z_{src} of 4.88 meters is estimated from the repeater location in Figure 2.7.

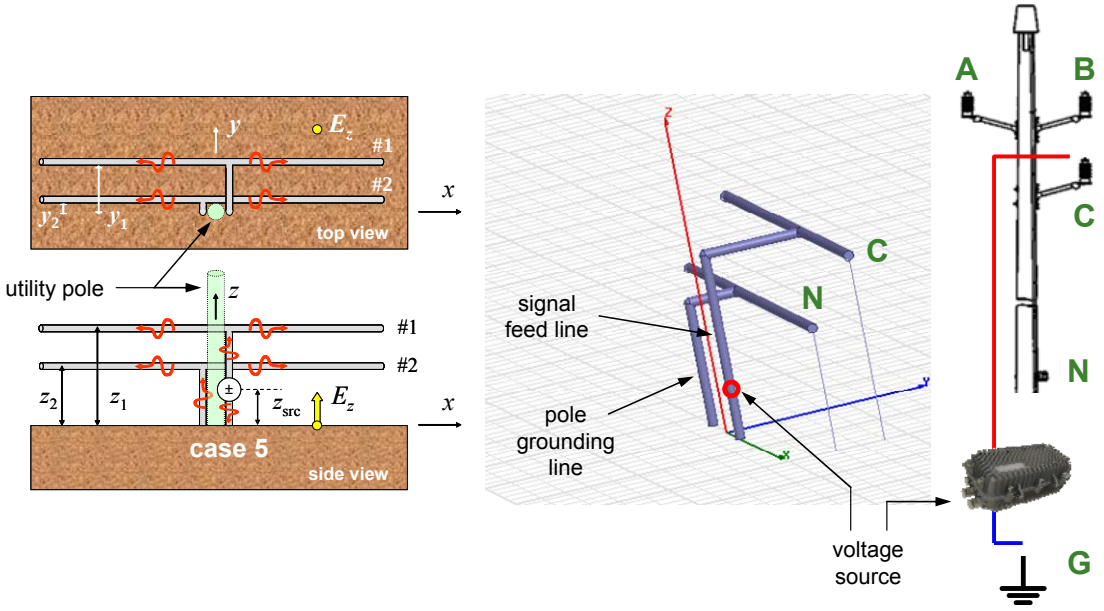

Figure 3.6 Concept of canonical model with (a) top and side as well as (b) 3D perspective views for (c) case 5 feed.

3.2 Line Truncation

In this section, a technique to minimize the reverse propagating current due to truncated power lines is presented. Either in a simulation or physical measurement environment, it is more practical to treat a small section (canonical cell) of line rather than reproducing large sections of the power grid. As such, the canonical cell for the five cases would involve a limited segment of power lines. Because the truncation of the power lines causes RF current leaving the utility pole (forward propagation) to reflect back toward the pole (reverse propagation), minimizing the latter type of current would

reduce the effects of the truncation to better represent the RF current along a long section of the power grid.

A single power line conductor along with its associated RF current is used to illustrate the concept to address the reverse propagating current. Suppose there is an inline source on the power line while the truncation is represented as a simple endpoint as portrayed in Figure 3.7(a), where forward and reverse propagating currents exist. The complex current can be observed at two geometrically distinct locations on the line, noted in the figure as positions 1 and 2. Accordingly, the total current at position 1 or 2 along the line can be expressed as

$$I = I_{\text{fwd}}\, e^{-jk_d d} + I_{\text{rev}}\, e^{+jk_d d}\ , \tag{3.1}$$

with I_{fwd} and I_{rev} being the complex amplitude for the forward and reverse currents at a given position, respectively, k_d is the wavenumber of the current, and d is the line length from the source. Based on Equation (3.1), the forward and reverse amplitudes can be obtained from

$$\begin{bmatrix} I_{\text{fwd}} \\ I_{\text{rev}} \end{bmatrix} = \begin{bmatrix} e^{-jk_d d_1} & e^{+jk_d d_1} \\ e^{-jk_d d_2} & e^{+jk_d d_2} \end{bmatrix}^{-1} \begin{bmatrix} I_1 \\ I_2 \end{bmatrix}, \tag{3.2}$$

where I_1 and I_2 are the observed currents at positions 1 and 2, respectively. Having found the reverse propagating current, a minimization of it can be done by introducing an inline voltage source very close to the endpoint to excite another reverse current though opposite in phase as depicted in Figure 3.7(b). The result from phasing, Figure 3.7(c), would leave a net forward propagating current, Figure 3.7(d), consisting of the forward current due to the source on the utility pole side and a reflected current that originates from the endpoint source.

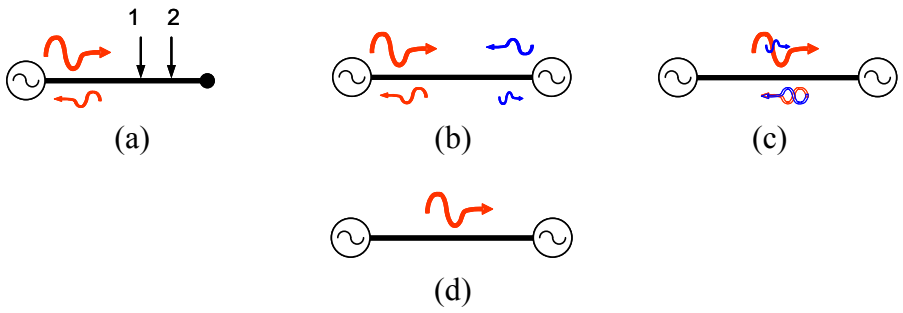

Figure 3.7 (a) Observing the current excited by a source. (b) Another source very close to the truncation endpoint. (c) Cancellation of reverse propagating currents occurs. (d) Only the forward propagating current remains.

The concept for a single line conductor can be extended to address the many truncated conductors that exist on the actual five different feed cases. Figure 3.8(a) shows segments of power lines that extend outward from the utility pole along with their respective forward and reverse propagating RF currents. Because of mutual coupling, an inline source nearby any given endpoint, such as node "a" in Figure 3.8(b), would excite current along the other line segments. Similarly, there will be contributions of such currents from excitation at the other endpoints as illustrated in Figure 3.8(c) that culminate into an overall endpoint excited current on every segment, which minimizes the reverse propagating currents. Like the single line conductor scenario, Figure 3.8(d) shows the outcome as a net forward propagating current.

For the described concept to be effective, it is essential to find the proper excitation at the endpoints that generate the opposite currents. It is convenient to set the excitation type on each line as a voltage source to be consistent with the existing feed cases. As mentioned, the approach is to set the overall endpoint excited currents to have the same magnitude but with a 180^{o} phase difference to minimize the reverse propagating

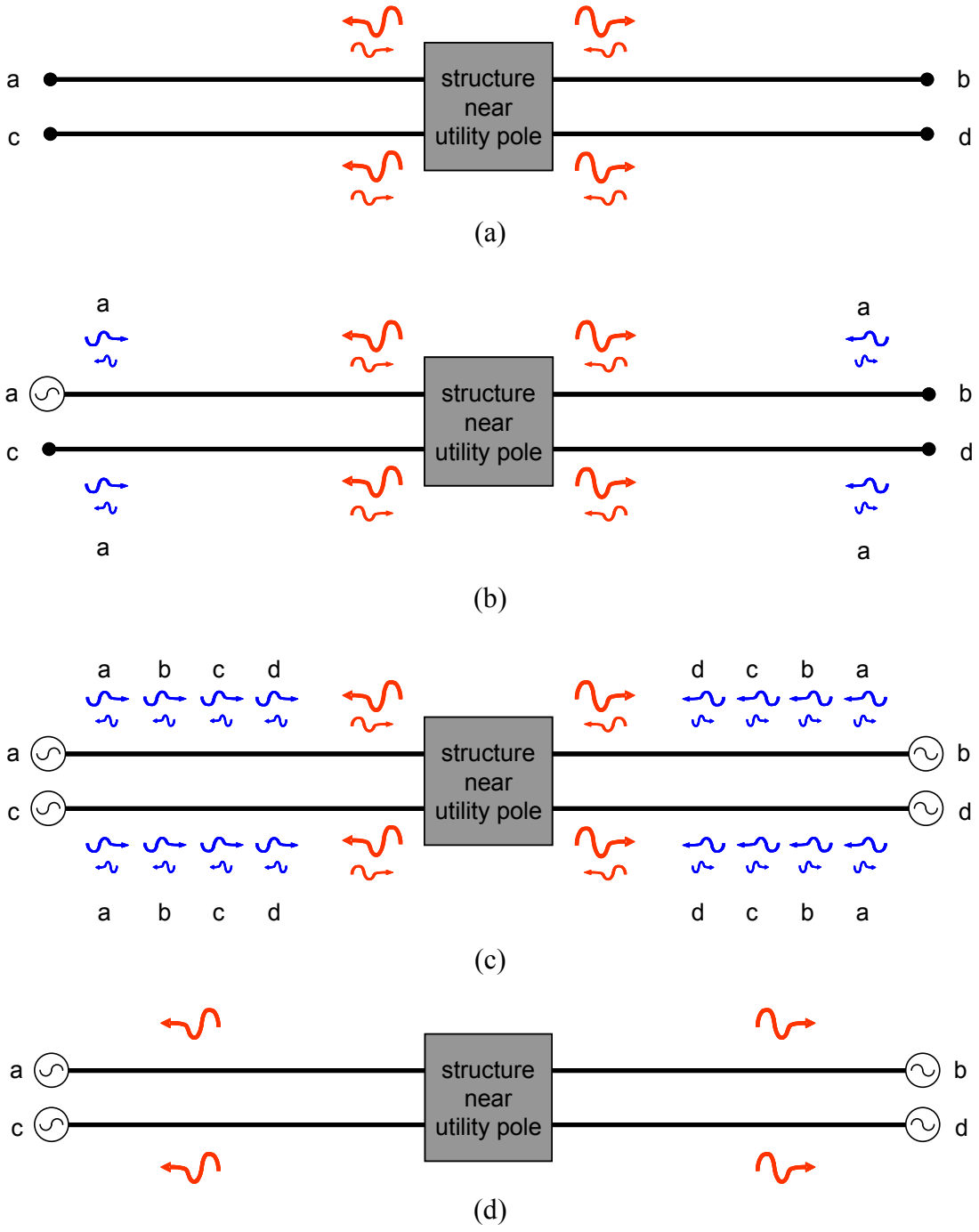

Figure 3.8 Addressing the line truncations of the BPL cell. (a) Original cell. (b) Excitation source at one endpoint. (c) Sources placed at all endpoints. (d) Only the forward propagating currents remain.

currents. This can be described, using notation from Figure 3.8, in form of a matrix equation as

$$-\begin{bmatrix} I_{\text{rev},a,V_s} \\ I_{\text{rev},b,V_s} \\ I_{\text{rev},c,V_s} \\ I_{\text{rev},d,V_s} \end{bmatrix} = \begin{bmatrix} I_{\text{fwd},a,V_a} & I_{\text{fwd},a,V_b} & I_{\text{fwd},a,V_c} & I_{\text{fwd},a,V_d} \\ I_{\text{fwd},b,V_a} & I_{\text{fwd},b,V_b} & I_{\text{fwd},b,V_c} & I_{\text{fwd},b,V_d} \\ I_{\text{fwd},c,V_a} & I_{\text{fwd},c,V_b} & I_{\text{fwd},c,V_c} & I_{\text{fwd},c,V_d} \\ I_{\text{fwd},d,V_a} & I_{\text{fwd},d,V_b} & I_{\text{fwd},d,V_c} & I_{\text{fwd},d,V_d} \end{bmatrix} \begin{bmatrix} V_a \\ V_b \\ V_c \\ V_d \end{bmatrix} \frac{1}{V_S}, \tag{3.3}$$

where $I_{\text{rev},a\to d,V_s}$ is the reverse propagating current due to a device terminal voltage V_S and $I_{\text{fwd},a\to d,V_{a\to d}}$ is the reverse propagating current (forward propagating with respect to the endpoint) due to $V_{a\to d}$, this being the inline voltage at the endpoint on wires "a" through "d". The currents $I_{\text{rev},a\to d,V_s}$ are found by energizing V_S while leaving $V_{a\to d}$ to be zero before applying Equation (3.2) on each segment. Meanwhile, $I_{\text{fwd},a\to d,V_{a\to d}}$ are found by leaving V_S to be zero while energizing each endpoint source one at a time, along with applying Equation (3.2) on each wire for every energizing source. Hence, the endpoint voltages that would provide the minimization of the reverse currents are obtained from

$$\begin{bmatrix} V_a \\ V_b \\ V_c \\ V_d \end{bmatrix} = \left(-V_S\right) \begin{bmatrix} I_{\text{fwd},a,V_a} & I_{\text{fwd},a,V_b} & I_{\text{fwd},a,V_c} & I_{\text{fwd},a,V_d} \\ I_{\text{fwd},b,V_a} & I_{\text{fwd},b,V_b} & I_{\text{fwd},b,V_c} & I_{\text{fwd},b,V_d} \\ I_{\text{fwd},c,V_a} & I_{\text{fwd},c,V_b} & I_{\text{fwd},c,V_c} & I_{\text{fwd},c,V_d} \\ I_{\text{fwd},d,V_a} & I_{\text{fwd},d,V_b} & I_{\text{fwd},d,V_c} & I_{\text{fwd},d,V_d} \end{bmatrix}^{-1} \begin{bmatrix} I_{\text{rev},a,V_s} \\ I_{\text{rev},b,V_s} \\ I_{\text{rev},c,V_s} \\ I_{\text{rev},d,V_s} \end{bmatrix}. \tag{3.4}$$

Note that the technique is applicable to an arbitrary number of wires and truncation sources, even though the discussion only involves four here.

Although the line truncation effects have largely been addressed now, the use of inline voltage sources at the endpoints poses another issue, since such discontinuities

radiate. However, the impact of the produced field on observations can be greatly reduced by having the endpoints sufficiently distant from the observed locations. Additionally, the technique tends to have better performance with longer segments of power lines.

3.3 Calculation of Currents

As mentioned, the fields are obtained through the currents and so the calculation of the currents is presented in this section. The currents are calculated through the use of two different implementation of EFIE MoM, each corresponding to a distinct software package. Figure 3.9 illustrates the difference in approaches between the two packages.

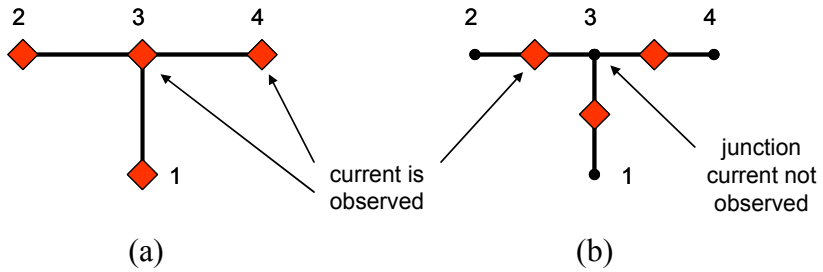

Figure 3.9 Comparison of locations where current is calculated (observed) for a wire junction using (a) moment method 1 and (b) moment method 2.

The first moment method is based on the application of triangular basis functions detailed in [25]. The corresponding software package, EMPACK 2000, is a program for academic purposes that compute currents on a structure in the frequency domain. With the use of triangular basis functions, it can represent any distribution of current as a collection of piecewise-linear functions. This aspect makes it more accommodating to distributions that have discontinuous derivatives, which could occur at bend and junctions. Since observations take place at the end node of each MoM element, currents at wire

junctions are directly found, making the enforcement of Kirchhoff's current law (KCL) quite explicit. Though the software does not presently have a field calculator, this is addressed by the methods noted previously on Chapter 2. In this environment, the endpoint sources to minimize the truncation effects are placed on the second to the last (outermost) end nodes near the ends of the power lines.

The second moment method is based on the application of sinusoidal basis functions detailed in [26]. The corresponding software package, 4nec2, is a program powered by the second version of the Numerical Electromagnetics Code (NEC-2) engine. NEC-2 performs a frequency domain EFIE MoM with the distribution of current being represented by a collection of piecewise-sinusoidal functions with observations taken at the center of each MoM element. With the currents at the ends of each MoM element being an extrapolated value, currents at wire junctions are indirect and so enforcement of the KCL is no longer explicit. The advantage, though, is the built-in field calculator for observing near- and far-fields over a PEC or finite-conductive earth. With excitations also located at the center of MoM elements, the endpoint sources are placed on the outermost MoM element (going towards the endpoints) along the power lines.

3.4 Results and Observations

In this section, the following assumptions have been made so that quantitative values can be obtained to demonstrate the concepts discussed throughout the chapter:

- The device terminal is impressed with a 1V excitation
- The earth is modeled as a PEC
- The fields are calculated within 100 meters from the utility pole

- The power line endpoints are $20\lambda_0$ at 30 MHz ($\approx$ 200 meters) away (along the longitudinal direction x) from the utility pole.

Unless there are indications to the contrary, these assumptions are expected to provide sufficiently general conditions from which observations can be made as well as identification of a particular case for a further more involved analysis. To facilitate the comparison among the various results, the vertical scaling is made to be consistent between all currents and field intensity plots, respectively.

Figures 3.10 through 3.12 compare the currents for case 1 based on the system model shown in Figure 3.2, where only wire C would exist. Figure 3.10 illustrates the frequency effect on the distribution of current from moment method 1. An apparent difference in distribution exists within 50 meters (along the longitudinal direction x) of the utility pole, where the inductive coupler is located. Note the relatively monotonic distributions along the 50 to 150 meter section of the line, which indicate a low standing wave ratio (SWR) and means that the forward propagating currents are predominant. Applying Equation (3.2), the reverse propagating currents are approximately zero at 3 MHz while being less than 0.2% of their respective forward current at 30 MHz. Figures 3.11 and 3.12 compare the currents obtained via the two moment methods at 3 and 30 MHz, respectively. As can be seen, there is good agreement between both moment methods at the two frequencies though each moment method uses different basis functions and implementation schemes.

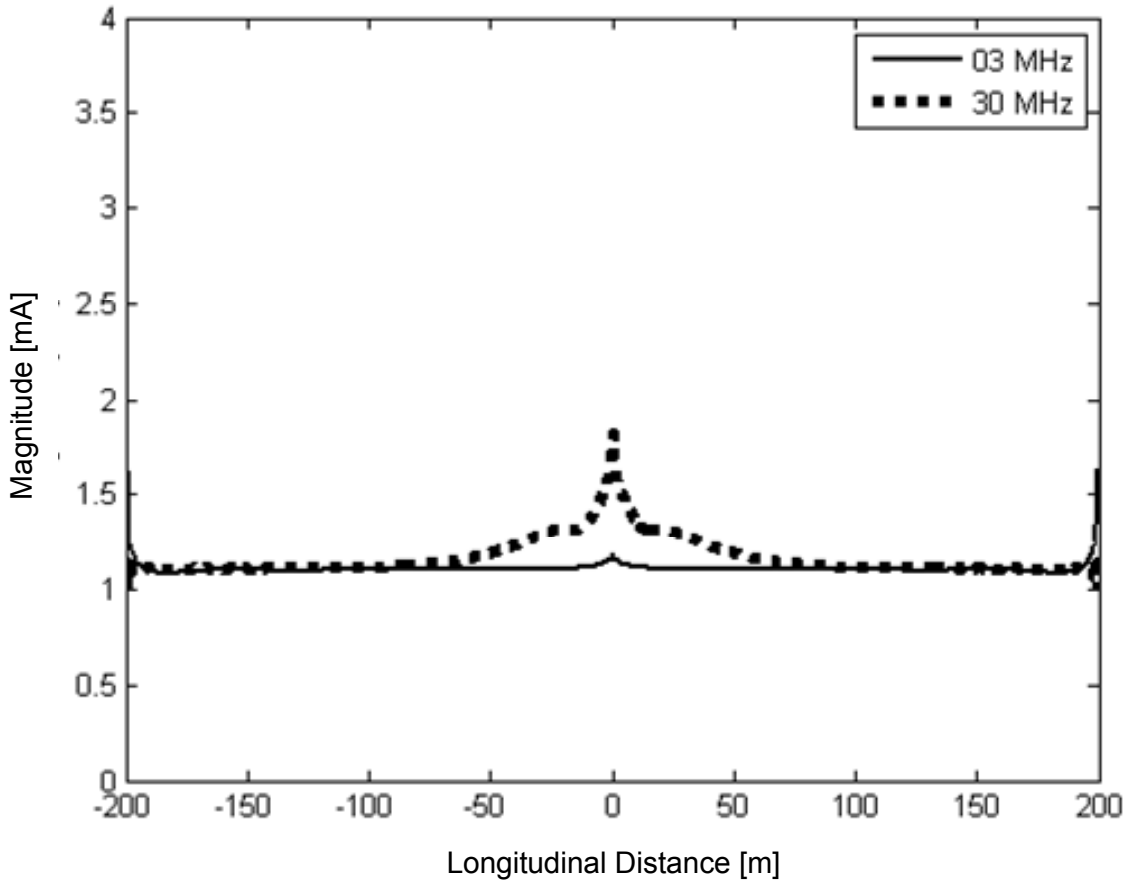

Figure 3.10 Currents for case 1 along power line from moment method 1 at 3 and 30 MHz.

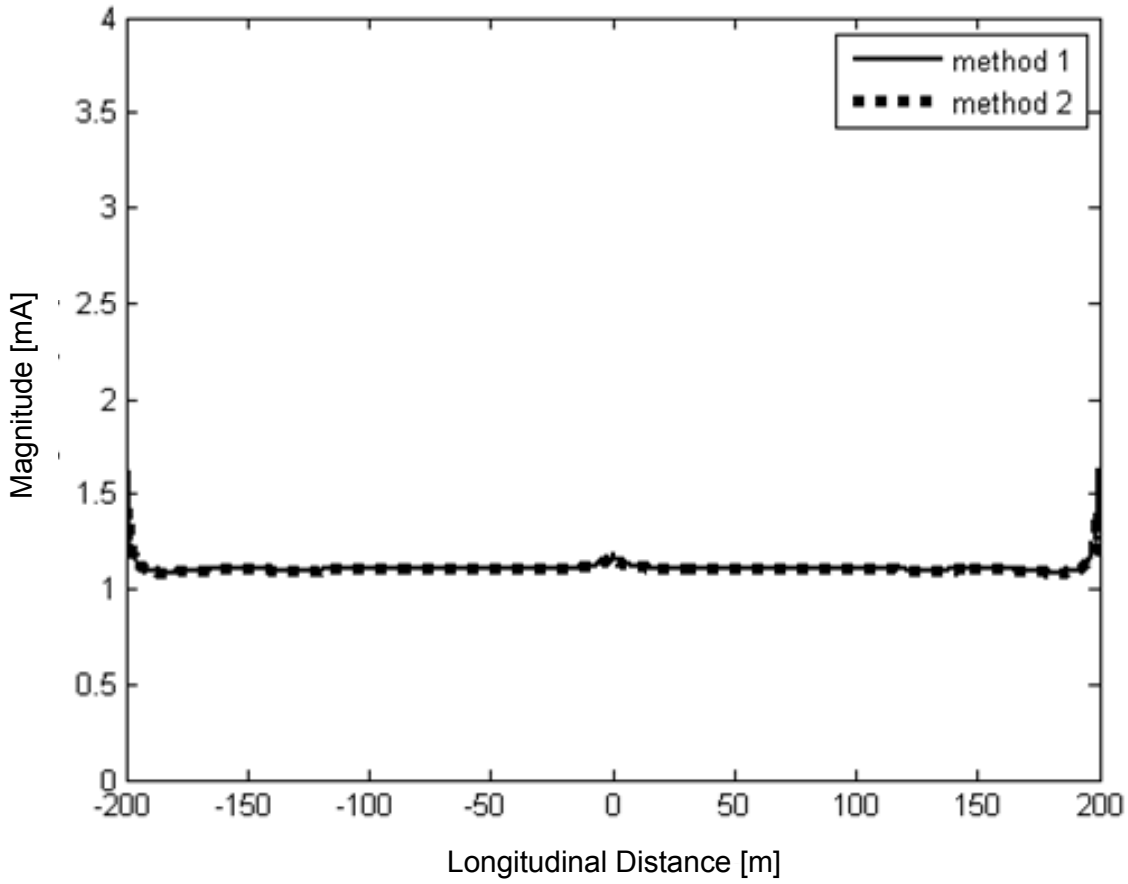

Figure 3.11 Currents for case 1 along power line from both moment methods at 3 MHz.

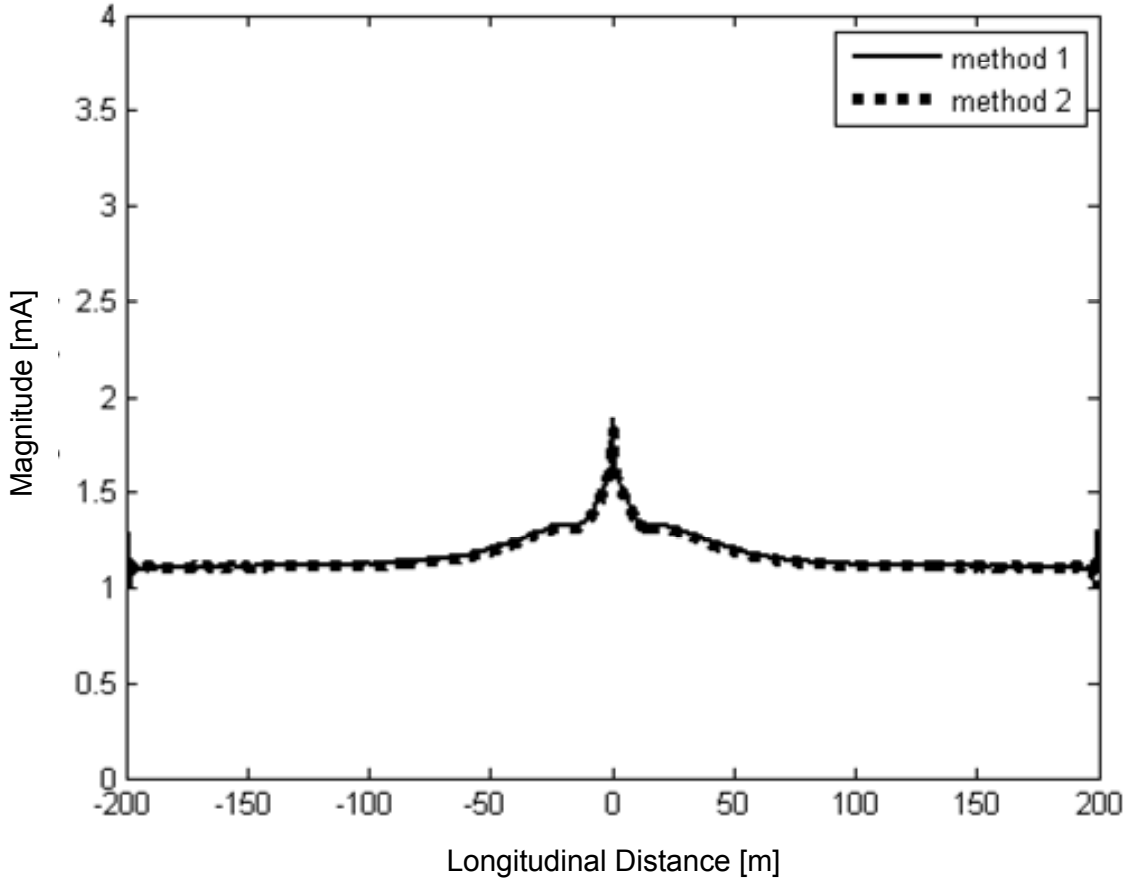

Figure 3.12 Currents for case 1 along power line from both moment methods at 30 MHz.

Figures 3.13 through 3.17 compare the currents for case 2 based on the system model shown in Figure 3.3, which involves feed and power line wires. Figure 3.13 illustrates the frequency effect on the distribution of current from moment method 1 along the vertical signal feed line while Figure 3.14 pertains to the power lines. Figures 3.15 and 3.16 compare the currents obtained via the two moment methods at 3 MHz for wires B and C, respectively, while Figure 3.17 would be for both power line wires at 30 MHz. Like before, there is good agreement between the two moment methods at both frequencies. Similar to case 1, the distribution of current along the 50 to 150 meter

section of power is relatively monotonic and indicative of predominantly forward propagating currents. The reverse propagating currents are found, by means of Equation (3.2), to be approximately zero at 3 MHz and less than 0.2% of their respective forward current at 30 MHz. From Figure 3.14, it is apparent at 30 MHz that there is an imbalance of current between power lines and a less pronounced difference in distribution comparing to case 1 within 50 meters (along the longitudinal direction *x*) of the utility pole. Note that the increasing 30 MHz feed line currents in Figure 3.13 are akin to a loaded end-fed dipole antenna.

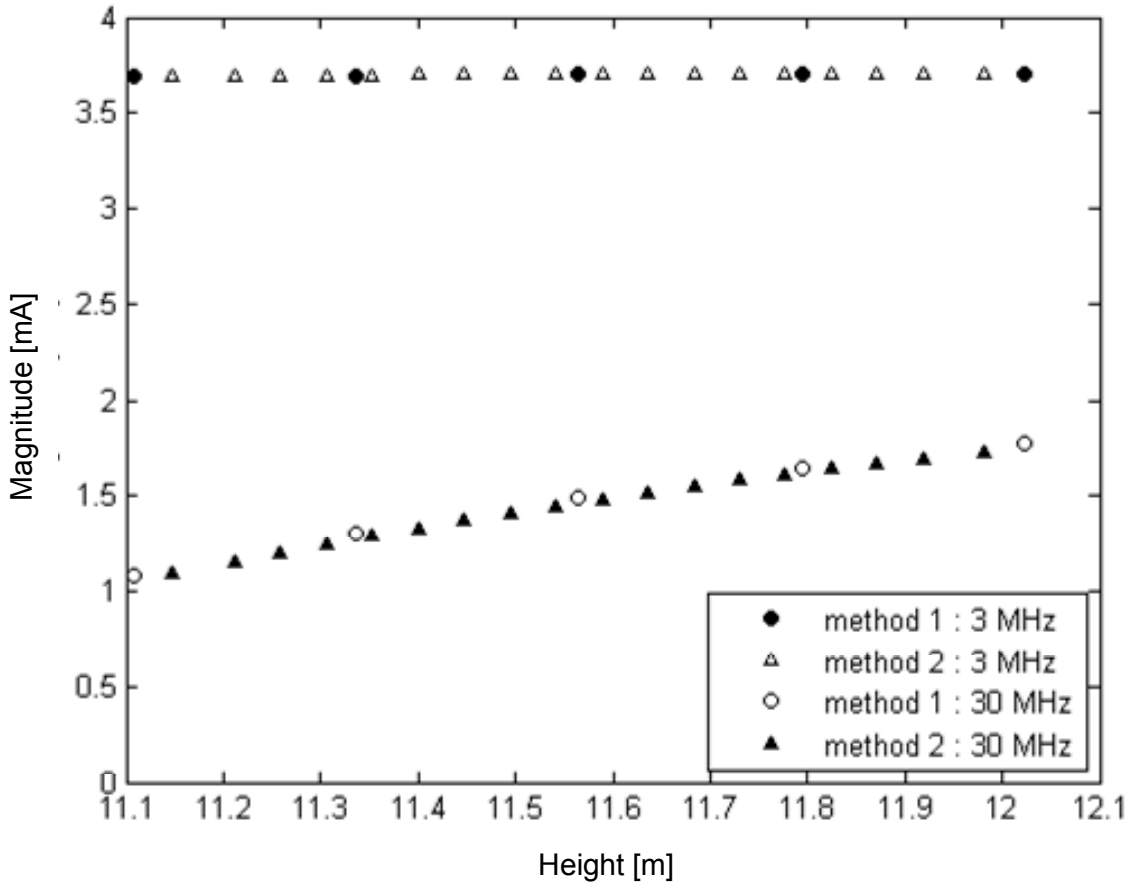

Figure 3.13 Currents for case 2 along vertical signal feed line from both moment methods at 3 and 30 MHz.

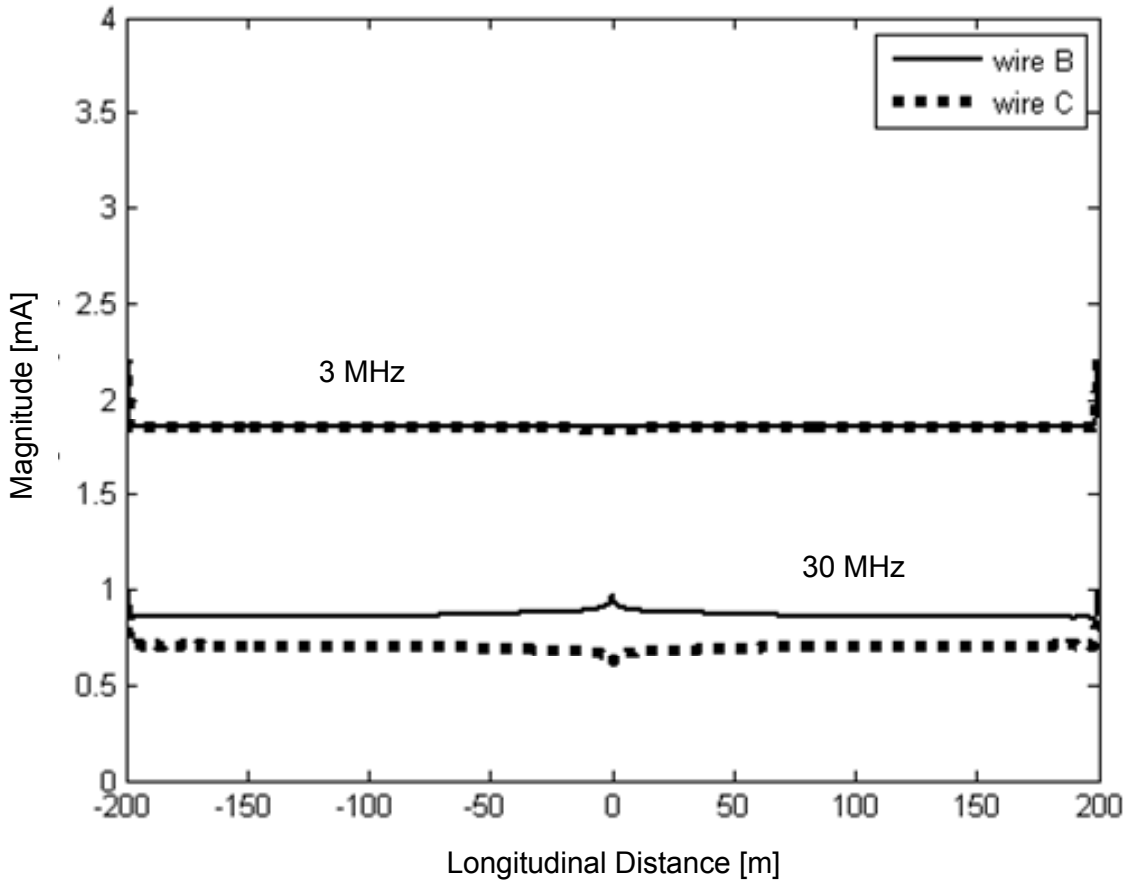

Figure 3.14 Currents for case 2 along power lines from moment method 1 at 3 and 30 MHz.

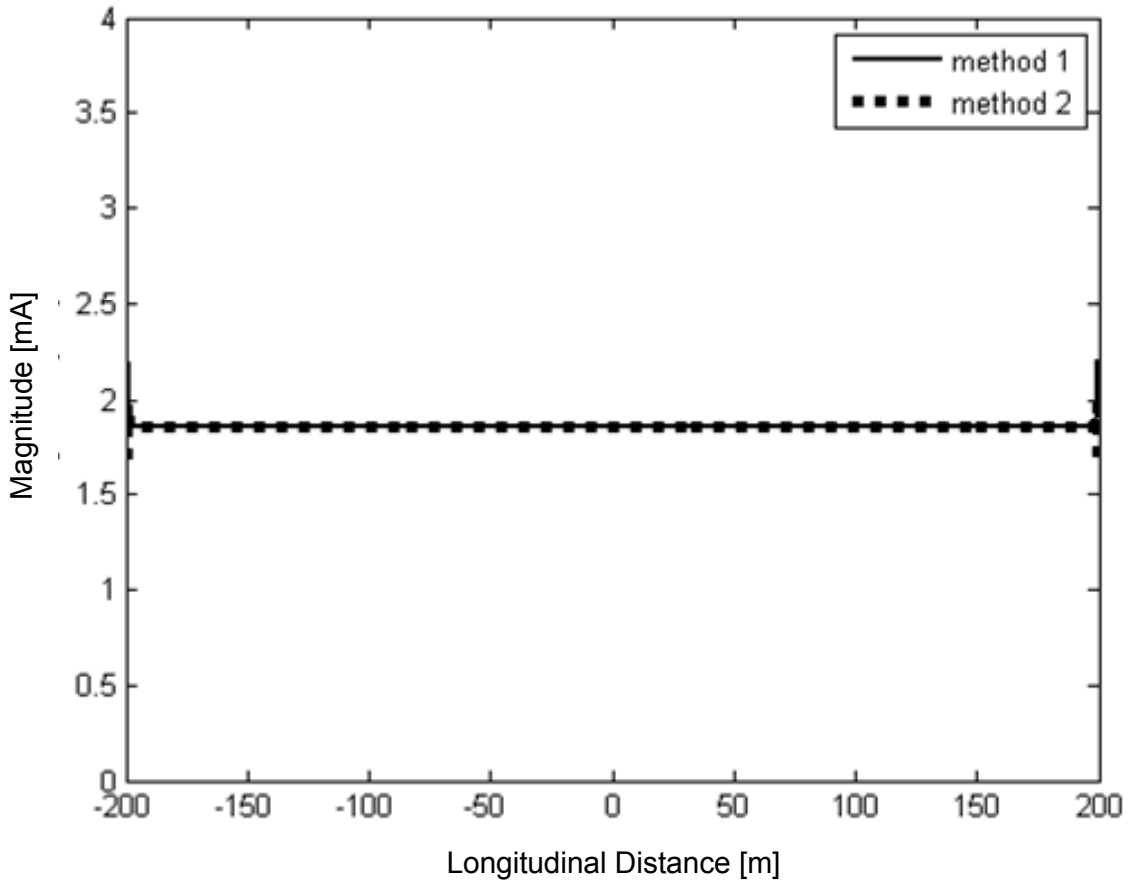

Figure 3.15 Currents for case 2 along power line wire B from both moment methods at 3 MHz.

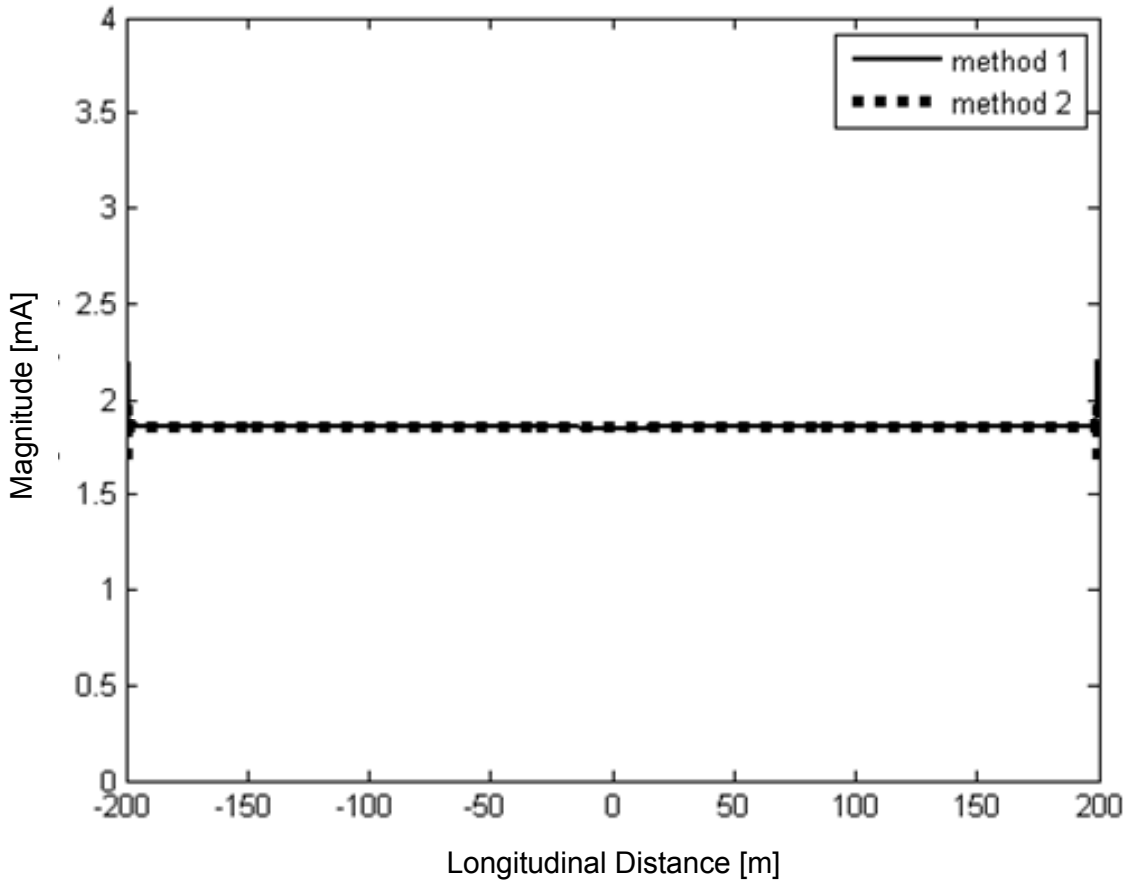

Figure 3.16 Same as Figure 3.15, except being along power line wire C.

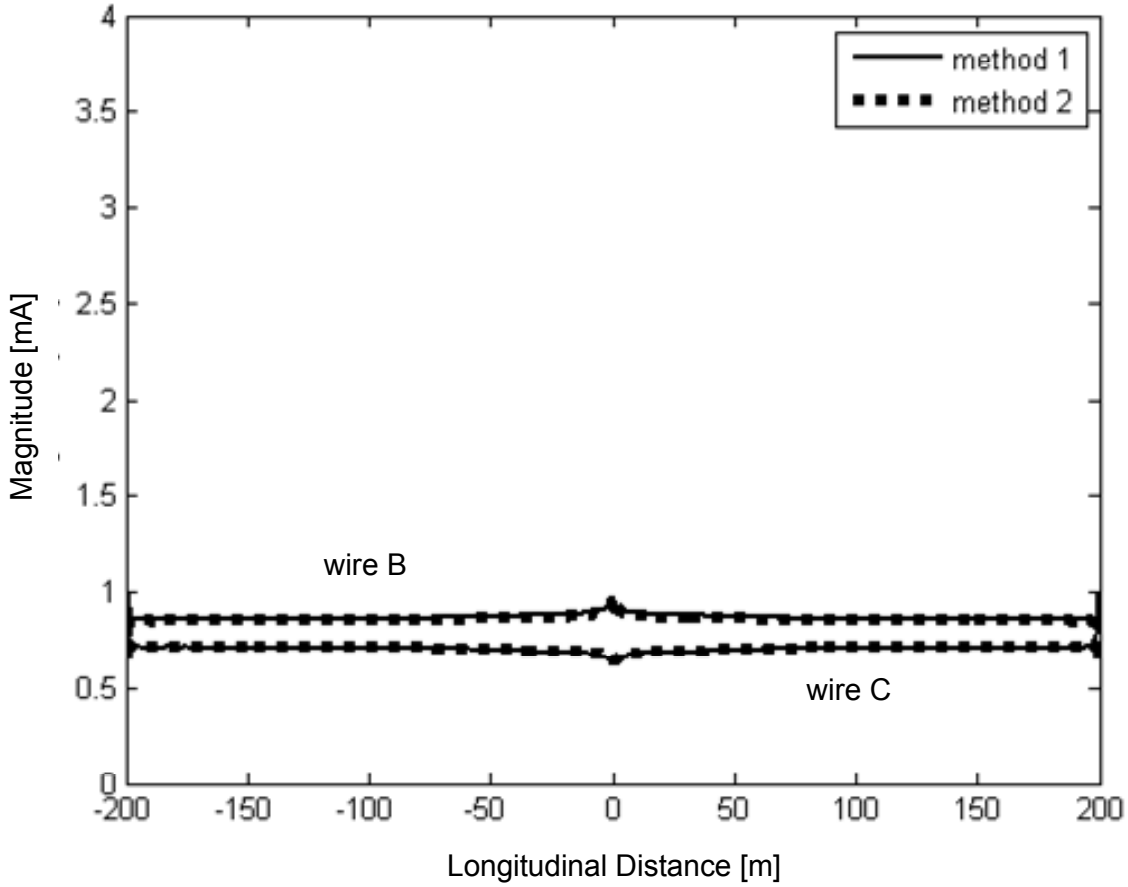

Figure 3.17 Currents for case 2 along power lines from both moment methods at 30 MHz.

Figures 3.18 through 3.21 compare the currents for case 3 based on the system model shown in Figure 3.4, which have feed lines that are horizontal (as are the power line wires). Figure 3.18 illustrates the frequency effect on the distribution of current from moment method 1 along the signal feed line while Figure 3.19 pertains to the power lines. Figure 3.20 compare the currents obtained via the two moment methods for wire A, while Figure 3.21 would be for wire B at 3 and 30 MHz, respectively. Again, there is good agreement between the two moment methods at both frequencies. As can be seen in

Figure 3.19, the distribution of current along the power lines is remarkably flat and balanced, with the reverse currents being approximately zero at both frequencies. Note that the 30 MHz horizontal feed line currents in Figure 3.18 resemble that of a loaded center-fed dipole antenna.

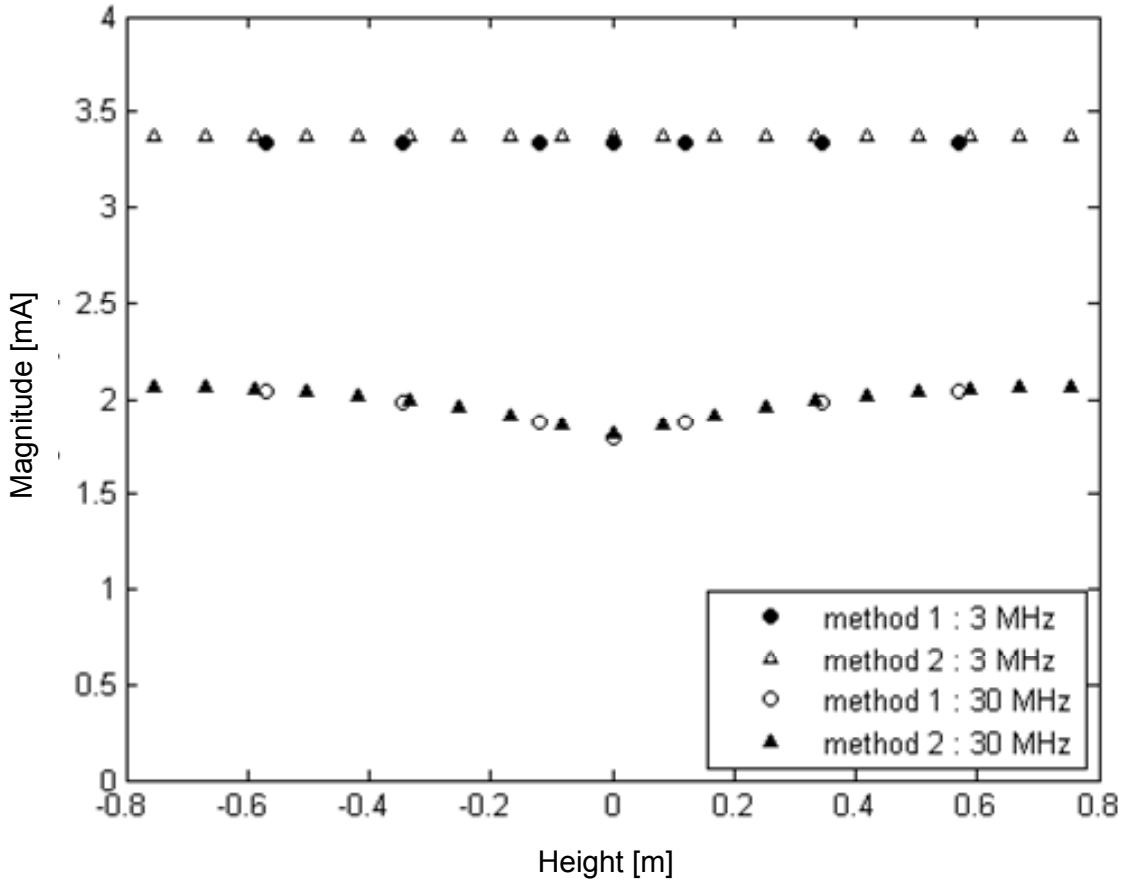

Figure 3.18 Currents for case 3 along signal feed line from both moment methods at 3 and 30 MHz.

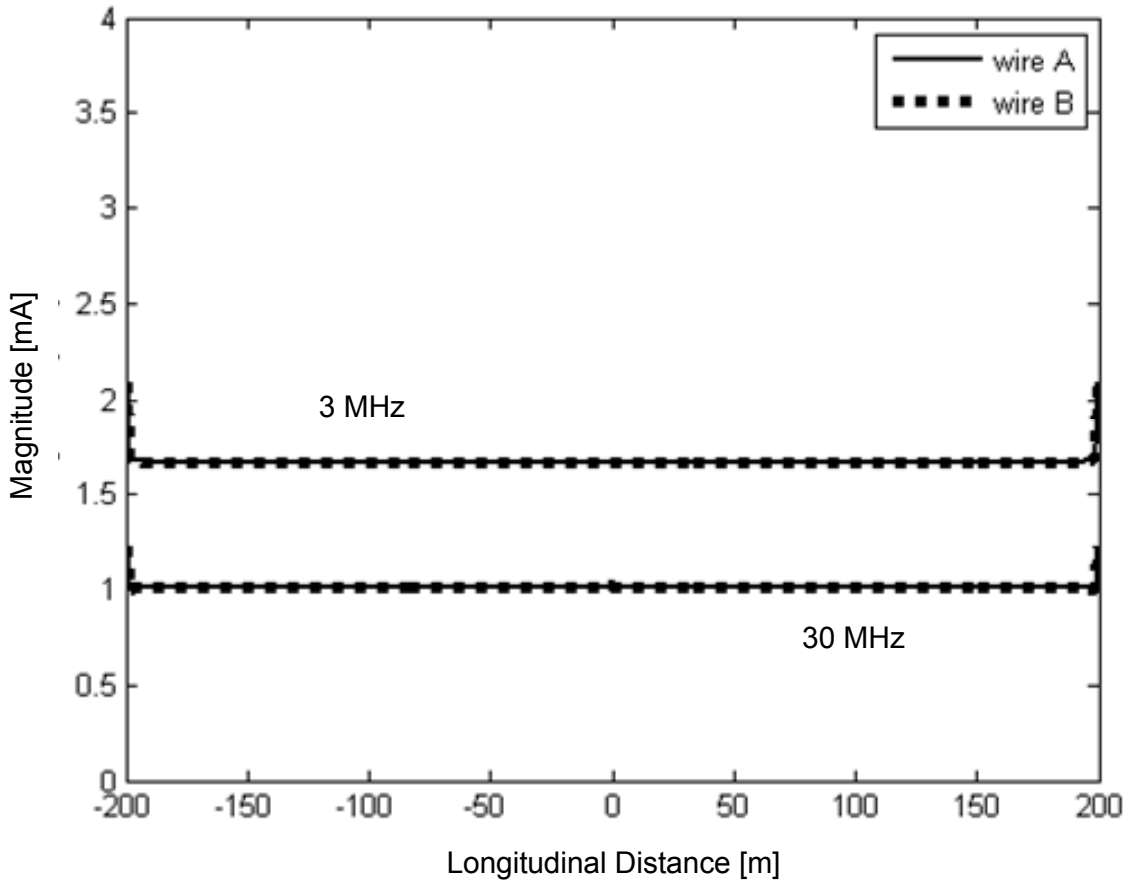

Figure 3.19 Currents for case 3 along power lines from moment method 1 at 3 and 30 MHz.

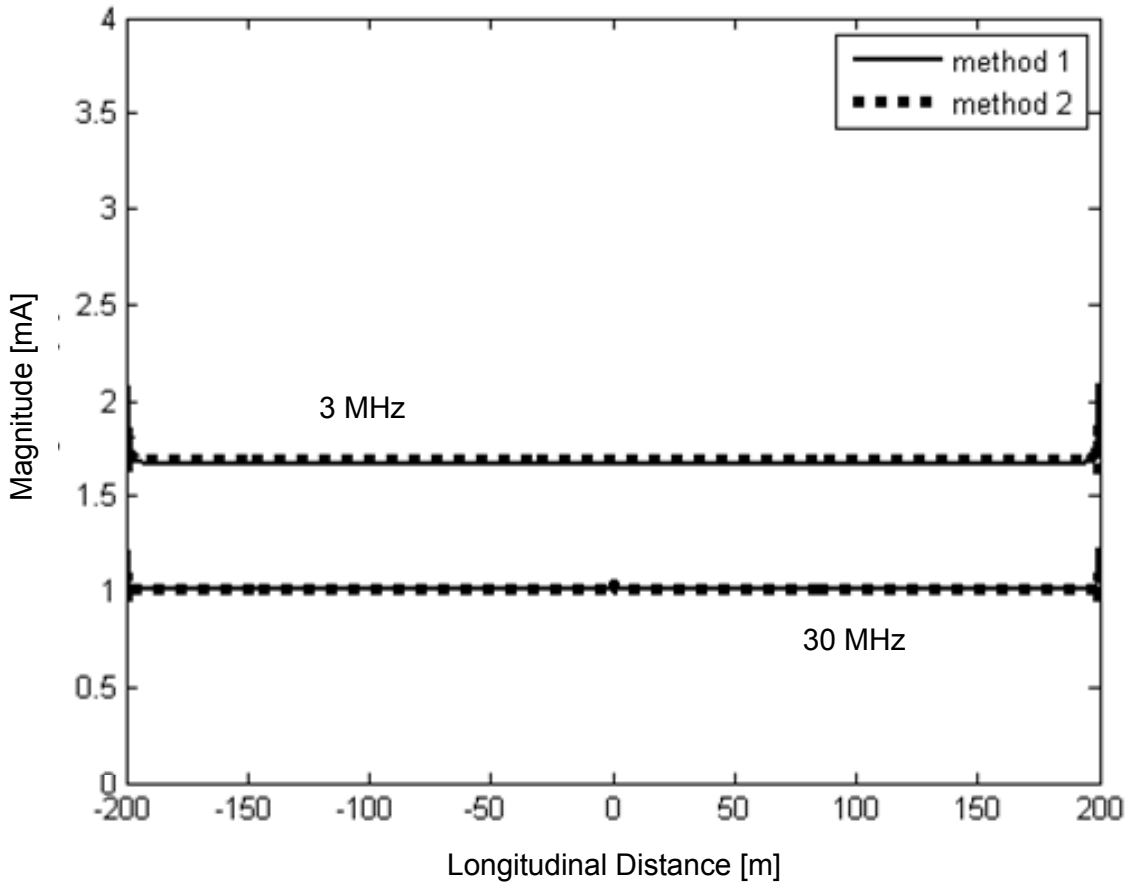

Figure 3.20 Currents for case 3 along power line wire A from both moment methods.

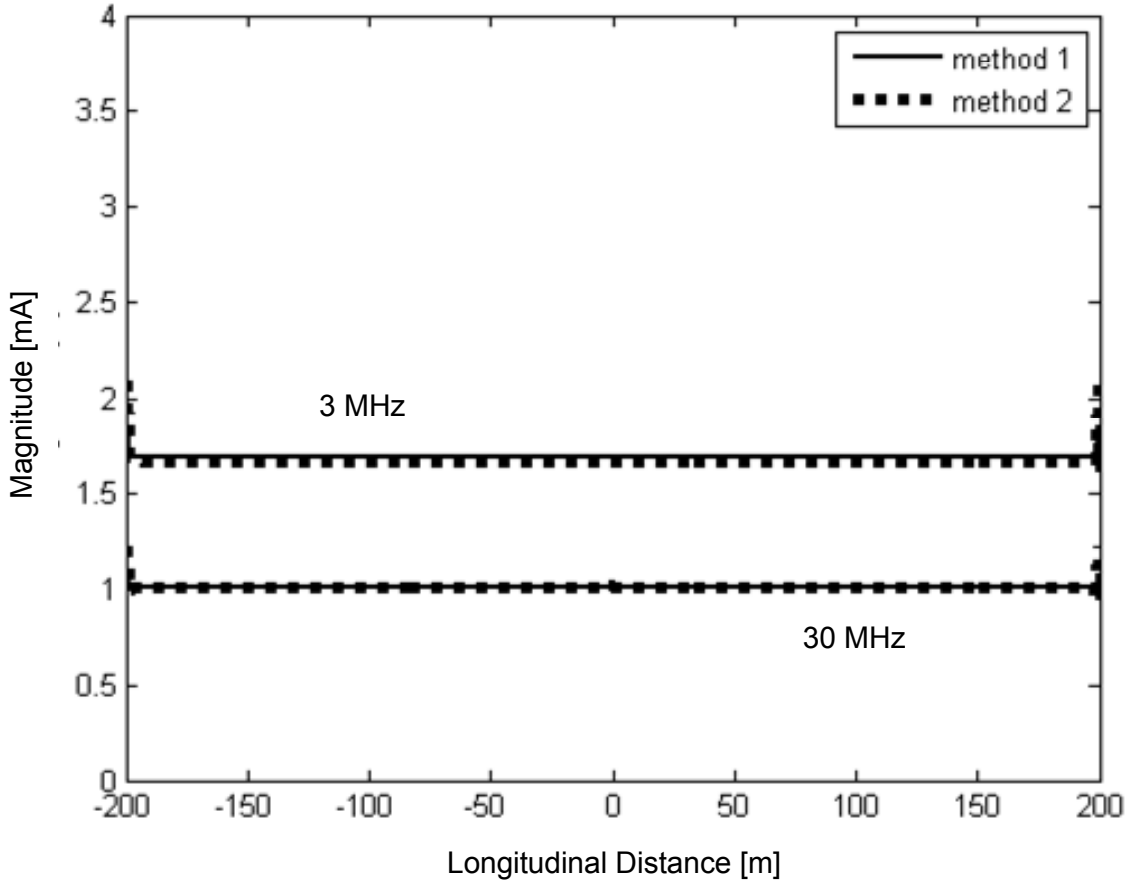

Figure 3.21 Same as Figure 3.20, except that the results are for power line wire B.

Figures 3.22 through 3.25 compare the currents for case 4 based on the system model shown in Figure 3.5, which is analogous to case 2 in regards to the signal feed and power line wires. Figure 3.22 illustrates the frequency effect on the distribution of current from moment method 1 along the vertical signal feed line and grounding wire, while Figure 3.23 pertains to the power lines. However, the neutral wire N is connected to a pole grounding wire and so Figure 3.22 includes the vertical grounding line current. Figures 3.24 and 3.25 compare the currents obtained via the two moment methods for both power line wires at 3 and 30 MHz, respectively. The distribution of current along

the 50 to 150 meter section of power lines is relatively monotonic with the reverse currents being approximately zero at 3 MHz and less than 0.2% of the forward current at 30 MHz. The agreement between the two moment methods at both frequencies is good, though better at 30 MHz than at 3 MHz. As can be seen in Figure 3.23, the unbalance of current between wires C and N is greater at 3 MHz than at 30 MHz. Note from Figure 3.22 that the profile at 30 MHz of the grounding line current is comparable to a $\frac{3}{2}\lambda$

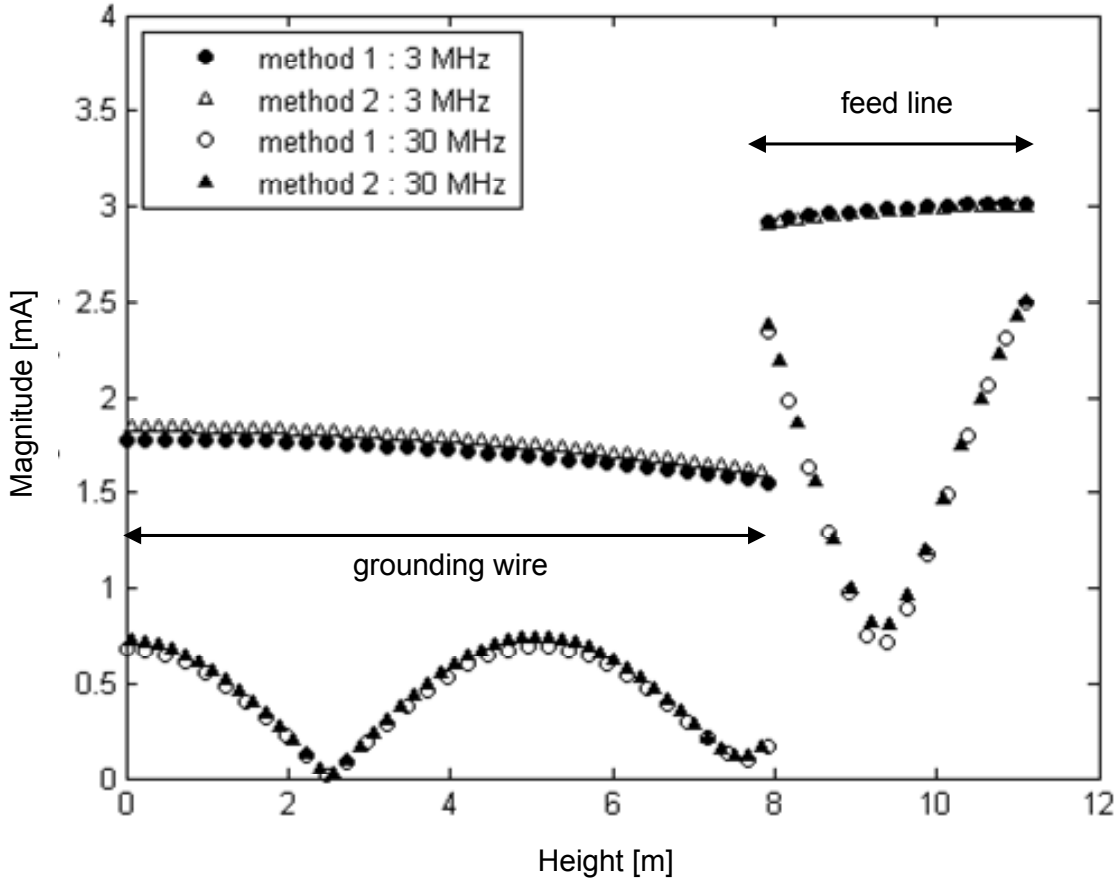

Figure 3.22 Currents for case 4 along vertical signal feed line and grounding wire from both moment methods at 3 and 30 MHz.

dipole antenna, while the signal feed line current resembles that of a loaded center-fed dipole antenna. Unseen in the previous cases, the signal feed and grounding line currents at 3 MHz also exhibit profiles of a small loaded dipole antenna.

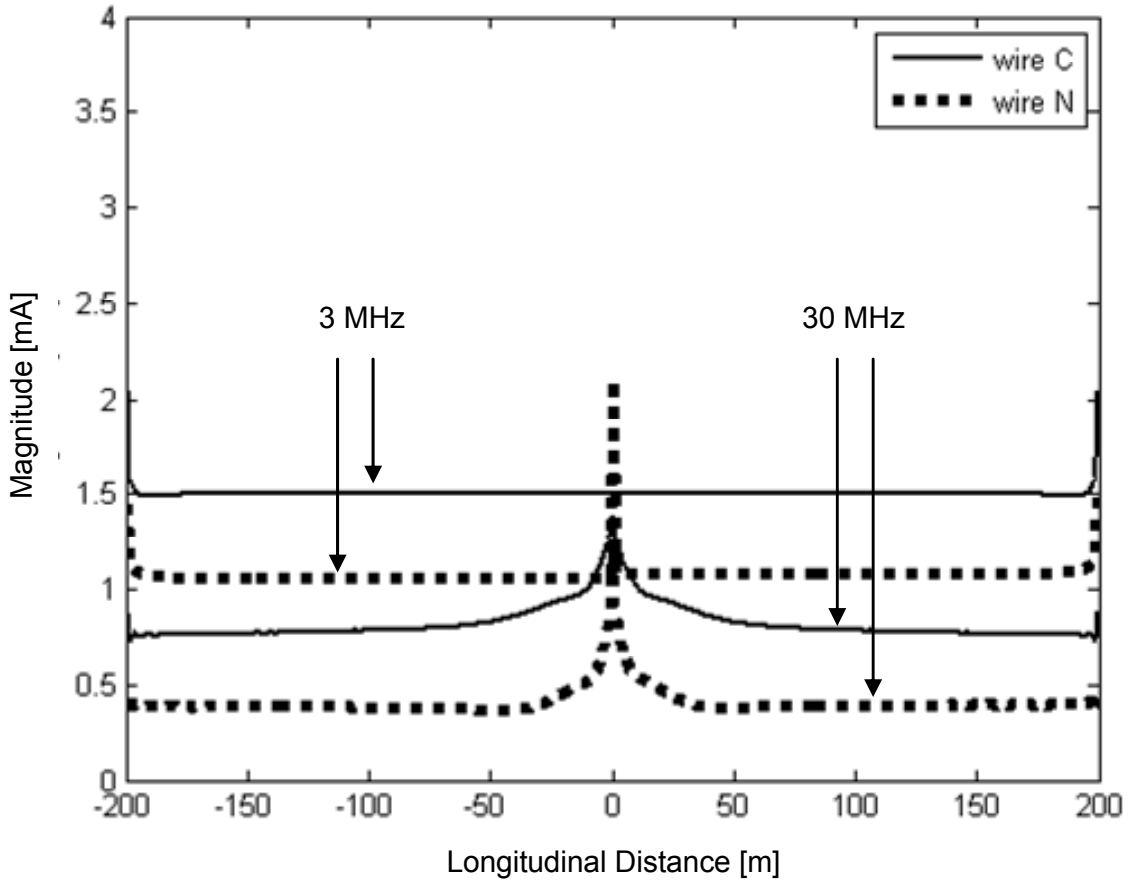

Figure 3.23 Currents for case 4 along power lines from moment method 1 at 3 and 30 MHz.

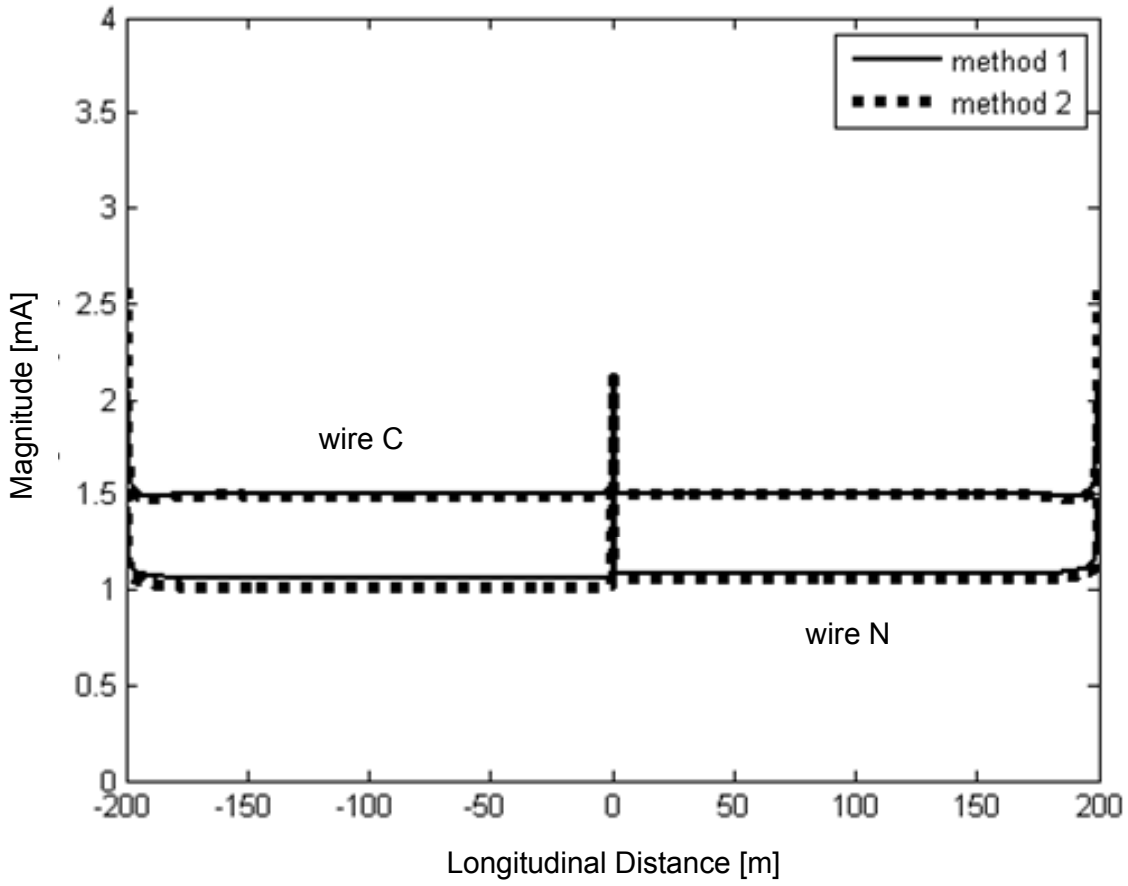

Figure 3.24 Currents for case 4 along power lines from both moment methods at 3 MHz.

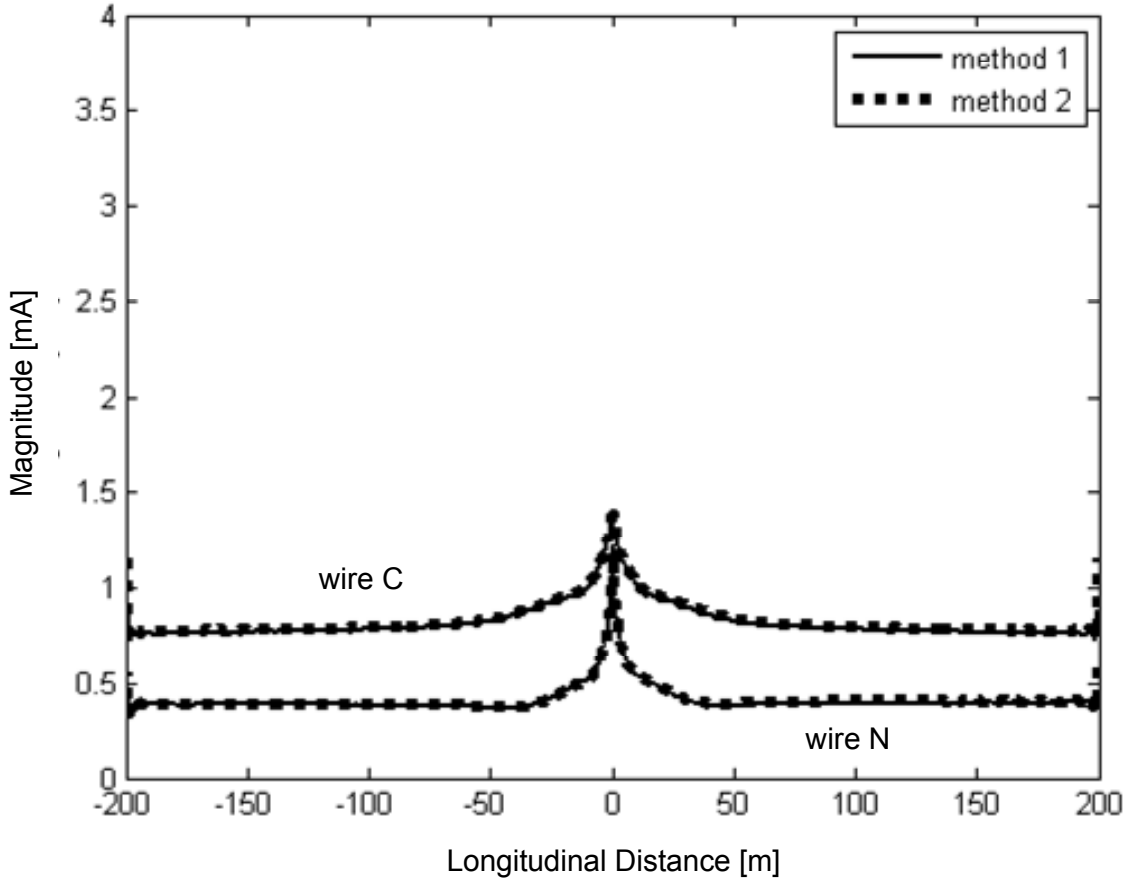

Figure 3.25 Same as Figure 3.24, except at 30 MHz.

Figures 3.26 through 3.31 compare the currents for case 5 based on the system model shown in Figure 3.6, which is like case 4 in regards to the signal feed, grounding, and power line wires. The main difference is that the signal feed line current exists from the earth to the height of wire C. Figure 3.26 illustrates the frequency effect on the distribution of current from moment method 1 along the vertical signal feed line and grounding wire, while Figure 3.29 pertains to the power lines. Figures 3.27 and 3.28 compare the currents obtained via the two moment methods for the vertical feed line and grounding wires at 3 and 30 MHz, respectively, while Figures 3.30 and 3.31 are for both

power line wires in a similar manner. As before, the distributions of current along the 50 to 150 meter section of power lines is relatively monotonic with the reverse currents being approximately zero at 3 MHz and less than 0.4% of the forward current at 30 MHz. Similarly, there is good agreement between the two moment methods at both frequencies, more so at 30 MHz. The currents along the signal feed and grounding lines have resemblance to loaded off-center-fed dipole antennas.

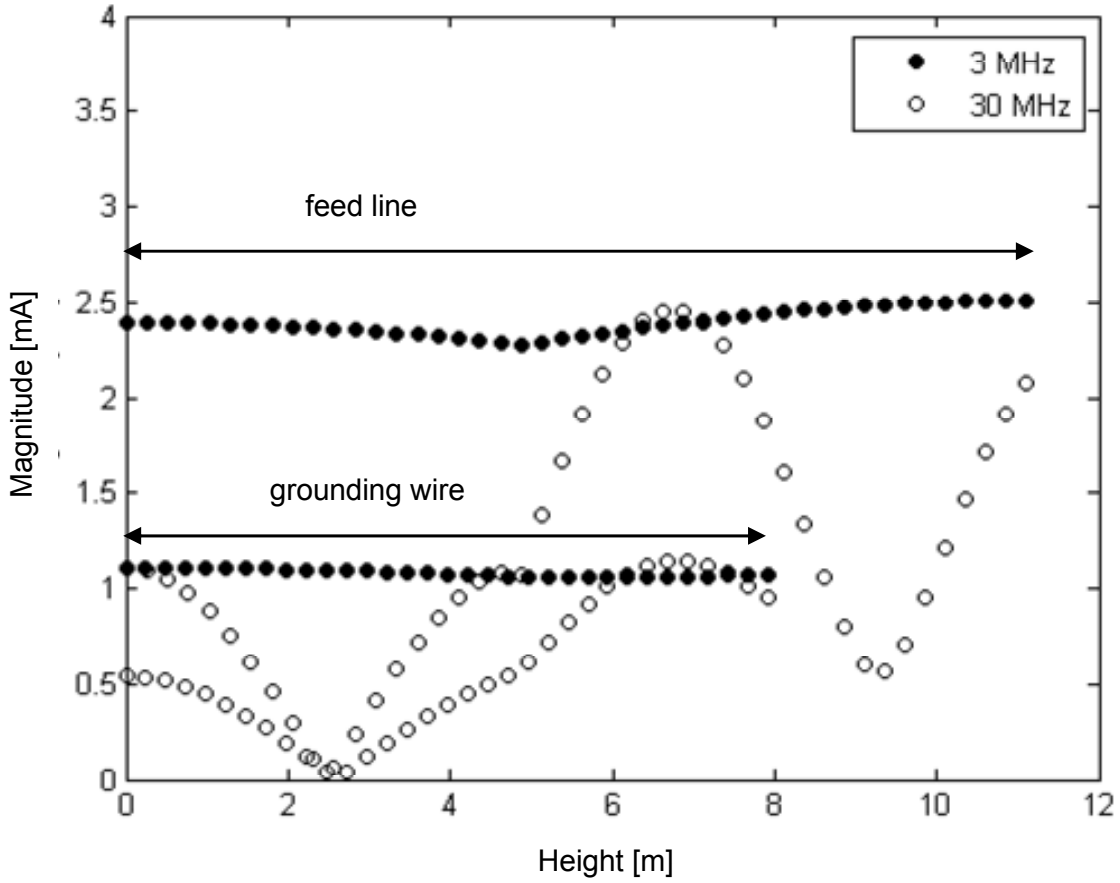

Figure 3.26 Currents for case 5 along vertical signal feed line and grounding wire from moment method 1 at 3 and 30 MHz.

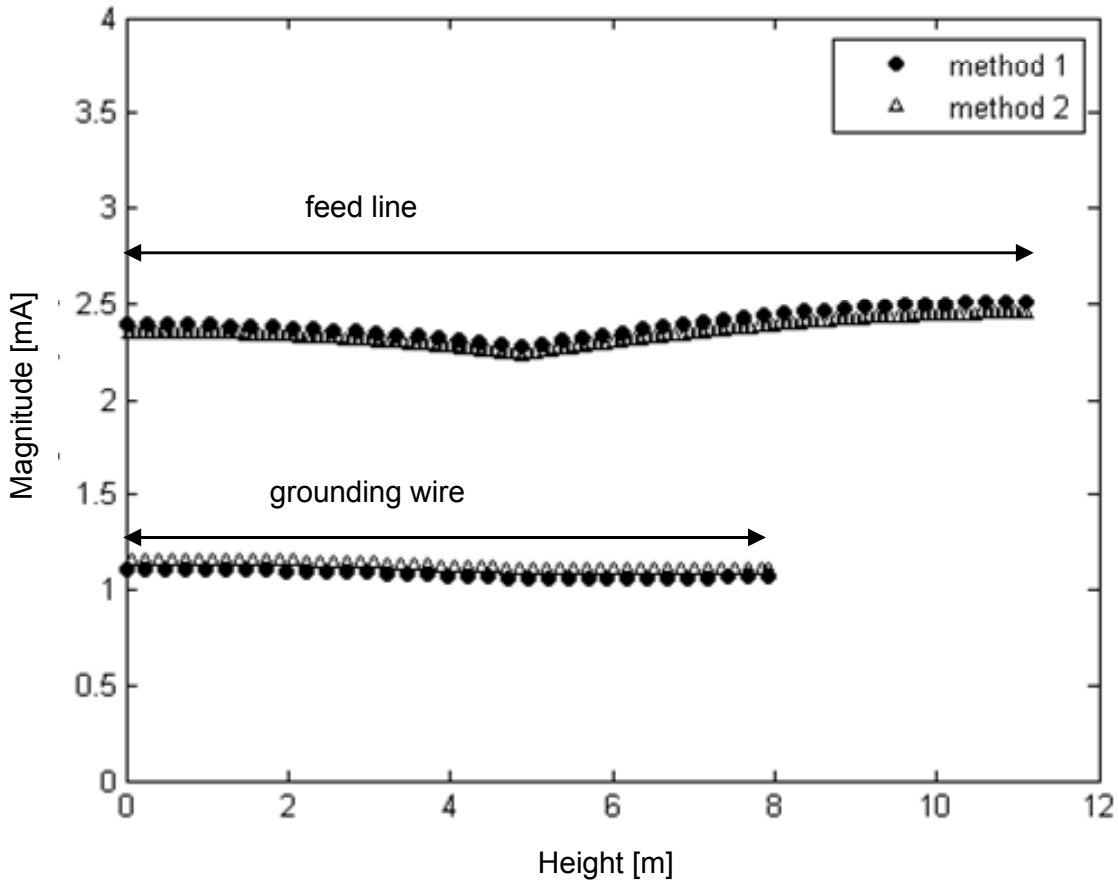

Figure 3.27 Currents for case 5 along vertical signal feed line and grounding wire from both moment methods at 3 MHz.

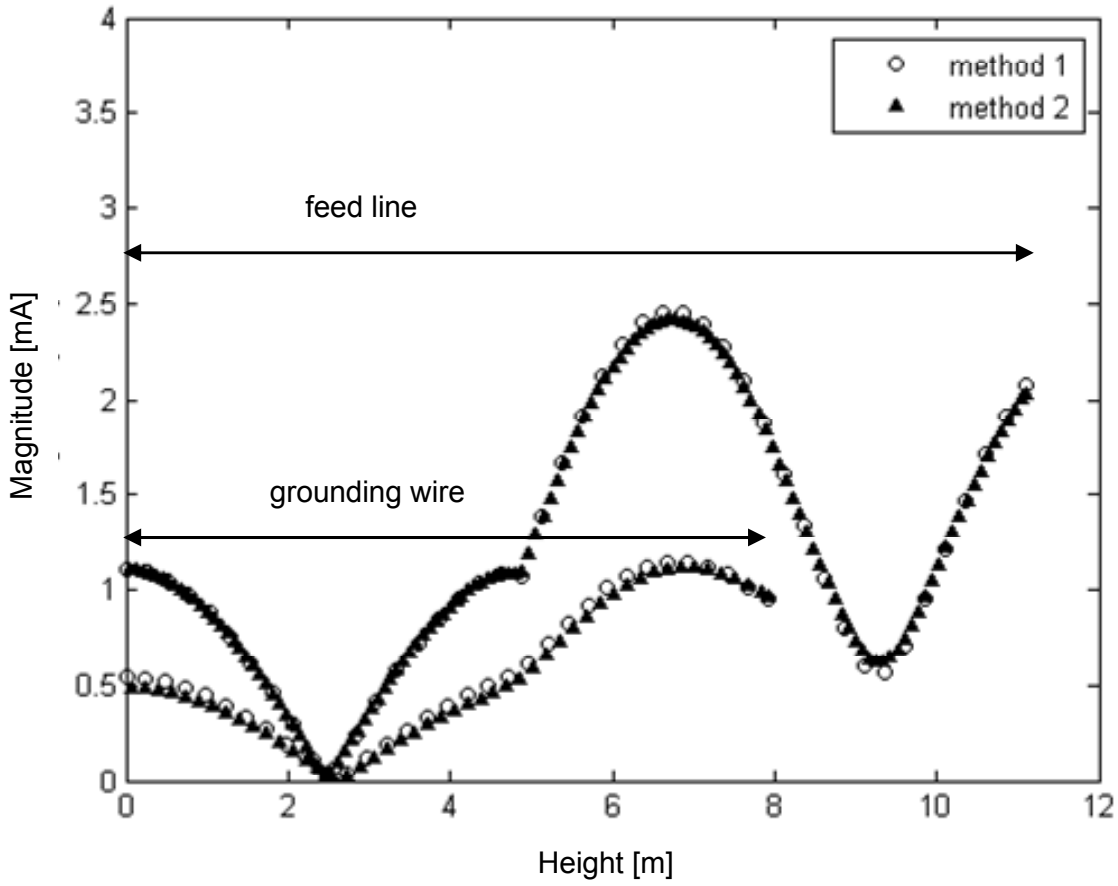

Figure 3.28 Same as Figure 3.27, except at 30 MHz.

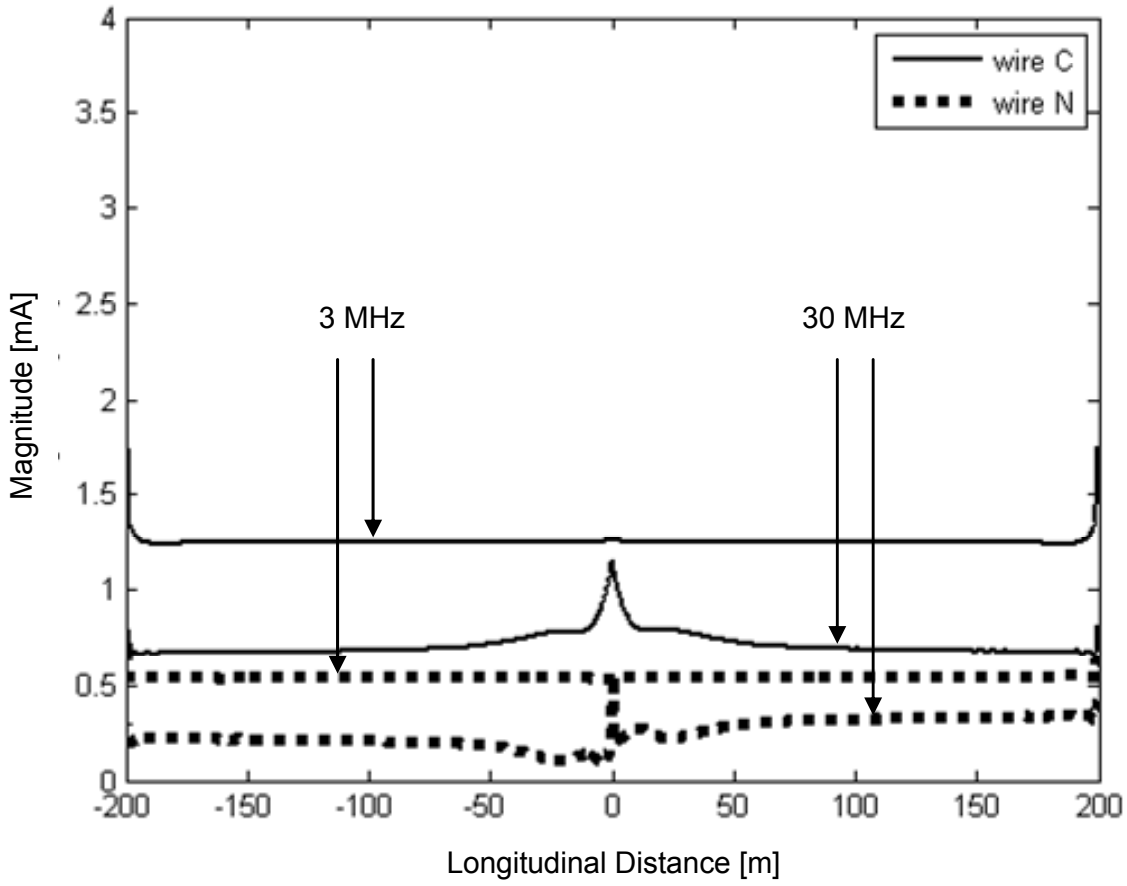

Figure 3.29 Currents for case 5 along power lines from moment method 1 at 3 and 30 MHz.

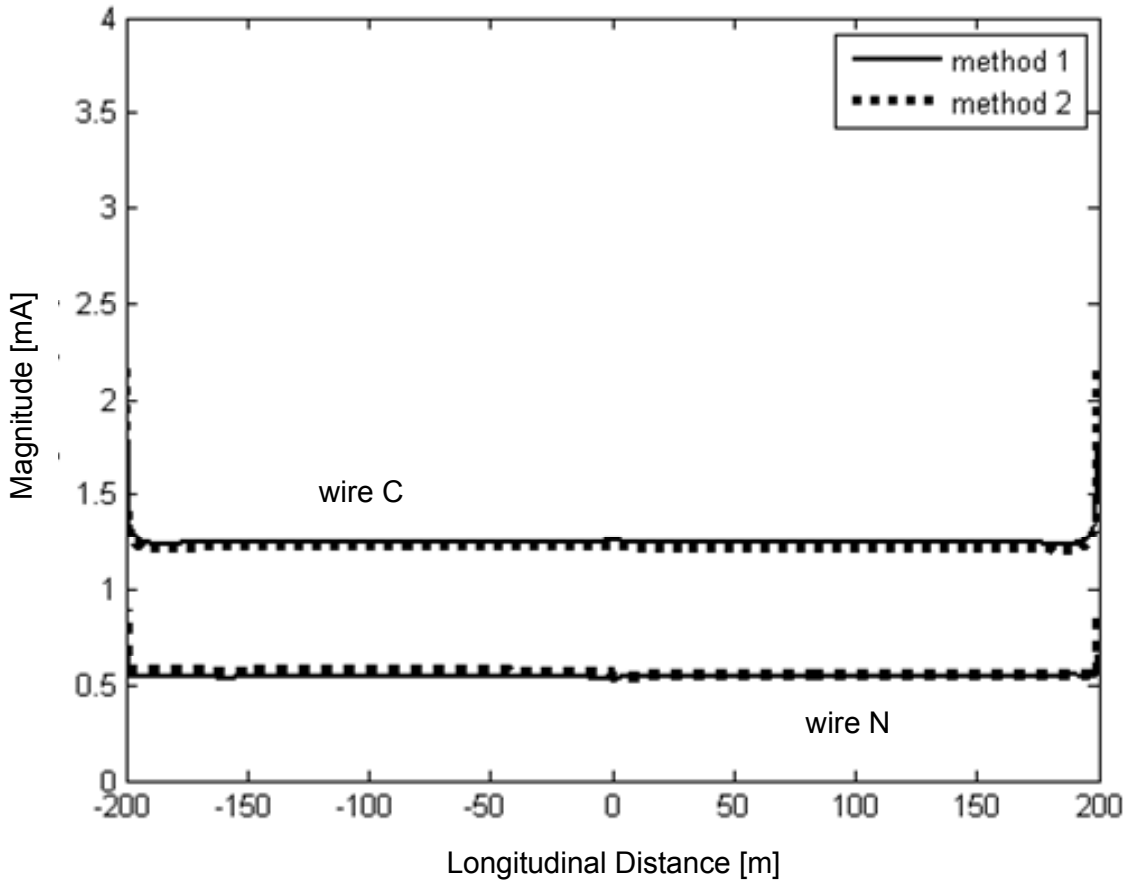

Figure 3.30 Currents for case 5 along power lines from both moment methods at 3 MHz.

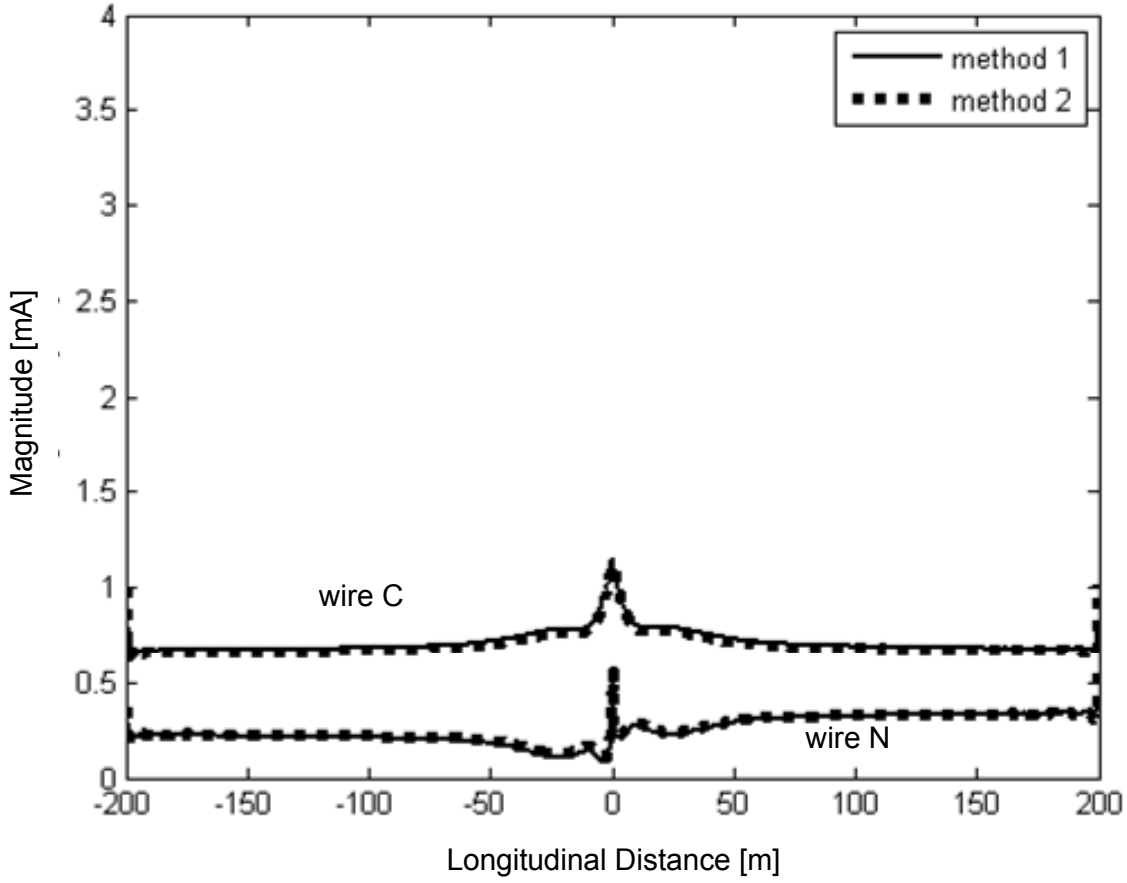

Figure 3.31 Same as Figure 3.30, except at 30 MHz.

Table 3.1 notes the input currents at the device terminal for the five cases, from the two moment methods at 3 and 30 MHz. It further illustrates the agreement at both frequencies between moment methods 1 and 2. The table exemplifies the types of load a BPL device may encounter. It also provides a reference in which input power scaling can be performed to meet FCC regulations.

Table 3.1 Device input current [mA] at 3 and 30 MHz for the five cases, from moment methods 1 and 2.

	3 MHz		30 MHz	
case	mtd 1	mtd 2	mtd 1	mtd 2
1	1.16 + j 0.238	1.16 + j 0.215	1.78 + j 0.648	1.77 + j 0.420
2	3.61 – j 0.774	3.58 – j 0.892	0.687 – j 0.830	0.617 – j 0.907
3	3.31 – j 0.416	3.34 – j0.425	1.26 – j 1.28	1.26 – j 1.32
4	2.54 – j 1.45	2.58 – j 1.34	1.31 + j 1.95	1.49 + j 1.85
5	1.44 – j 1.76	1.51 – j 1.64	0.753 – j 0.758	0.813 – j 0.729

Figures 3.32 through 3.35 depict the electric field intensities along the earth for the five cases at 3 and 30 MHz, respectively, to identify the scenario most likely to be in conflict with FCC regulations. Based on moment method 2 currents, the surface plot is at $z = 0$ with color codes that indicate the field intensity. Since the currents between moment methods 1 and 2 for the five cases are shown from Figures 3.11 through 3.31 to be generally the same, their fields are anticipated to match correspondingly. Note that the most intense fields in all cases shown in Figures 3.32 and 3.33 are either directly underneath the power lines or near the utility pole, where the signal feed and grounding lines are located. To determine the case that is most likely to be of interest regarding the FCC regulations, the field values in the region between the FCC lines have been omitted in Figures 3.34 and 3.35, with the scale adjusted to provide greater detail near the FCC lines. As can be seen, the field level of cases 4 and 5 further away from the power line is in some instances more intense than the fields near the FCC lines of the other cases. The distinctly different colors near the FCC lines after the omission in cases 4 and 5 of both figures make them of particular interest.

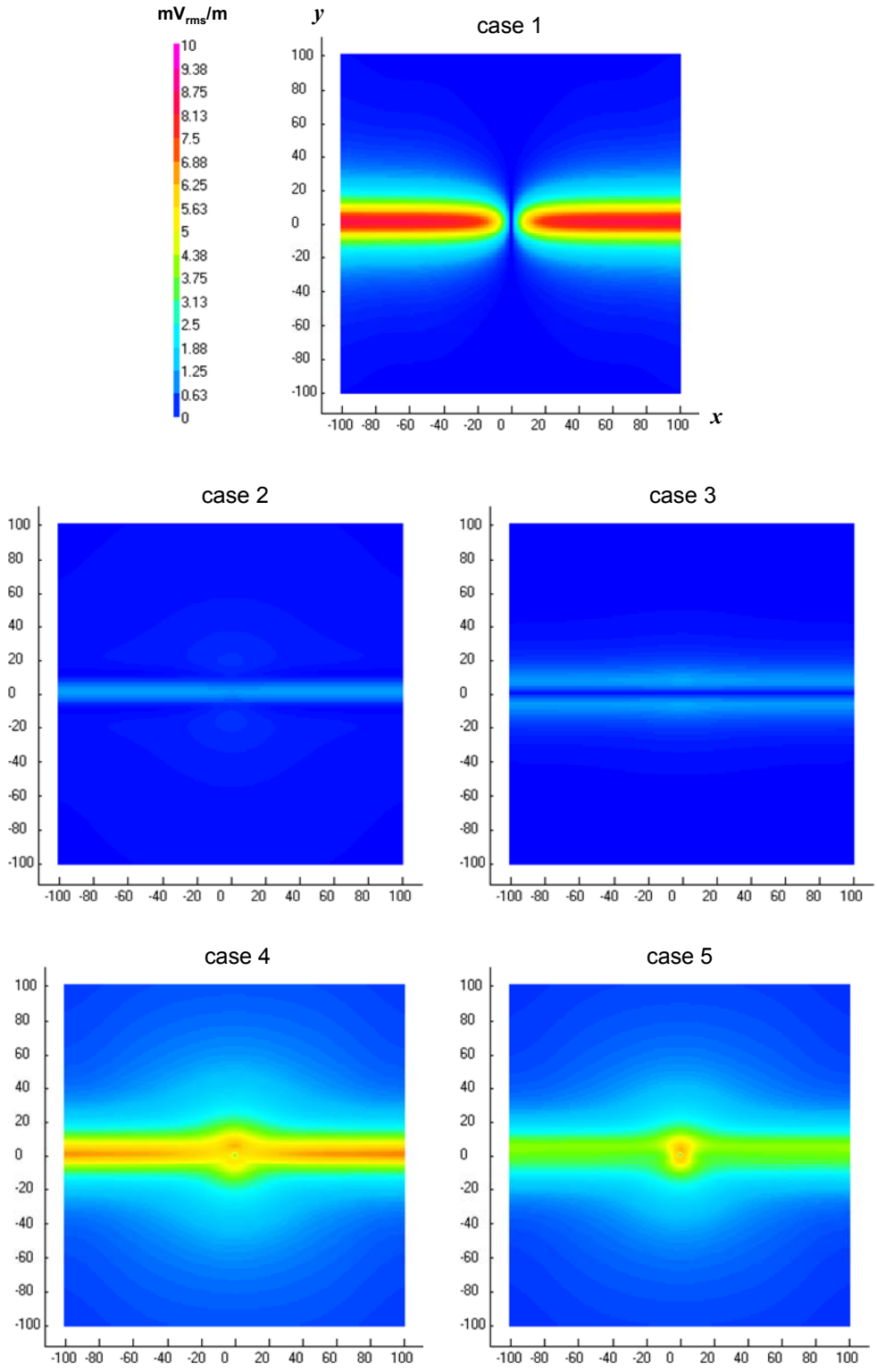

Figure 3.32 Surface plots comparing at 3 MHz E-field along earth (z = 0) between the five cases from moment method 2.

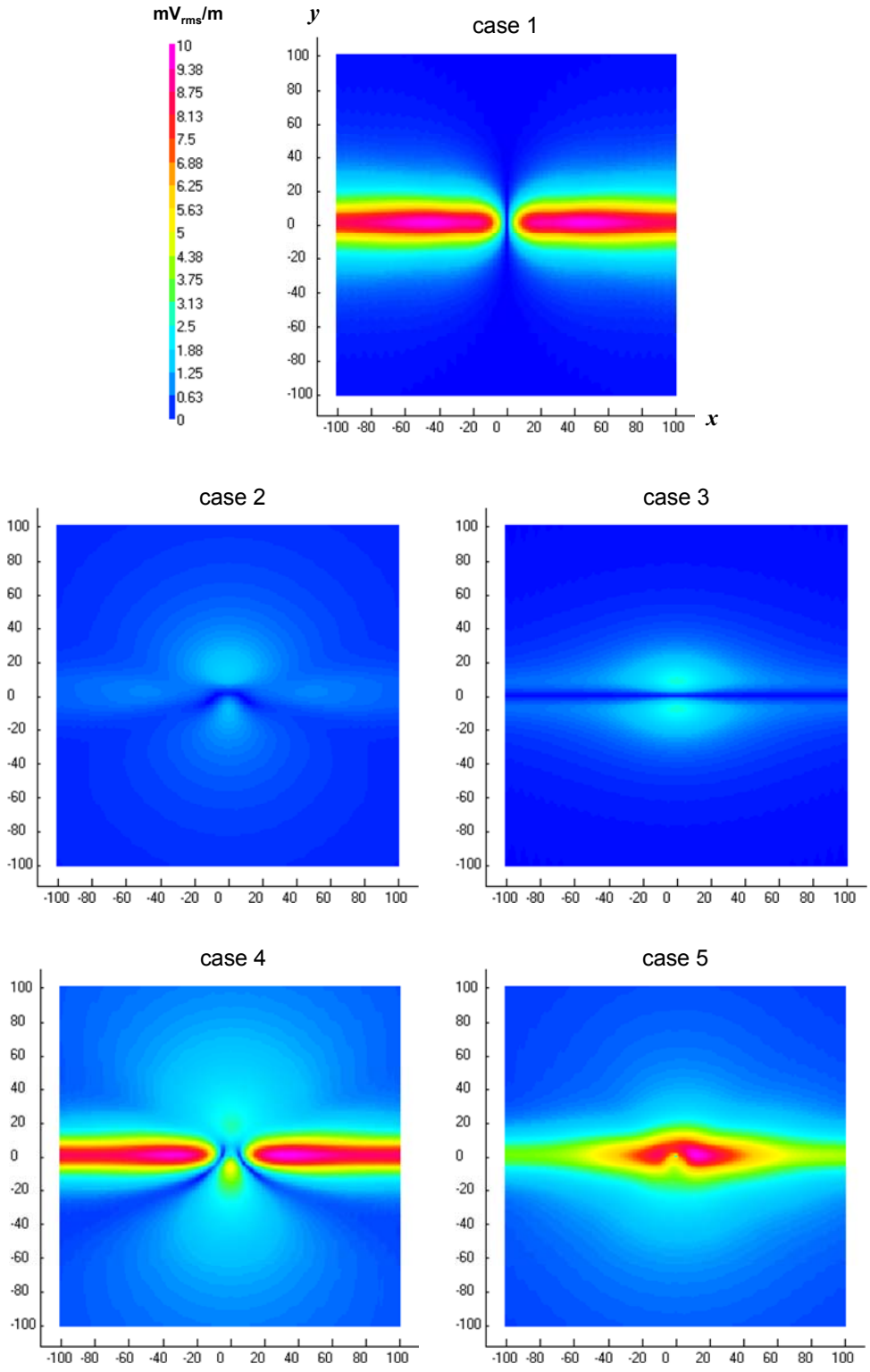

Figure 3.33 Same plots as Figure 3.32, except at 30 MHz.

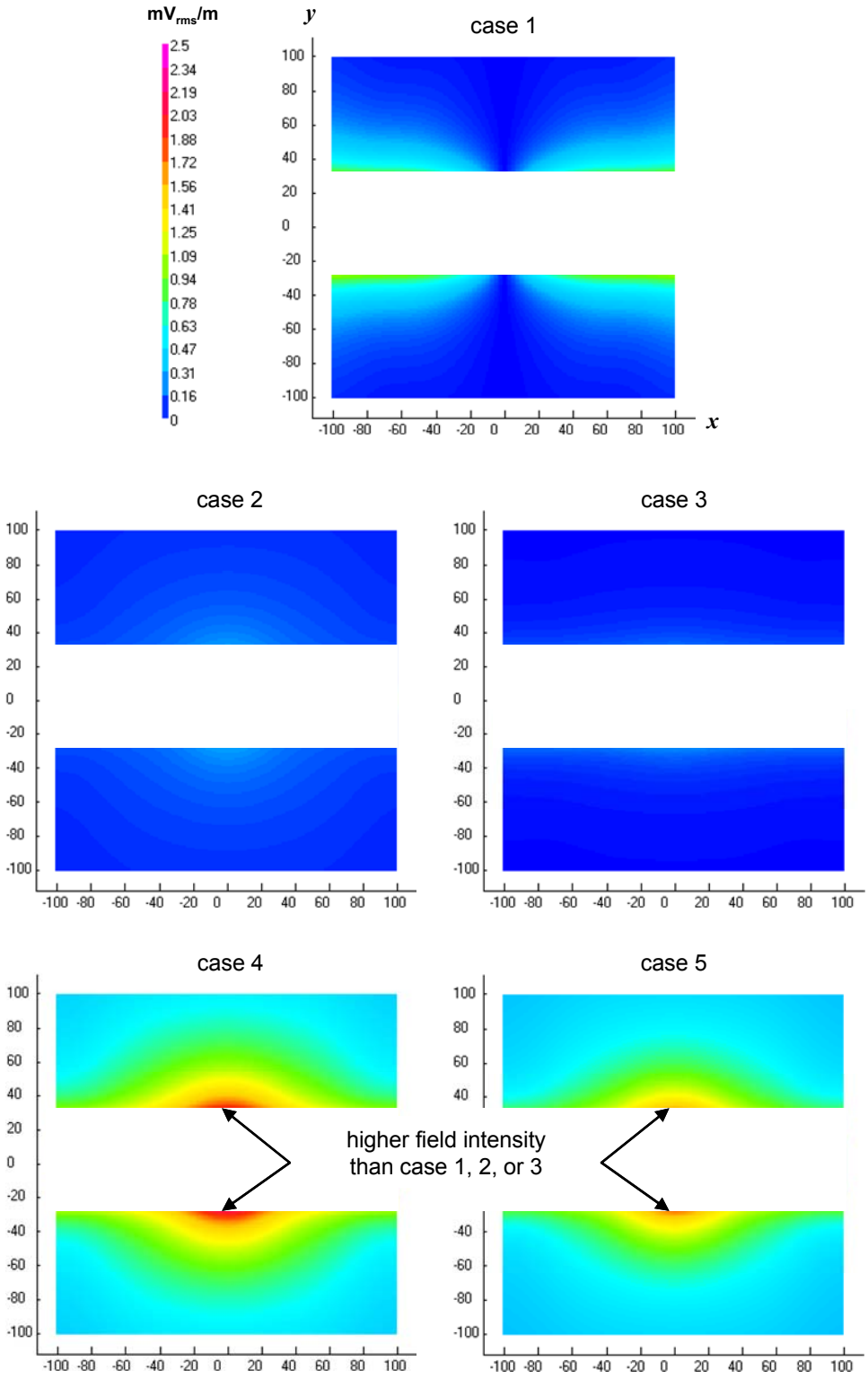

Figure 3.34 Same as Figure 3.32, except with omission of the fields in the region between the FCC lines and a scale adjustment.

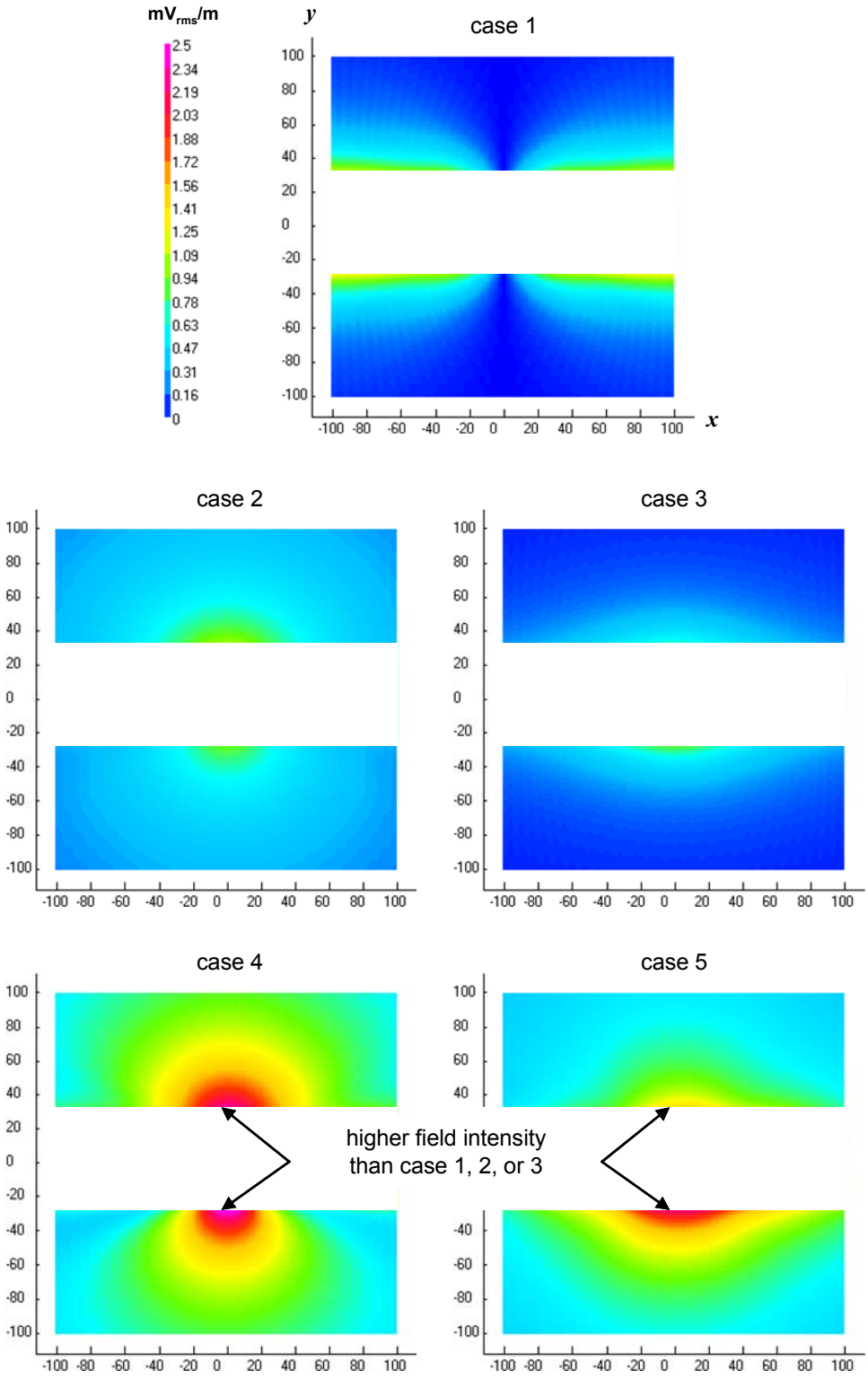

Figure 3.35 Same plots as Figure 3.34, except at 30 MHz.

Figures 3.36 through 3.39 compares the electric field intensities along the FCC lines at $z = 0$. It provides a more specific view of the surface plots shown previously. Figures 3.36 and 3.37 is for $y > 0$ while Figures 3.38 and 3.39 covers the $y < 0$ part. As can be seen among the figures, the scenario that has the highest peak intensity for both frequencies is case 4, with case 5 being a close second. Note that, other than case 1, the peak intensity occurs near the utility pole (along the longitudinal direction x) which reflects the impression obtained from the surface plots.

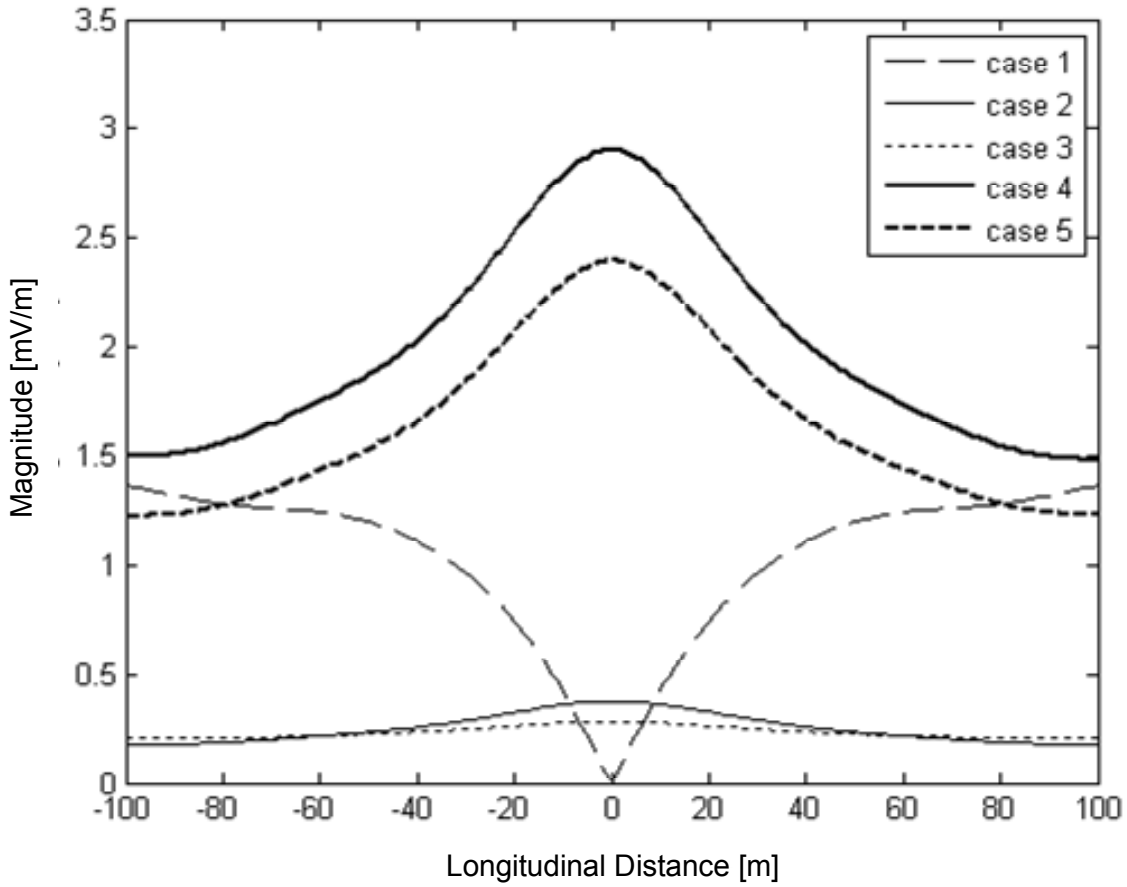

Figure 3.36 Electric field along earth ($z = 0$) for the five cases at 3 MHz from moment method 2 on the $y > 0$ side of the FCC lines.

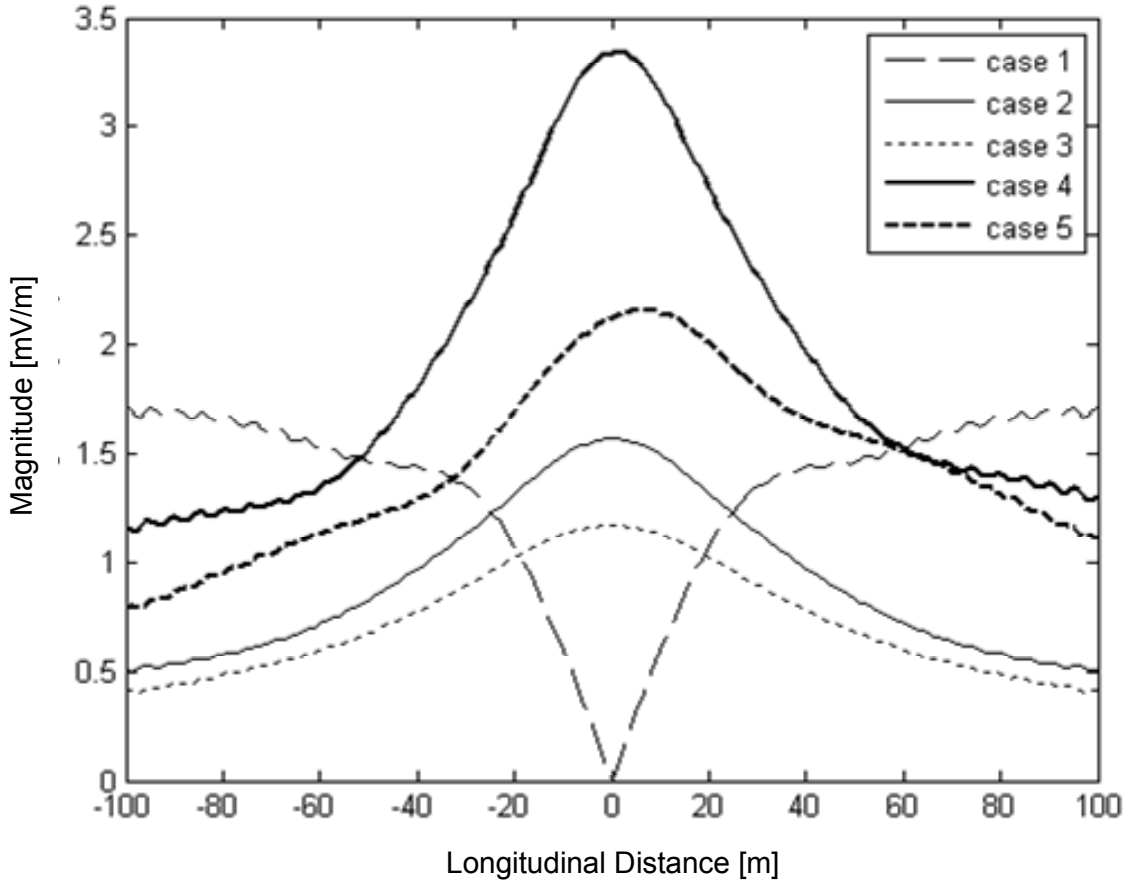

Figure 3.37 Same as Figure 3.36, except at 30 MHz.

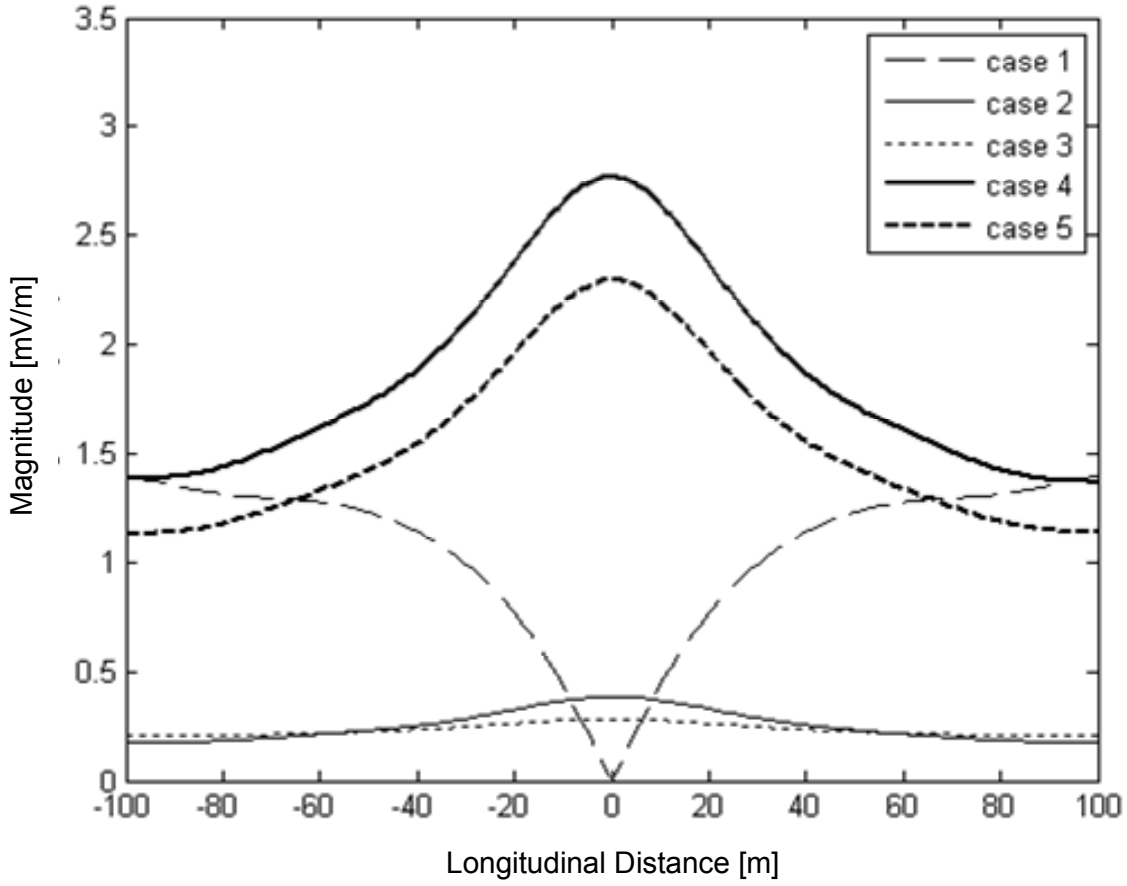

Figure 3.38 Same as Figure 3.36, except being on the $y < 0$ side of the FCC lines.

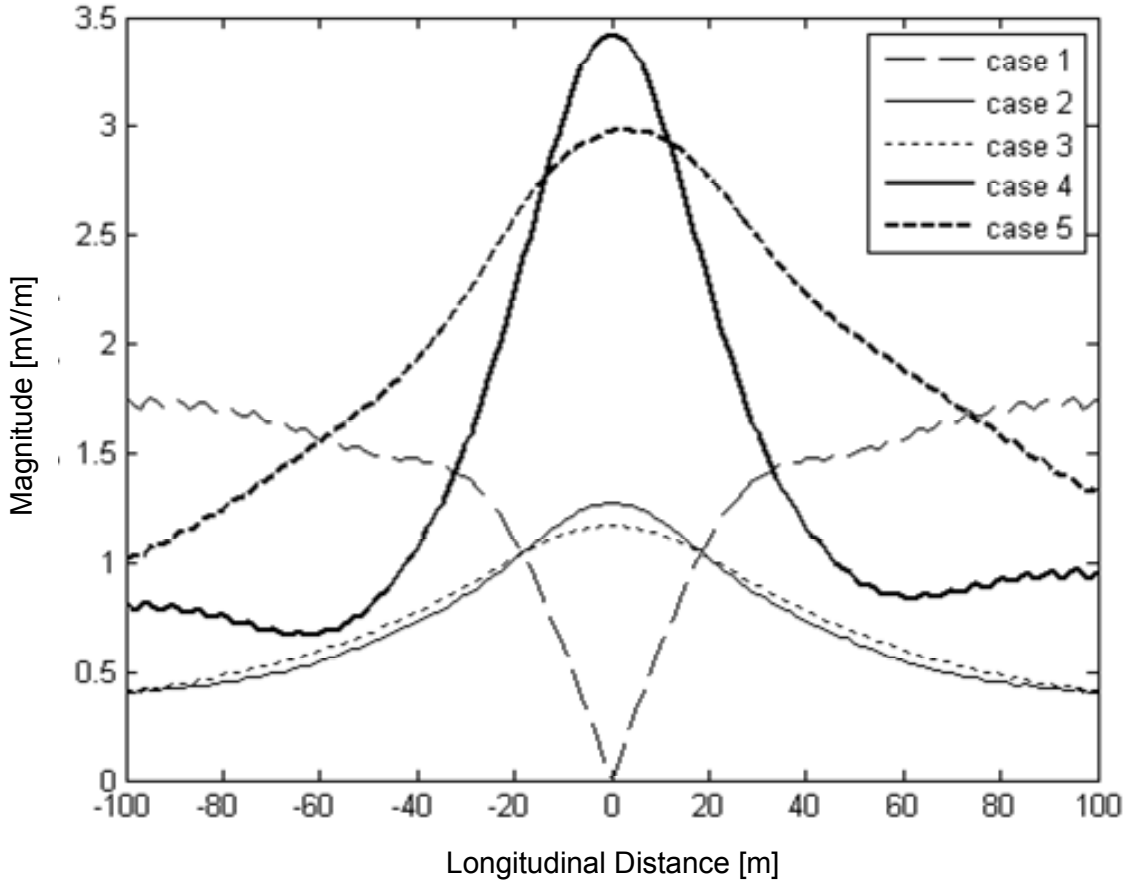

Figure 3.39 Same as Figure 3.38, except at 30 MHz.

Tables 3.2 and 3.3 show the terminal properties for a 1V source, and the peak electric field intensities for a 1W source, respectively, for the five cases, obtained from moment method 2 for 3 and 30 MHz. The Table 3.2 input power is based on the Table 3.1 input currents while Figures 3.36 through 3.39 provide the peak intensities. Table 3.2 also includes the input power for which the peak fields would meet the FCC regulation of 30 μV/m at a horizontal distance of 30 meters away from nearest power line. Table 3.3 is based on the Table 3.2 values and shows the peak intensity for the five cases for a device terminal that delivers 1W into the system. In general, an input power less than 100 nW

and 40 nW would satisfy the FCC regulations at 3 and 30 MHz, respectively. Field intensities are less than 90 to 150 mV/m when 1W is injected into the system, with case 5 being the highest. Case 4 produces the highest peak fields when the source is 1V, though case 5 produces the highest peak field when the source delivers a fixed 1W of power.

Table 3.2 Device terminal properties for the five cases, from moment method 2 at 3 and 30 MHz, using Figures 3.36 through 3.39 for the peak electric field intensities.

	case	current [mA]	power [mW]	peak E-field [mV/m]	power [μW] (for FCC)
3 MHz	1	1.16 + j 0.215	0.580	> 1.40	< 0.267
	2	3.58 – j 0.892	1.68	0.385	10.2
	3	3.34 – j0.425	1.67	0.285	18.6
	4	2.58 – j 1.34	1.29	2.90	0.138
	5	1.51 – j 1.64	0.757	2.40	0.119
30 MHz	1	1.77 + j 0.420	0.885	> 1.73	< 0.266
	2	0.617 – j 0.907	0.308	1.57	0.113
	3	1.26 – j 1.32	0.632	1.17	0.413
	4	1.49 + j 1.85	0.744	3.41	0.057
	5	0.813 – j 0.729	0.407	2.98	0.041

Table 3.3 Peak electric field intensities [mV/m] produced by a 1W device for the five cases, along the earth ($z = 0$) at the FCC lines. The results are calculated from moment method 2.

case	3 MHz	30 MHz
1	≅ 58.0	≅ 58.2
2	9.40	89.3
3	6.96	46.7
4	80.8	125
5	87.1	148

3.5 Summary

A summary of this chapter is presented in this section. The main concepts discussed in this chapter are as follows:

1) Based on the physical components, there are five principle connection methods, with each exemplified individually as a scenario case to be considered.
2) Reverse propagating current levels less than 0.4% of the respective forward propagating currents along truncated power lines are achievable from the presented technique involving placement of voltage sources near the endpoints.
3) For a given device terminal voltage, emission from case 4 is the strongest, while it is the strongest from case 5 for a given input power from the device.
4) Emission from case 3 is the smallest.
5) For systems involving capacitive couplers, the emission is strongest near the utility pole as the signal feed and pole grounding lines behave similar to vertical dipole antennas and produce strong radiation.

Chapter 4

Identification of the Currents

This chapter describes the identification of the various components of current that exist on the case 4 system model. The case 4 system model is of particular interest from an FCC regulation perspective and is a good frame to exemplify the different emission mechanisms. While the system models in previous chapters involve only the power lines directly connected to the signal feed line, the model in this chapter includes the remaining power line (passive) conductors to form a multiconductor system and refines the model of the physical system. Furthermore, the currents along each of the power lines that produce their respective traveling and space waves are identified in conjunction with the feed and grounding line currents to better illustrate the emission mechanisms. Figure 4.1 depicts the case 4 multiconductor system model where wires A and B are the newly introduced conductors that are not directly connected to the signal feed line, having coordinates from Table 2.1.

4.1 Traveling-Wave and Space-Wave Currents

Being that there is value in knowing the traveling-wave and space-wave currents along each power line, a discussion on these currents is presented in this section. Having the distinction between feed and grounding line currents as well as power line traveling and space-wave currents provides insight into the emission mechanisms through the fields produced in relation to their corresponding physical components. Fortunately, the feed line and grounding line currents have been identified in the previous chapter. Thus, only the traveling-wave and space-wave currents remain.

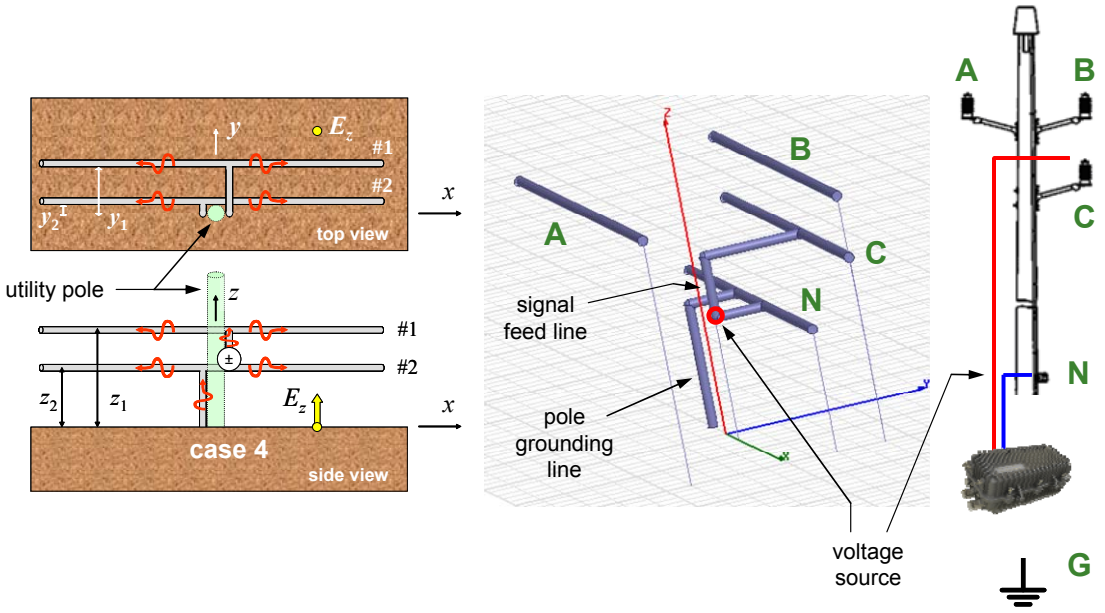

Figure 4.1 Concept of canonical model with (a) top and side as well as (b) 3D perspective views for (c) case 4 feed. Note that the utility pole is included for reference purposes only and not part of the model.

Basically, the approach for the space-wave currents is to find the balance between the traveling-wave currents extracted from the collected data and the respective total currents. For the traveling waves, the currents along the power lines are essentially complex constants from the junction to any given endpoint. On the other hand, currents for the space waves are generally complicated since they include near-field interactions. They are defined as the difference between the total currents on the lines and the traveling-wave currents on the lines. When sufficiently distant from any discontinuity, the space-wave current is inversely proportional to the distance squared [27]. By modeling these properties, a fit can be made using the collected data over a region sufficiently distant from either a junction or endpoint. The data fit provides the traveling-wave currents and, hence, the space-wave currents along the power lines.

In concert with the space-wave properties discussed, Figure 4.2 illustrates the concept of the model. Similar to the scenario in Figure 3.7, forward and reverse propagating traveling-wave and space-wave currents exist from a source at both the utility pole side of the power line as well as the endpoint, as shown in Figure 4.2(a). The reverse propagating currents are minimized from proper phasing, as shown in Figure 4.2(b), and this leaves predominantly forward-propagating currents, consisting of traveling-wave and space-wave currents with a minute amount of reverse currents, as shown in Figure 4.2(c). Thus, for a given geometric position that is sufficiently distant from any discontinuities, the total current can be modeled as

$$\bar{I}_m = \underbrace{\left(\underbrace{a_1}_{\text{trv}} + \underbrace{\frac{a_2}{(d_m - b_1)^2}}_{\text{space}} \right) e^{-jk_d d_m}}_{\text{forward propagating}} + \underbrace{\left(\underbrace{a_3}_{\text{trv}} + \underbrace{\frac{a_4}{(d_m - b_2)^2}}_{\text{space}} \right) e^{+jk_d d_m}}_{\text{reverse propagating}}, \tag{4.1}$$

where k_d as well as d are the same as defined for Equation (3.1) and $a_{i=1\to4}$ as well as $b_{i=1,2}$ are complex and real valued parameters, respectively, to be data fitted.

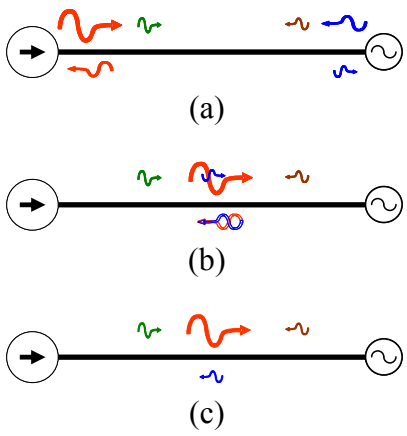

Figure 4.2 (a) Forward and reverse traveling-wave and space-wave currents with sources. (b) Reverse propagating current cancels. (c) Predominantly forward and some reverse traveling-wave and space-wave current remain.

4.2 Data Fitting

Using the currents obtained from moment method 1, this section describes the determination of the traveling-wave and space-wave currents along each power line through model fitting of the collected data. Considering the role that the bends and junctions have on the power line currents, there is preference to use data from moment method 1 since, as discussed in Section 3.3, the KCL is explicitly enforced. For given $b_{i=1,2}$ offset values, there exist $a_{i=1\to 4}$ values such that $\overline{I}_m$, rearranged from Equation (4.1) as

$$\overline{I}_m = a_1 \cdot e^{-jk_d d_m} + a_2 \cdot \frac{e^{-jk_d d_m}}{\left(d_m - b_1\right)^2} + a_3 \cdot e^{+jk_d d_m} + a_4 \cdot \frac{e^{+jk_d d_m}}{\left(d_m - b_2\right)^2} \ , \tag{4.2}$$

best fits the collected data.

For an "*n*" number of distinct geometric position points and collected data points, Equation (4.2) can be described in matrix form as

$$[I] - [\Delta] = \left[\overline{I}\right] = [T][a] \ , \tag{4.3}$$

with $[I]$ and $\left[\overline{I}\right]$ being a $n \times 1$ column of collected and modeled data points, respectively, $[\Delta]$ denotes a $n \times 1$ column of differences between collected and modeled data, $[a]$ is a 4×1 column of $a_{i=1\to 4}$ values, and

$$[T] = \begin{bmatrix} e^{-jk_d d_{m=1}} & \dfrac{e^{-jk_d d_{m=1}}}{\left(d_{m=1} - b_1\right)^2} & e^{+jk_d d_{i=1}} & \dfrac{e^{+jk_d d_{m=1}}}{\left(d_{m=1} - b_2\right)^2} \\ \vdots & \vdots & \vdots & \vdots \\ e^{-jk_d d_{m=n}} & \dfrac{e^{-jk_d d_{m=n}}}{\left(d_{m=n} - b_1\right)^2} & e^{+jk_d d_{i=n}} & \dfrac{e^{+jk_d d_{m=n}}}{\left(d_{m=n} - b_2\right)^2} \end{bmatrix} . \tag{4.4}$$

The form of Equation (4.3) can be viewed as a linear least squares problem, and hence

$$[\bar{a}] = \left(\left[T^* \right]^{\mathrm{T}} [T] \right)^{-1} \left[T^* \right]^{\mathrm{T}} [I] \ , \tag{4.5}$$

where $\left[T^* \right]^{\mathrm{T}}$ is the transposed complex conjugate of $[T]$ and $[\bar{a}]$ is the best estimate of $[a]$ given a selection of $b_{i=1,2}$ offset values. Based on Equations (4.3) through (4.5), the difference vector for a given set of coefficients $b_{i=1,2}$ can be calculated through

$$[\Delta] = [I] - [T] \left(\left[T^* \right]^{\mathrm{T}} [T] \right)^{-1} \left[T^* \right]^{\mathrm{T}} [I] \ . \tag{4.6}$$

Since $b_{i=1,2}$ are parameters related to the space wave currents at a sufficient distance away from either a junction or endpoint, there exist coefficients $b_{i=1,2}$ that will create a minimum set of differences. Therefore, the traveling-wave currents can be obtained from their respective a_i terms followed by a simple subtraction from the total currents to obtain the space-wave currents.

4.3 Results and Observations

In this section, the assumptions from Section 3.4 have been made so that quantitative values can be obtained to demonstrate the concepts discussed throughout the chapter. The only exception would be that the power line endpoints of moment method 1 are $15\lambda_0$ at 30 MHz (≈ 150 meters) away from the utility pole along the longitudinal direction x. Unless there are indications to the contrary, these assumptions are expected to provide sufficiently general conditions from which observations can be made.

Figures 4.3 through 4.6 compare the currents for the case 4 multiconductor system based on the Figure 4.1 model. In general, the passive conducting wires A and B in the Figure 4.1 is capable in supporting coupled currents in conjunction with wires C and N as

well as on the vertical signal feed and grounding lines, and thus are included in the model. Figure 4.3 illustrates the frequency effect on the distribution of current from moment method 1 along the vertical signal feed line and grounding wire, while Figure 4.4 pertains to the power lines. Figures 4.5 and 4.6 compare the currents obtained via the two moment methods for both power line wires at 3 and 30 MHz, respectively. The distributions of current along the 50 to 125 meter section of the power lines is relatively monotonic with reverse propagating currents being less than 0.2% and 0.4% of the forward current at 3 and 30 MHz, respectively. The agreement between the two moment

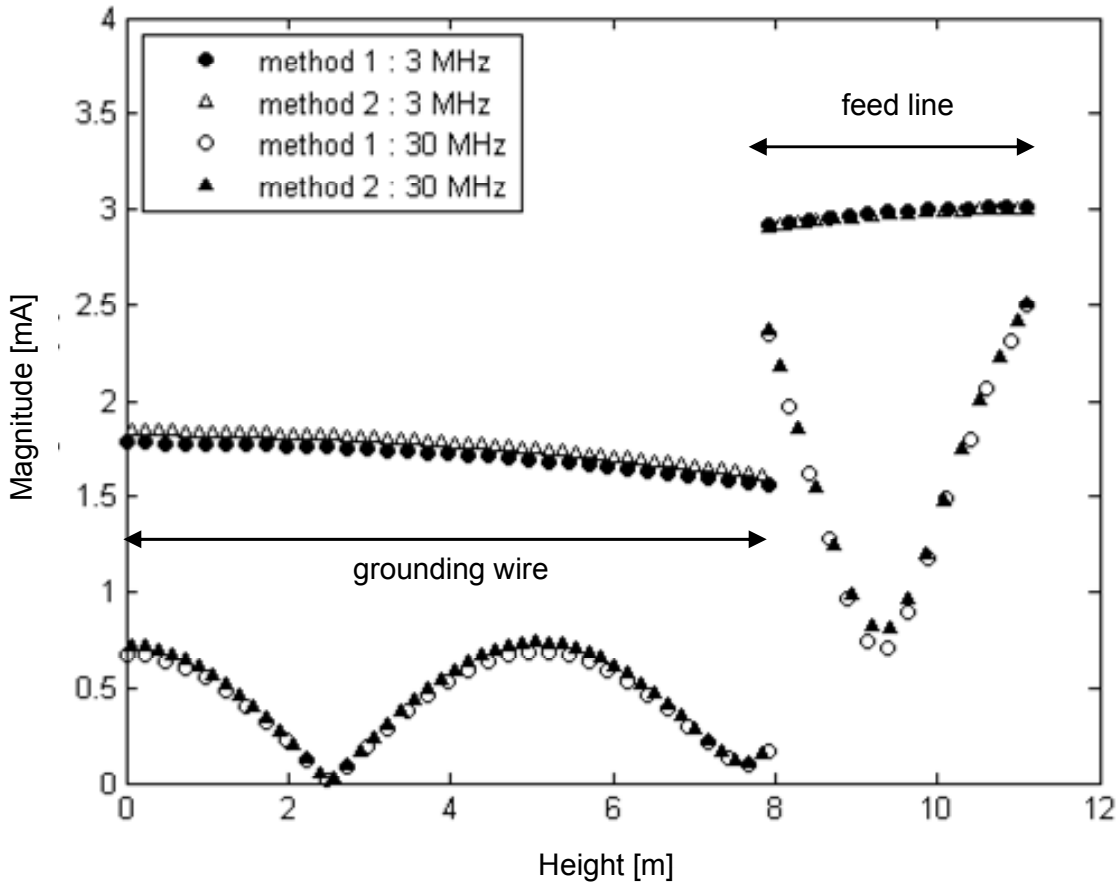

Figure 4.3 Currents along vertical signal feed line and grounding wire from both moment methods at 3 and 30 MHz.

methods at both frequencies is good, though better at 30 MHz than at 3MHz. Unlike Figure 3.23, Figure 4.4 shows that the unbalance of current between wires C and N is almost the same between frequencies, with the presence of current along wires A and B at 30 MHz and essentially none at 3 MHz. Note the strong similarity in profile between Figure 4.3 and Figure 3.22. This indicates that the presence of wires A and B does not significantly disturb the vertical currents and, subsequently, the associated fields or the device terminal power.

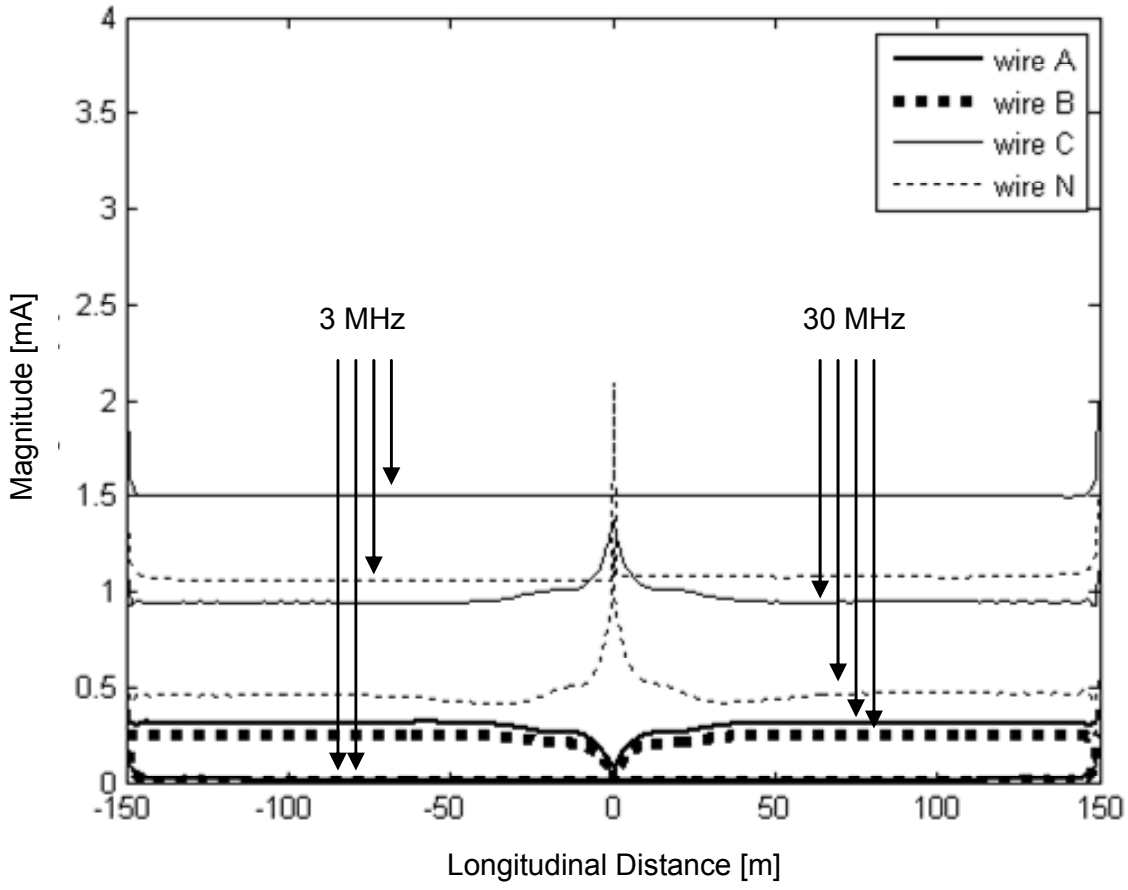

Figure 4.4 Currents along power lines from moment method 1 at 3 and 30 MHz.

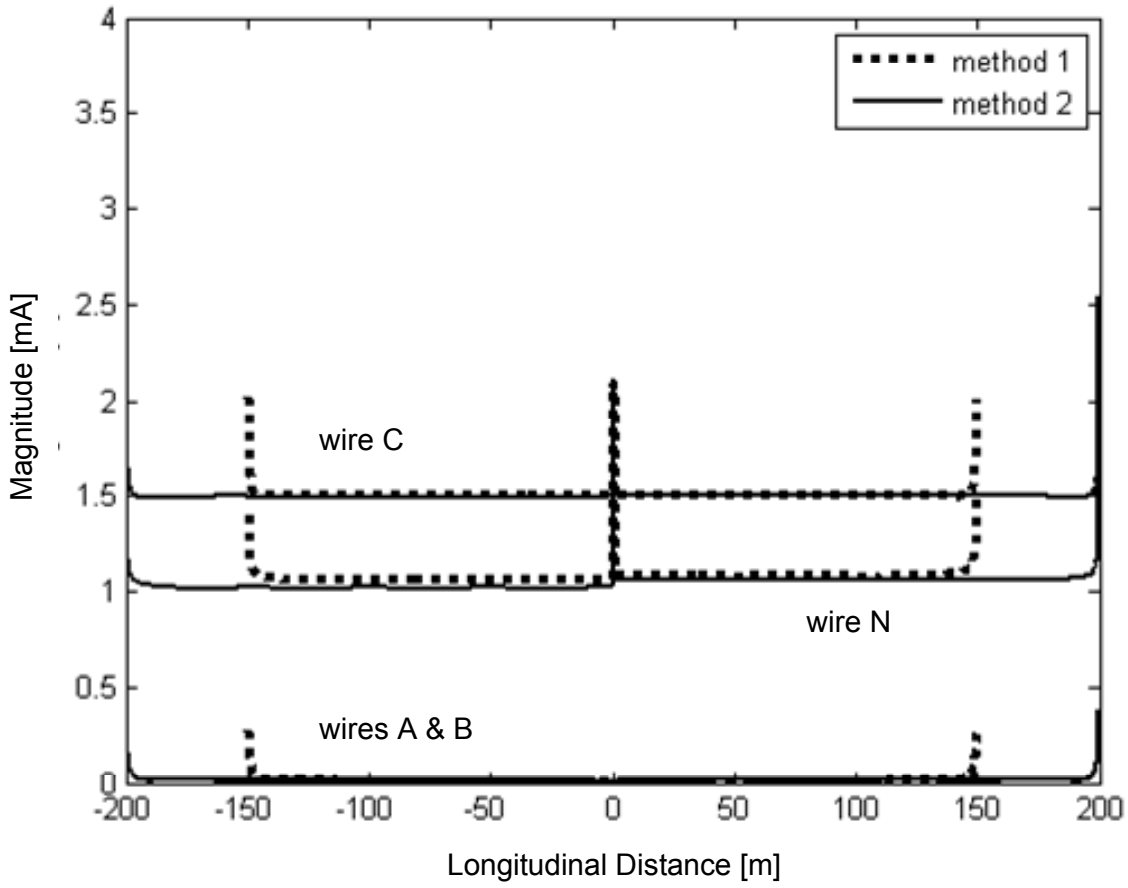

Figure 4.5 Currents along power lines from both moment methods at 3 MHz.

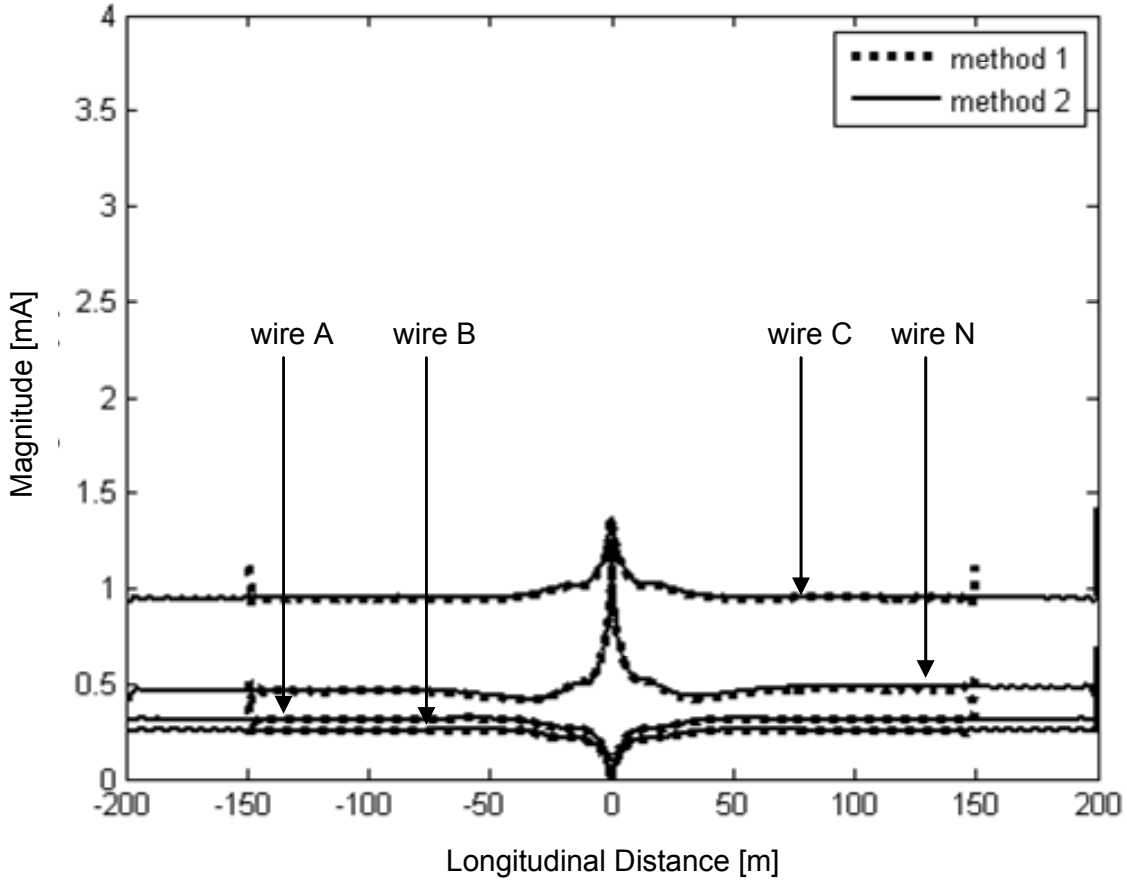

Figure 4.6 Same as Figure 4.5, except at 30 MHz.

Figures 4.7 and 4.8 compare currents between moment method 1 and the "data-fitted" model based on currents from moment method 1. Figure 4.7 reflects using only the forward propagating terms of Equation (4.1) at 3 MHz, while Figure 4.8 is for 30 MHz. Note that the data-fitted currents contain extrapolation to extend the values beyond the power line length used in moment method 1. Not only would this be consistent with the power line length used in moment method 2, it also allows for the truncation effects to be excised from the currents and, thereby, the fields. As portrayed in Figure 4.7, the peaks at the endpoints of the 3 MHz currents from moment method 1 do not appear in the

data-fitted currents. Similarly, the data-fitted currents in Figure 4.8 do not have such peaks at the endpoints, while preserving any forward propagating space-wave currents throughout the line. Considering Figures 4.5 through 4.8 together, it is apparent that the data-fitted currents are a good match at 3 MHz and even better at 30 MHz.

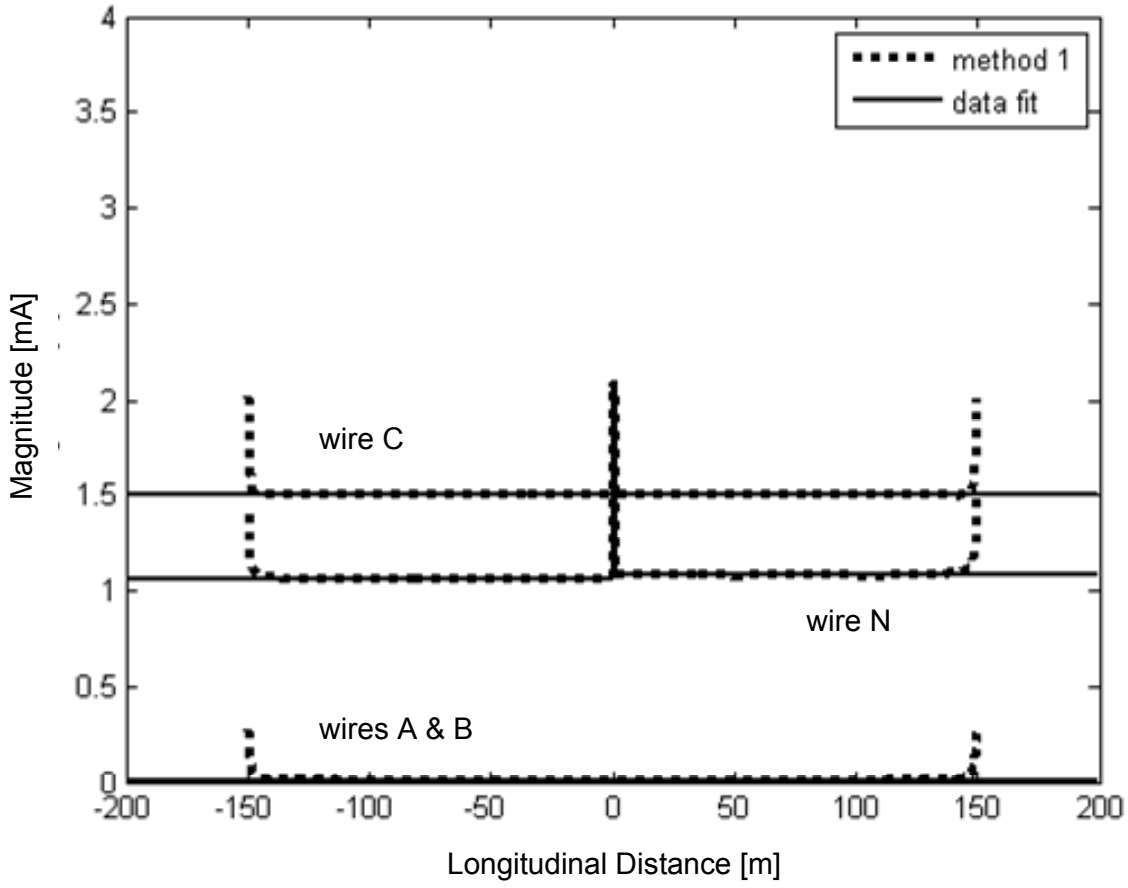

Figure 4.7 Currents along power line wires between moment method 1 and data-fitted model at 3 MHz.

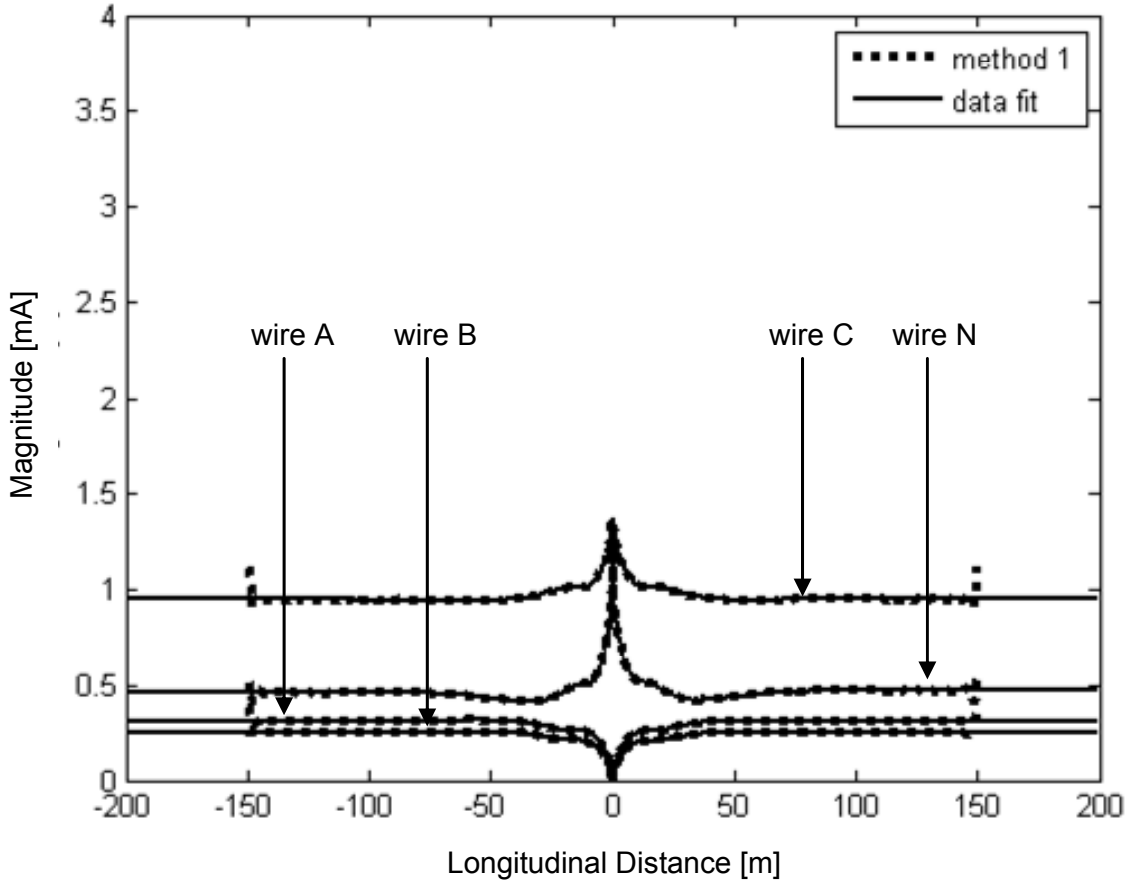

Figure 4.8 Same as Figure 4.7, except at 30 MHz.

Figures 4.9 through 4.12 compare the electric field intensities along the earth ($z = 0$) at the FCC lines for various components of current. Figures 4.9 and 4.10 are for $y > 0$ while Figures 4.11 and 4.12 covers the $y < 0$ side of the FCC lines at 3 and 30 MHz, respectively. Throughout the figures, the fields shown are those directly obtained from moment method 2 as well as from composites of its constituent parts from the various components of the current on the system defined as the following:

- Vertical directed currents ("verticals") from the vertical signal feed line and vertical grounding wire.

- Power line currents from wires A, B, C, and N ("A+B+C+N").
- Power line and vertical directed currents ("ABCN+V").
- Power line, vertical directed, and horizontal directed currents that are not on the power lines ("ABCNV+H").

As can be seen, the fields due to the vertical currents of the feed and grounding lines have a significant impact on the overall intensity. Note that the peak of the field intensity with

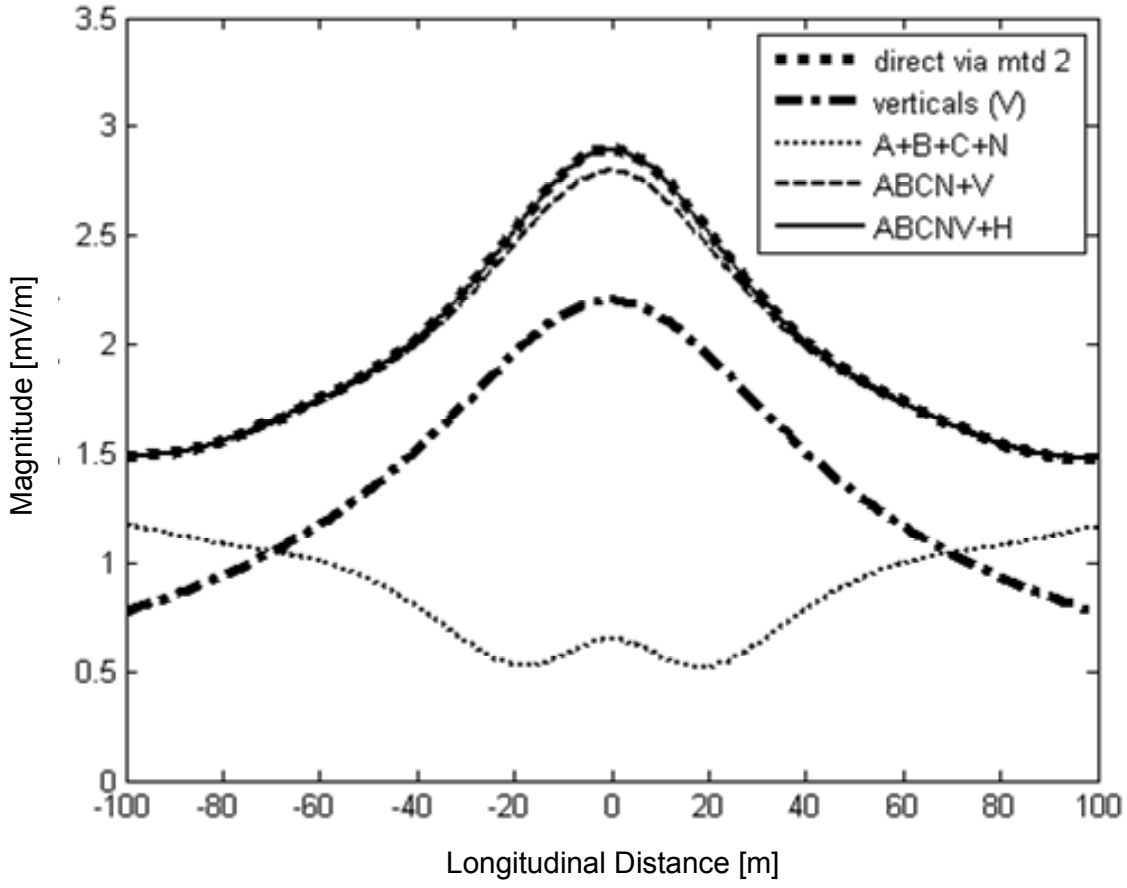

Figure 4.9 Electric field along the earth (z = 0) at 3 MHz from components of moment method 2 currents on the $y > 0$ side of the FCC lines. Note that "H" represents all horizontal currents that are not on the power lines.

the vertical currents is much higher than the other components of current when near the utility pole along the longitudinal direction *x*. A similar phenomenon illustrated in Figures 3.32 and 3.33 with surface plots can thereby be attributed to the vertical currents.

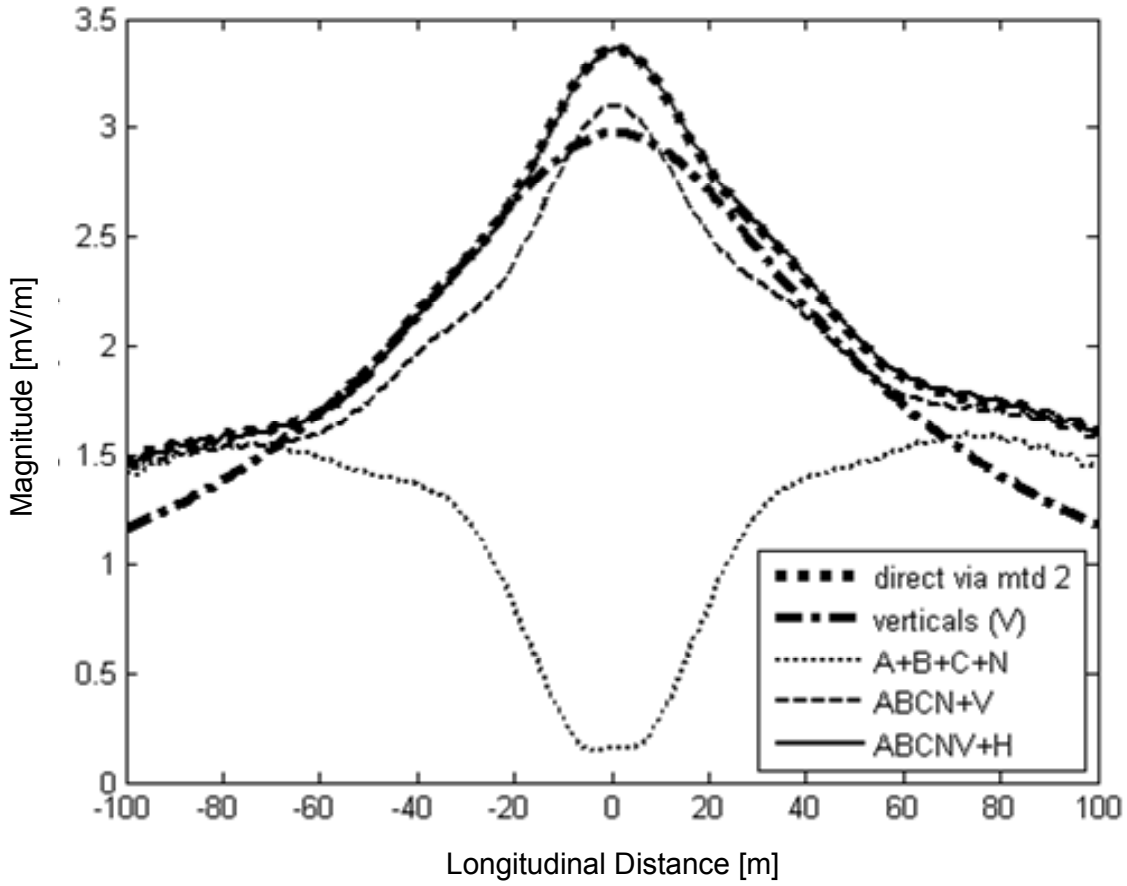

Figure 4.10 Same as Figure 4.9, except at 30 MHz.

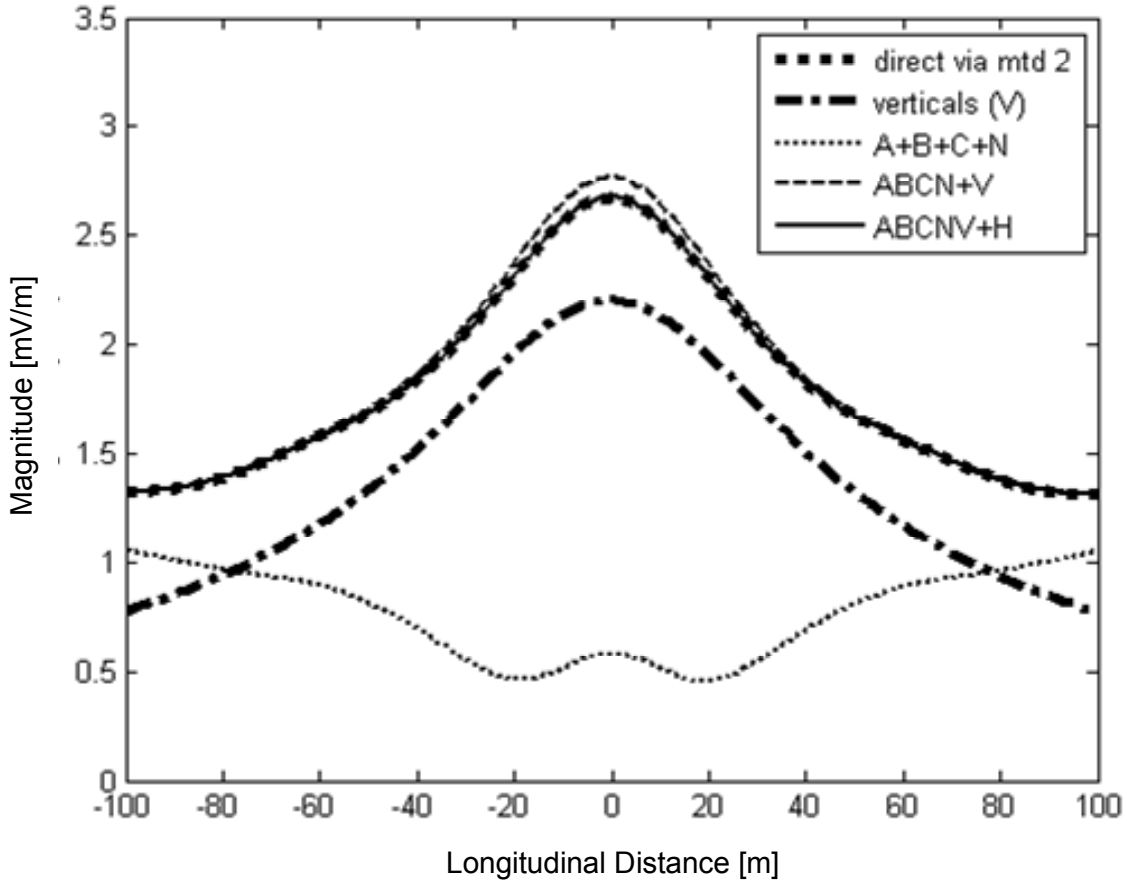

Figure 4.11 Same as Figure 4.9, except being on the $y < 0$ side of the FCC lines.

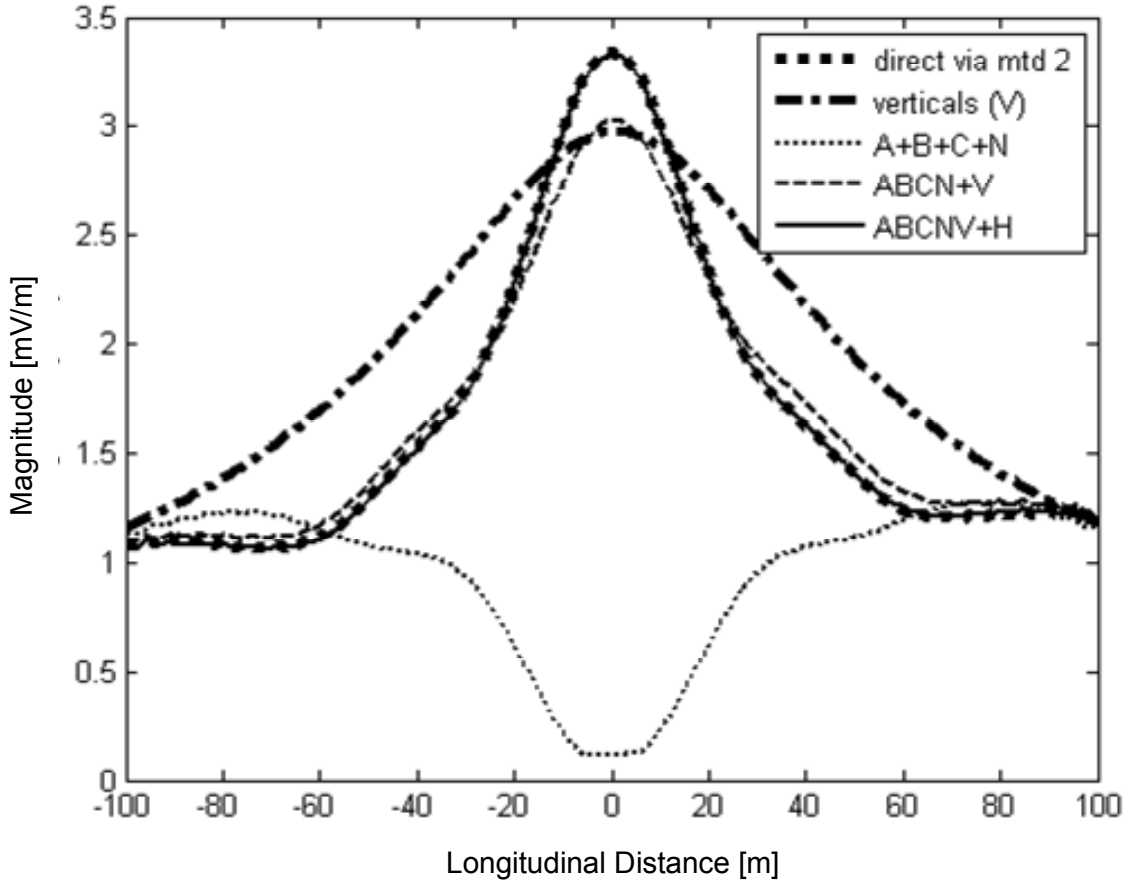

Figure 4.12 Same as Figure 4.11, except at 30 MHz.

Figures 4.13 and 4.14 compare the electric field intensities along the earth ($z = 0$) at the FCC lines between moment method 2 and data-fitted (via moment method 1) currents. Corresponding fields for case 5 (without passive conductor wires A and B) from Figures 3.34 through 3.37 had been included as reference. With the power line currents between moment methods generally having a closer agreement than their respective feed line currents, it can be seen that the fields match nicely when away (along the longitudinal direction x) from the utility pole while differences are more apparent near the utility pole. Note that the peak intensity of case 4 is higher than case 5, though

more distinctly at 3 MHz than at 30 MHz as depicted in Figures 4.13 and 4.14 respectively, and is near (along longitudinal direction x) the utility pole, which is not significantly affected by wires A and B. This provides assurance that case 4 should remain the scenario for further study.

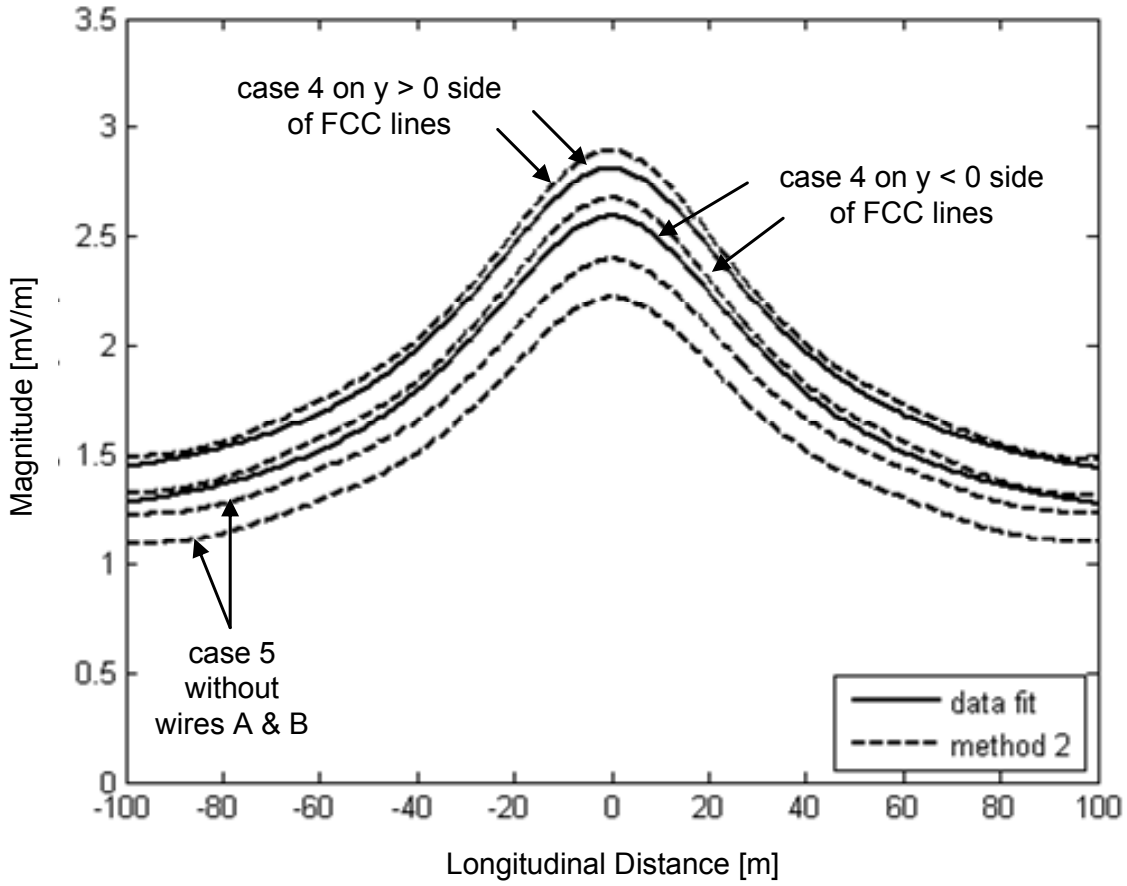

Figure 4.13 Electric field along the earth (z = 0) at 3 MHz on the FCC lines from moment method 2 and the data-fitted model currents. Inclusion of case 5 without passive wires A and B is only for reference.

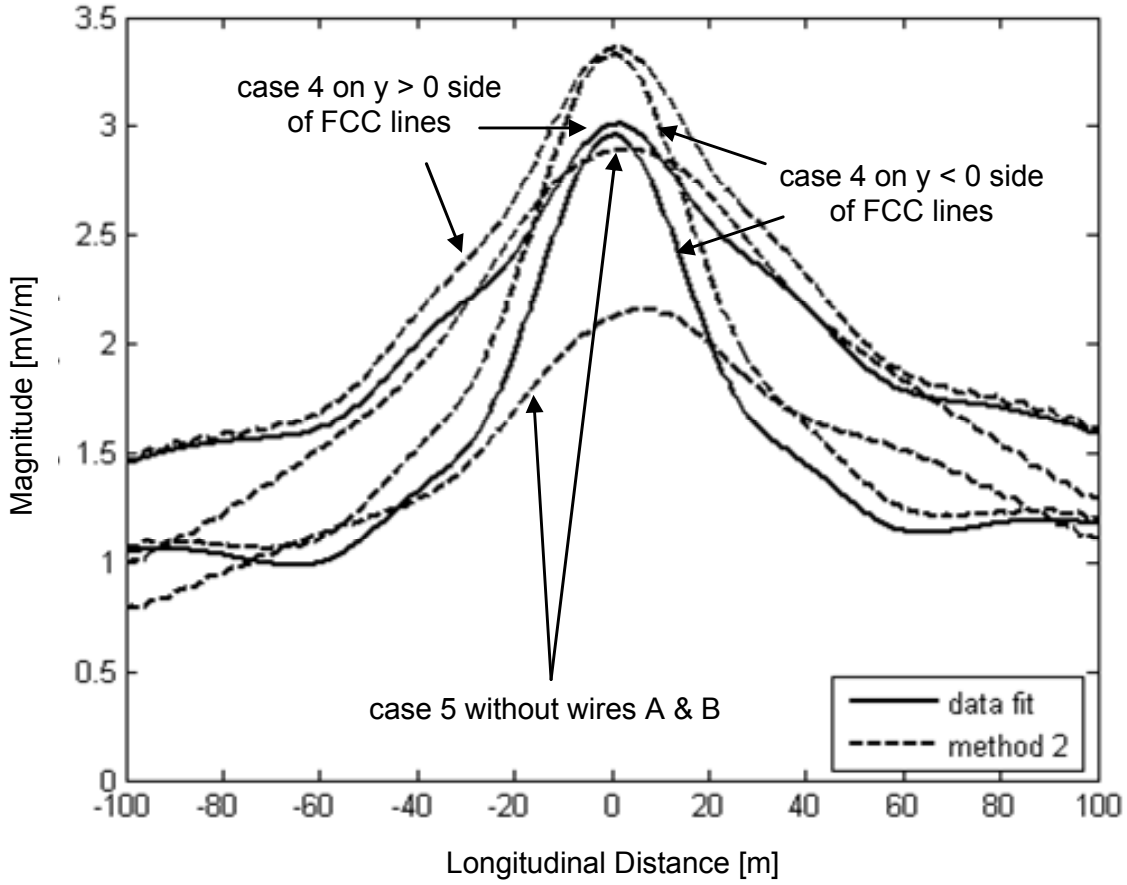

Figure 4.14 Same as Figure 4.13, except at 30 MHz.

Figures 4.15 and 4.16 illustrate the traveling-wave and space-wave currents, respectively, at 30 MHz from the data fit based on currents from moment method 1. For comparison purposes, Figure 4.15 includes the moment method 1 currents along with the data-fitted traveling-wave current, a_1, of Equation (4.1). Figure 4.16 shows the space-wave currents, where the values within 75 meters (along the longitudinal direction x) of the utility pole are from the difference between the total and traveling-wave currents, while model-extrapolated values based on the forward-propagating space-wave term of Equation (4.1) are shown for greater distances. The extrapolation effectively excises any

reverse propagating space-wave currents, which are responsible for the peaks at the truncation endpoints. Note the asymmetry in the traveling-wave current as well as the distribution of the space-wave currents between opposite directions (along the longitudinal direction x) from the utility pole.

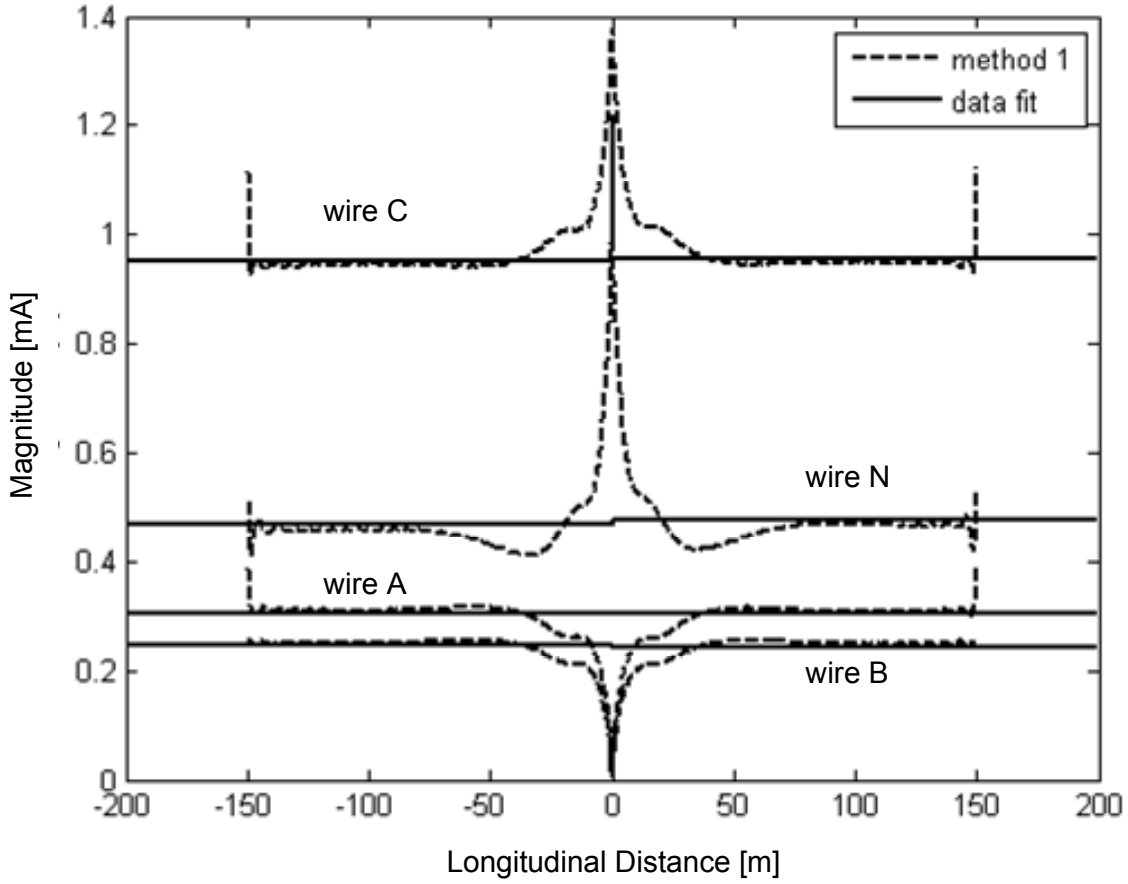

Figure 4.15 Currents corresponding to traveling-waves along the horizontal power line wires at 30 MHz from the data-fitted model. Inclusion of currents from moment method 1 is only for reference.

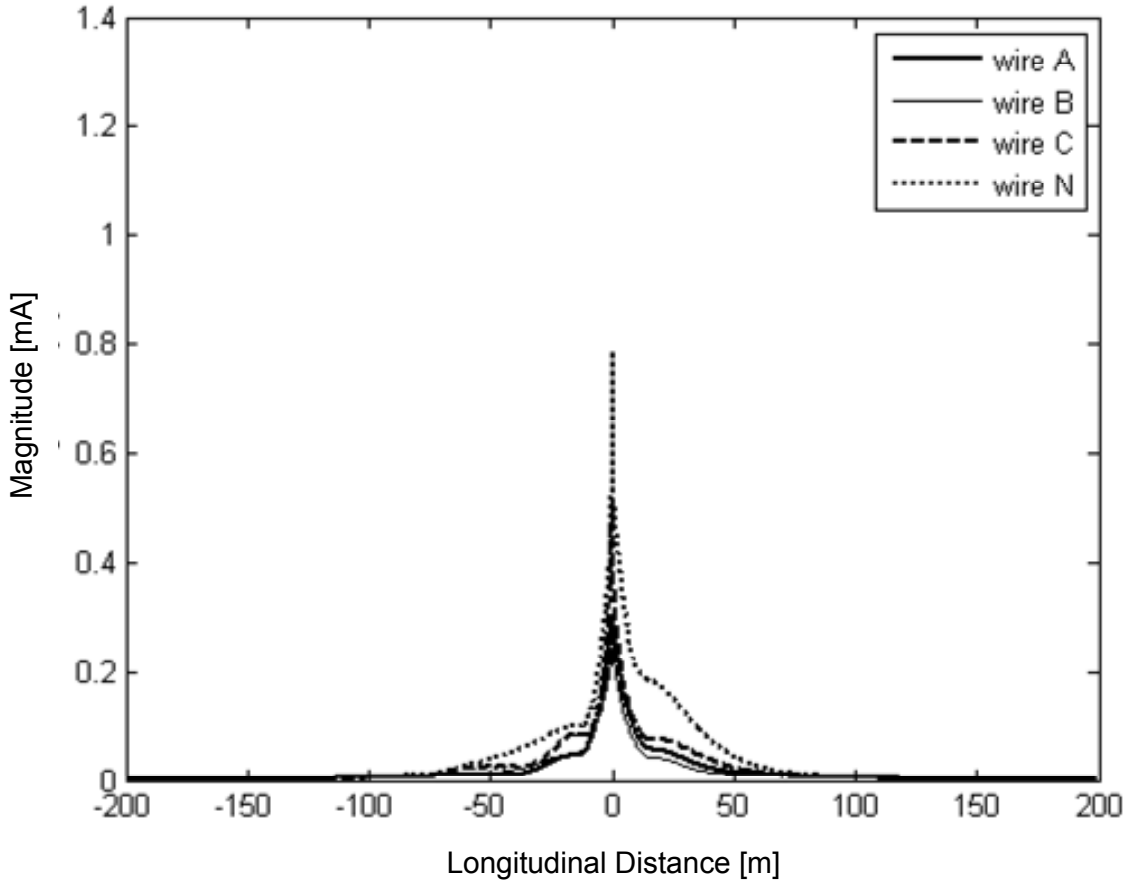

Figure 4.16 Currents corresponding to space-waves along the horizontal power line wires at 30 MHz from the data-fitted model.

Tables 4.1 and 4.2 show the traveling-wave currents from the data-fitted model and the terminal properties for a 1V source, respectively, for both frequencies. The traveling-wave currents along each power line between opposite directions from the utility pole shown in Table 4.1 have slight differences, with the exception of the neutral wire at 30 MHz. The Table 4.2 input power is based on the input currents from moment method 2 and the data-fitted model, while Figures 4.13 and 4.14 provide the peak intensities. It also includes the input power for which the peak field intensity would meet

the FCC regulation. Note the similarity in values between moment method 2 and the data-fitted model.

Table 4.1 Traveling-wave current [mA] at 3 and 30 MHz along the power lines from moment method 1.

	3 MHz		30 MHz	
wire	$x < \rho_{\text{utiity pole}}$	$x > \rho_{\text{utiity pole}}$	$x < \rho_{\text{utiity pole}}$	$x > \rho_{\text{utiity pole}}$
A	0.0106	0.0106	0.305	0.303
B	0.00840	0.00925	0.246	0.245
C	1.51	1.50	0.951	0.956
N	1.06	1.08	0.468	0.478

Table 4.2 Device terminal properties from moment method 2 and the data-fitted model at 3 and 30 MHz, based on Figures 4.13 and 4.14 field intensities.

	mtd	current [mA]	power [mW]	peak E-field [mV/m]	power [nW] (for FCC)
3 MHz	fit	2.54 – j 1.44	1.27	2.81	144
	2	2.58 – j 1.34	1.29	2.89	139
30 MHz	fit	1.29 + j 1.95	0.647	3.01	64.3
	2	1.47 + j 1.85	0.735	3.36	58.5

Figure 4.17 compares the electric field intensities along the earth ($z = 0$) at 30 MHz on the $y > 0$ side of the FCC lines. The fields that have been decomposed into their constituent parts from the various components of the current on the system, defined as the following along with the total field ("sum"):

- Vertical currents ("verticals") from the vertical signal feed line and the vertical grounding wire.
- Horizontal currents ("horizontals") from horizontal wires that connect the vertical wires to the power lines.

- Traveling-wave currents ("traveling") on the power lines (A, B, C, N).
- Space-wave currents ("space") on the power lines (A, B, C, N).

As illustrated, the field from the "horizontals" near (along the longitudinal direction x) the utility pole is influential to the "sum". Note that the radiated field from the space-wave current is comparable to the emitted field of the traveling-wave current as well as the total field.

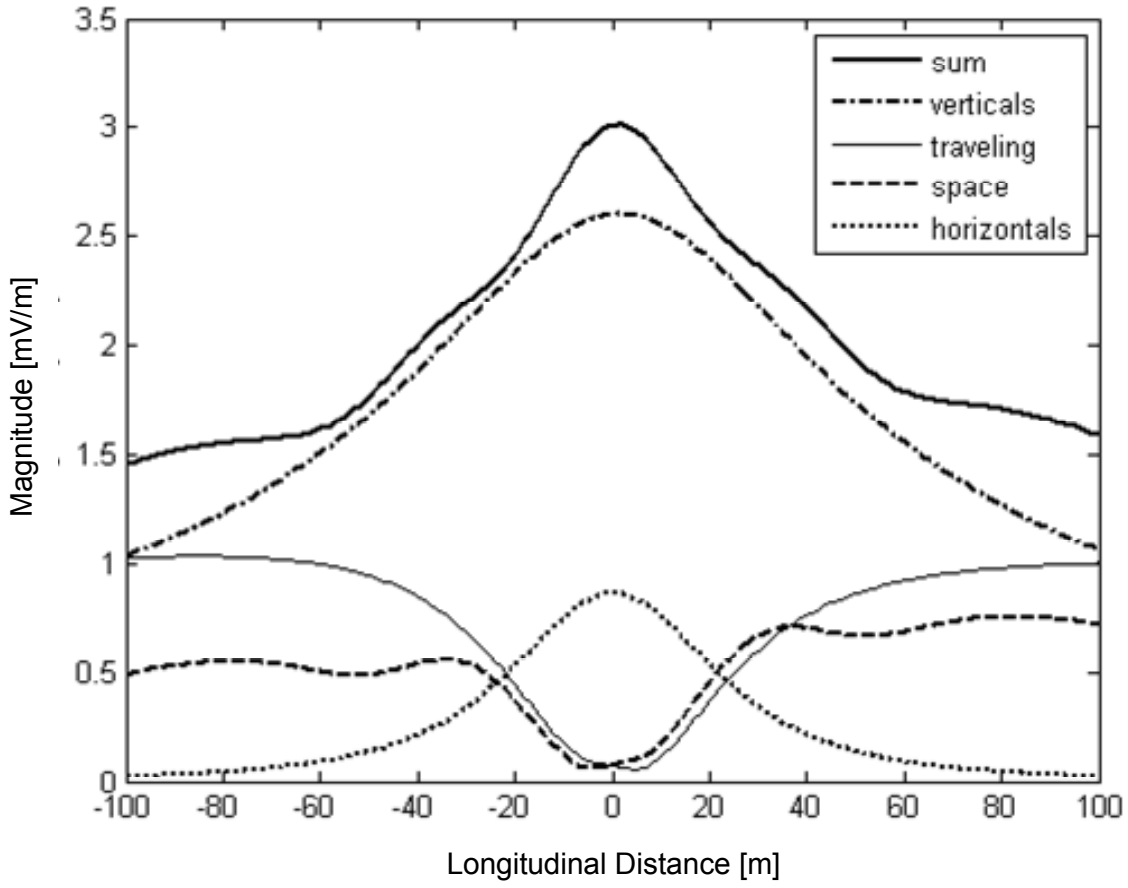

Figure 4.17 Electric field along the earth (z = 0) at 30 MHz due to horizontal (excluding power lines) and vertical currents, comparing with traveling-wave and space-wave currents on the $y > 0$ side of the FCC lines.

Figure 4.18 compares the electric field intensities along the earth ($z = 0$) at 30 MHz on the $y > 0$ side of the FCC lines. It highlights the proportion of the overall field of the vertical and horizontal currents, shown in Figure 4.17, to the following components:

- Vertical currents from the vertical signal feed line ("vert , sig").
- Vertical currents from the vertical grounding wire ("vert , gnd").
- Horizontal currents from horizontal wire that connect the vertical signal feed line to power line wire C ("horz , C").

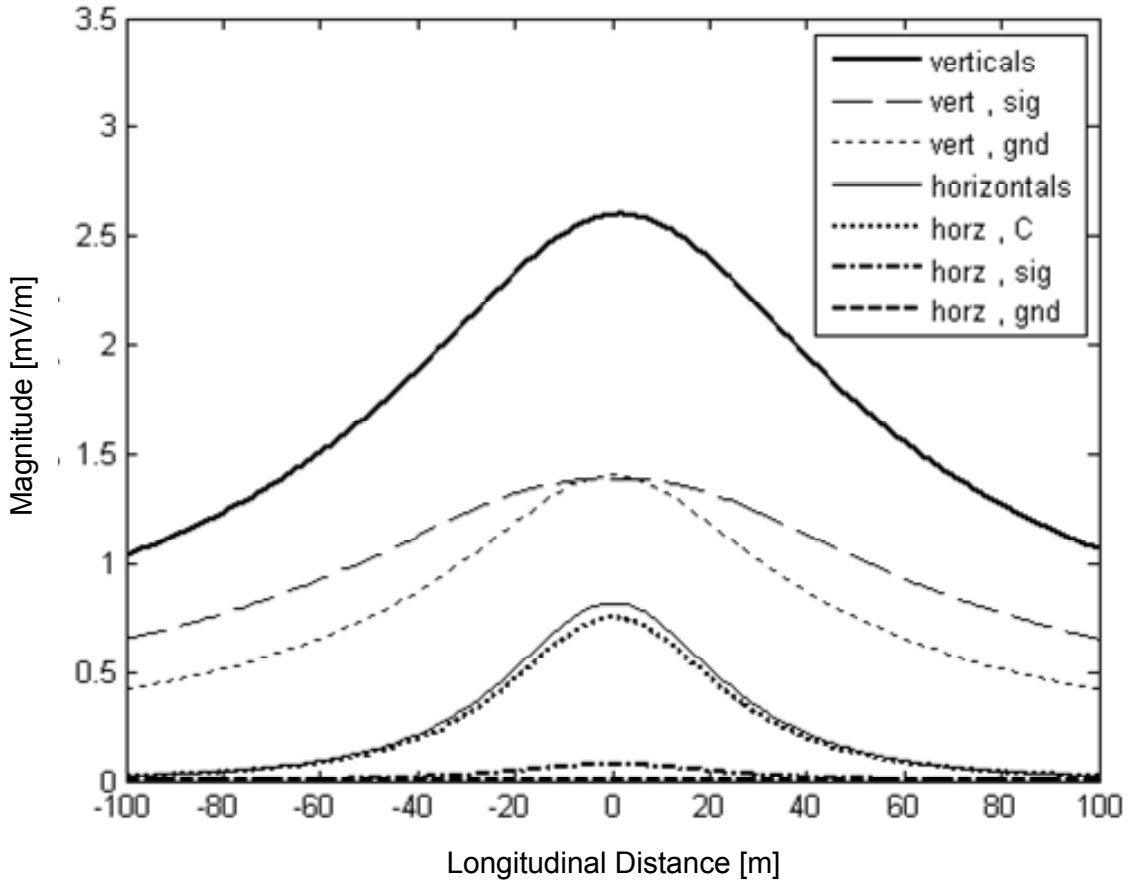

Figure 4.18 Same as Figure 4.17, except comparing fields due to various components of the horizontal and vertical currents.

- Horizontal currents from horizontal wire that connect the vertical signal feed line to power line wire N (“horz , sig”).
- Horizontal currents from horizontal wire that connect the vertical grounding wire to power line wire N (“horz , gnd”).

It can be seen that the current along the horizontal wire (about 0.8 meters long) that connects the vertical signal feed line to power line wire C is the main contributor to the “horizontals” field, which is influential to the sum near (along the longitudinal direction *x*) the utility pole. Note that the vertical current from the grounding wire is a strong contributor to the overall field of the vertical currents, especially near the utility pole.

4.4 Summary

A summary of the chapter is presented in this section. The main concepts discussed in this chapter are as follows:

1) Considering a fixed voltage source, the case 4 system model would be of most interest from an FCC regulation perspective, as it has the strongest fields.
2) The inclusion of power lines that are not directly connected to the signal feed lines does not significantly affect the vertical feed and vertical grounding line currents.
3) The fields from vertical currents have the most impact on the peak field emission.
4) The input power limits for FCC compliance are not significantly affected by the passive power lines that are not directly connected to signal feed lines.
5) The input power limits for the emitted fields to be FCC compliant are 144 nW and 64 nW at 3 and 30 MHz, respectively.

6) The model for the traveling-wave and space-wave currents fit well to the actual power line currents.
7) The presence of space-wave currents at 30 MHz confirms increased radiation at this frequency.
8) The induced currents on wires A and B increases the common-mode and differential-mode traveling-wave currents between wire C and neutral.
9) Greater emissions along the surface of the earth will occur with an increased presence of a common-mode current, corresponding to an increase in the unbalance of traveling-wave currents between wire C and the neutral wire.

Chapter 5

Calculations of Field Emissions

This chapter describes the inclusion of a finite-conductive earth and the presence of a receiving system on the case 4 multiconductor system model. Thus far, the earth has been modeled as a PEC, which may not always be valid, depending on the frequency and the type of field calculation. When allowing for the earth to have a finite conductivity, the use of simple image theory is no longer appropriate, and a more general method that allows for the inclusion of layered media is necessary. The method used here is the spectral domain immittance (SDI) method. As done previously, voltage sources are placed very close to the ends of the lines in order to minimize reflected currents from the line truncation.

The first section in this chapter details the formulation for a transmitter system only (TX-only) configuration with infinitely long power lines over a PEC earth, with the second section being for the same configuration except over a finite-conductive earth. This is followed by a section discussing a configuration involving both transmitter and receiver systems (TX-RX). For the case of a transmitting BPL source and no receivers, TX-only, the four lines (A, B, C, N) are assumed to be infinite, and the traveling-wave currents on them are semi-infinite, as noted in Equation (5.1) of this chapter. As discussed in Chapter 3, a finite "cell" is actually modeled, using voltage sources at the ends of the lines in order to minimize reflections. From a numerical solution of this finite cell system the amplitude of the semi-infinite traveling-wave currents are identified, along with the amplitude of the space wave currents on the lines and the currents on the vertical wires and the horizontal connector wires. The currents are calculated assuming a

PEC earth. The fields from these currents are then calculated using the formulas presented in Section 5.2 of this chapter for a finite-conductive earth. For a PEC earth, the formulas detailed in Section 5.1 as well as previously presented in Chapter 2 (based on image theory) are used.

5.1 Transmitter System Only: PEC Formulation

As discussed in Section 2.2, image theory greatly simplifies the analysis for a PEC earth, and details are presented in this section. With the scattered fields due to the earth found from the fields produced by the currents on the image conductors, the total field at and above the earth is obtained from a superposition of all the physical and image conductor currents. Figure 5.1 depicts the scenario for case 4 with infinite power lines while Figure 5.2 illustrates the model after application of image theory.

Since Table 4.1 indicates that differences exist in the two traveling-wave currents on opposite sides of the utility pole in the x direction, they are modeled as semi-infinite line currents that are each described by

$$I^{travel}(x) = I_0^{travel}\, e^{-jk_{x0}|x-x_0|}\, u(x-x_0)\ , \tag{5.1}$$

where k_{x0} is the wavenumber of the traveling-wave current I_0^{travel} that begins at x_0 and the function u denotes the unit step function. The 1D Fourier transform of such a current is

$$\tilde{I}^{travel}(k_x) = \frac{j}{k_x - k_{x0}} I_0^{travel}\ . \tag{5.2}$$

Combining Equations (2.2), (2.3), and (5.2), the E_z field component for the traveling-wave current is

$$E_z^{travel} = \frac{(z-z_i)}{\rho_x}\frac{1}{j\omega\varepsilon}\frac{\partial}{\partial\rho_x}\frac{\partial}{\partial x}\left(\frac{1}{j8\pi}\int_{-\infty}^{+\infty} I_0^{travel}\frac{j}{k_x-k_{x0}}\, H_0^{(2)}\left(k_{\rho_x}\rho_x\right)\, e^{-jk_x(x-x_0)}dk_x\right)\ . \tag{5.3}$$

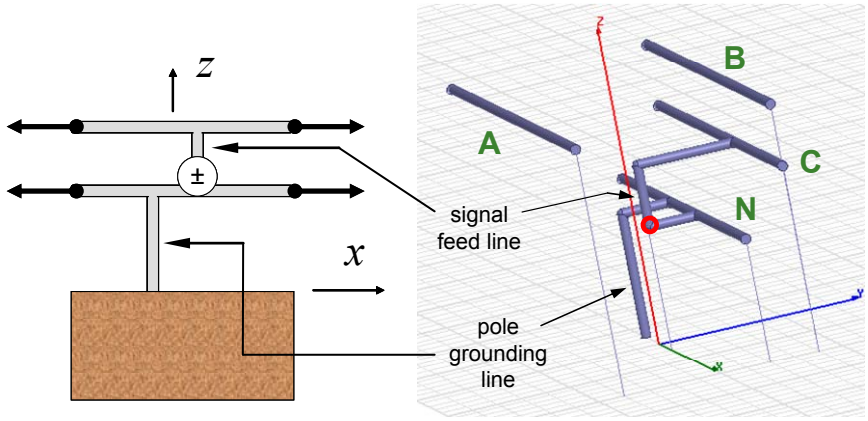

Figure 5.1 Concept of case 4 canonical model with (a) side and (b) 3D perspective views.

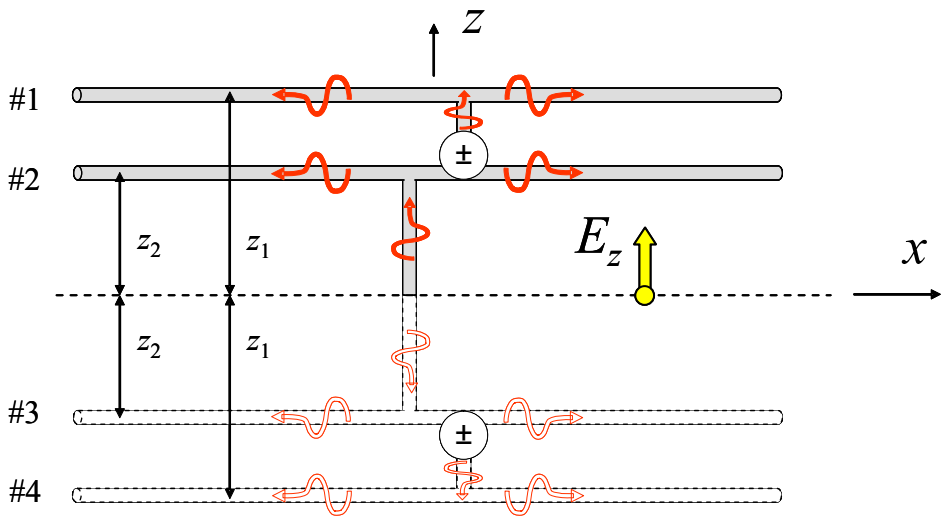

Figure 5.2 Side view of canonical model concept for case 4 after applying image theory. Power lines directly connected to the signal feed lines are used for illustration purposes.

After some simplification, it can be expressed as

$$E_z^{travel} = \frac{(z-z_i)}{\rho_x}\frac{I_0^{travel}}{8\pi\omega\varepsilon}\int_{-\infty}^{+\infty}\frac{k_x k_{\rho_x}}{k_x - k_{x0}}H_1^{(2)}\left(k_{\rho_x}\rho_x\right)e^{-jk_x(x-x_0)}dk_x \quad . \tag{5.4}$$

For the space-wave current I^{space}, the E_z field component can be found through coordinate transformation of Equations (2.6) and (2.7) along with direct geometric relations to give

$$E_z^{space} = \frac{1}{j\omega\varepsilon}\frac{\partial}{\partial\rho_x}\frac{\partial}{\partial x}\left(\frac{1}{4\pi}\int_{x_2}^{x_1}\frac{-(z-z_i)}{\rho_x}\frac{-I^{space}(x_i)}{R}e^{-jkR}dx_i\right) . \tag{5.5}$$

After some simplification, this can be expressed as

$$E_z^{space} = (z-z_i)\frac{j\eta}{4\pi}\int_{x_2}^{x_1}\left(\frac{-k}{R^3}+\frac{3j}{R^4}+\frac{3}{kR^5}\right)(x-x_i)I^{space}(x_i)e^{-jkR}dx_i \quad . \tag{5.6}$$

For the vertical signal feed and grounding line currents I^{vert}, the E_z field component is formed by combining Equations (2.5) and (2.6) to become

$$E_z^{vert} = \frac{1}{j\omega\varepsilon}\frac{1}{4\pi}\left(\int_{z_2}^{z_1}\frac{\partial^2}{\partial z^2}\frac{-I^{vert}(z_i)}{R}e^{-jkR}dz_i + k^2\int_{z_2}^{z_1}\frac{-I^{vert}(z_i)}{R}e^{-jkR}dz_i\right) . \tag{5.7}$$

After some simplification, it can be expressed as

$$E_z^{vert} = \frac{-j\eta}{4\pi}\int_{z_2}^{z_1}\left[\frac{k}{R}+\left(\frac{-k}{R^3}+\frac{3j}{R^4}+\frac{3}{kR^5}\right)(z-z_0)^2+\left(\frac{-j}{R^2}+\frac{-1}{kR^3}\right)\right]I^{vert}(z_i)e^{-jkR}dz_i \quad . \tag{5.8}$$

The total E_z field component can be found by

$$E_z = \sum_{ABCN}E_z^{travel} + \sum_{ABCN}E_z^{space} + \sum_{\substack{sig\,\&\\ gnd}}E_z^{vert} \quad , \tag{5.9}$$

where $\sum_{ABCN}$ and $\sum_{\substack{sig\,\&\\ gnd}}$ denotes the summation of all the power lines on both directions from the utility pole and the vertical signal feed wires as well as the vertical grounding

lines, respectively. The integration in Equations (5.4), (5.6) , and (5.8) are performed numerically.

5.2 Transmitter System Only: SDI Formulation

As discussed in Section 2.3, the use of SDI allows the earth to have more general properties and its formulation is detailed in this section. Representing the earth as a semi-infinite region, it can be assigned a loss tangent (calculated from the conductivity and relative permittivity) to reflect, to some degree, the actual earth characteristics (modeling the earth as homogenous and isotropic). Figure 2.2 illustrates the concept for vertical and horizontal currents.

Using Equation (5.2) to represent the traveling-wave current, the E_z field component in the air region below the source based on Equation (2.8) would be

$$E_z^{travel} = \frac{1}{(2\pi)^2}\int_{-\infty}^{\infty}\int_{-\infty}^{\infty} \frac{1}{\omega\varepsilon_0} k_x \left(\frac{j}{k_x - k_{x0}} I_0^{travel}\right) I_i^{TM}\left(k_\rho, z, z_i\right) e^{-j\left(k_x[x-x_i]+k_y[y-y_i]\right)} dk_x dk_y \ , \quad (5.10)$$

where

$$I_i^{TM}\left(k_\rho, z, z_i\right) = \frac{-T_i^{TM}\left(k_\rho, z, z_i\right)}{Z_{in}^{TM}\left(k_\rho, z_i\right)}\left(\frac{1}{Z_0^{TM}\left(k_\rho\right)} + \frac{1}{Z_{in}^{TM}\left(k_\rho, z_i\right)}\right)^{-1} \ , \quad (5.11)$$

$$T_i^{TM}\left(k_\rho, z, z_i\right) = \frac{e^{jk_{z0}\left(k_\rho\right)\cdot z} - \Gamma^{TM}\left(k_\rho\right) e^{-jk_{z0}\left(k_\rho\right)\cdot z}}{e^{jk_{z0}\left(k_\rho\right)\cdot z_i} - \Gamma^{TM}\left(k_\rho\right) e^{-jk_{z0}\left(k_\rho\right)\cdot z_i}} \ , \quad (5.12)$$

$$\Gamma^{TM}\left(k_\rho\right) = \frac{Z_1^{TM}\left(k_\rho\right) - Z_0^{TM}\left(k_\rho\right)}{Z_1^{TM}\left(k_\rho\right) + Z_0^{TM}\left(k_\rho\right)} \ , \quad (5.13)$$

$$Z_{in}^{TM}\left(k_\rho, z_i\right) = Z_0^{TM}\left(k_\rho\right)\frac{Z_1^{TM}\left(k_\rho\right) + jZ_0^{TM}\left(k_\rho\right)\cdot\tan\left(k_{z0}\left(k_\rho\right)\cdot z_i\right)}{Z_0^{TM}\left(k_\rho\right) + jZ_1^{TM}\left(k_\rho\right)\cdot\tan\left(k_{z0}\left(k_\rho\right)\cdot z_i\right)} \ , \quad (5.14)$$

$$Z_0^{TM}\left(k_\rho\right)=\frac{k_{z0}\left(k_\rho\right)}{\omega\varepsilon_0}\ , \tag{5.15}$$

$$Z_1^{TM}\left(k_\rho\right)=\frac{k_{z1}\left(k_\rho\right)}{\omega\varepsilon_1}=\frac{k_{z1}\left(k_\rho\right)}{\omega\varepsilon_0\varepsilon_{r,earth}}\ , \tag{5.16}$$

$$k_{z0}\left(k_\rho\right)=\sqrt{k_0^2-k_\rho^2}\ , \tag{5.17}$$

$$k_{z1}\left(k_\rho\right)=\sqrt{k_1^2-k_\rho^2}\ , \tag{5.18}$$

$$k_1=k_0\sqrt{\varepsilon_{r,earth}}\ , \tag{5.19}$$

and

$$\varepsilon_{r,earth}=\varepsilon'_{r,earth}\left(1-j\tan\delta_{earth}\right)\ , \tag{5.20}$$

with k_ρ defined by Equation (2.9). After converting the spectral variables to cylindrical coordinates and simplifying, Equation (5.10) can be expressed as

$$E_z^{travel}=\frac{j\cdot I_0^{travel}}{\left(2\pi\right)^2\omega\varepsilon_0}\int_0^\infty k_\rho^2\ I_i^{TM}\left(k_\rho,z,z_i\right)\left[\int_0^{2\pi}\frac{\cos\left(\phi_{k_\rho}\right)}{\cos\left(\phi_{k_\rho}\right)-\frac{k_{x0}}{k_\rho}}e^{-jk_\rho\cos\left(\phi_{k_\rho}-\phi\right)}d\phi_{k_\rho}\right]dk_\rho\ , \tag{5.21}$$

where ϕ_{k_ρ} is the spectral angle defined as $\cos\left(\phi_{k_\rho}\right)=\frac{k_x}{k_\rho}$. Equation (5.21) minimizes the computation of the I_i^{TM} function compared to the rectangular spectral coordinate system of Equation (5.10), facilitating better utilization of computational resources.

The space-wave currents are modeled as a continuous distribution of infinitesimal dipoles with amplitude I^{space}. Thus, the E_z field component in the air region below the source for a given dipole can be found from Equation (2.8) as

$$E_{z,dip}^{space} = \frac{1}{(2\pi)^2}\int_{-\infty}^{\infty}\int_{-\infty}^{\infty} \frac{1}{\omega\varepsilon_0} k_x \, I^{space}(x) \, I_i^{TM}\left(k_\rho, z, z_i\right) e^{-j\left(k_x[x-x_i]+k_y[y-y_i]\right)} dk_x dk_y \ . \quad (5.22)$$

Converting the spectral variables to cylindrical coordinates and simplifying yields

$$E_{z,dip}^{space} = \frac{(x-x_i)}{\rho}\frac{I^{space}(x)}{2\pi\omega\varepsilon_0}\int_0^{\infty} J_1\left(k_\rho\rho\right) I_i^{TM}\left(k_\rho, z, z_i\right) k_\rho^2 dk_\rho \ , \quad (5.23)$$

where J_1 denotes the first-order Bessel function. The E_z field component in the air region below the source due to the space-wave current on a horizontal line, I^{space}, is then

$$E_z^{space} = \frac{1}{2\pi\omega\varepsilon_0}\int_{x_2}^{x_1} \frac{(x-x_i)}{\rho} I^{space}(x) \int_0^{\infty} J_1\left(k_\rho\rho\right) I_i^{TM}\left(k_\rho, z, z_i\right) k_\rho^2 dk_\rho dx_i \ . \quad (5.24)$$

For the vertical signal feed and grounding line currents I^{vert}, the E_z field component in the air region below the source can be obtained via Equation (2.10), where

$$I_v^{TM}\left(k_\rho, z, z_i\right) = \frac{T_i^{TM}\left(k_\rho, z, z_i\right)}{Z_0^{TM}\left(k_\rho\right) + Z_{in}^{TM}\left(k_\rho, z_i\right)} \ . \quad (5.25)$$

The functions $T_i^{TM}\left(k_\rho, z, z_i\right)$, $Z_0^{TM}\left(k_\rho\right)$, and $Z_{in}^{TM}\left(k_\rho, z_i\right)$ are defined by Equations (5.12) through (5.20).

Hence, the total E_z field component can then be found using Equation (5.9). The integration in Equations (5.21), (5.24), and (2.10), are performed numerically with the formulation to facilitate the computation of Equation (2.10) near the grounding line currents derived in Appendix C.

5.3 Transmitter and Receiver Systems

It is usually the intent for the transmitted signal to be received, and so there is a receiver on the system at some point. Hence, the model for transmitter and receiver systems (TX-RX) configuration is described in this section.

Typically, the BPL device hosts both transmit and receive circuits. While it may be possible for both circuits to be operating in tandem, superposition can be leveraged to explore the fields of each operating mode independently. Further, it is assumed that the BPL installation practice for the transmitter on the utility pole is the same as for the receiver on the pole. Thus, the TX-RX model shown in Figure 5.3 is used, where the feed lines from the power lines to the receive circuits are the same as that for the transmit circuit.

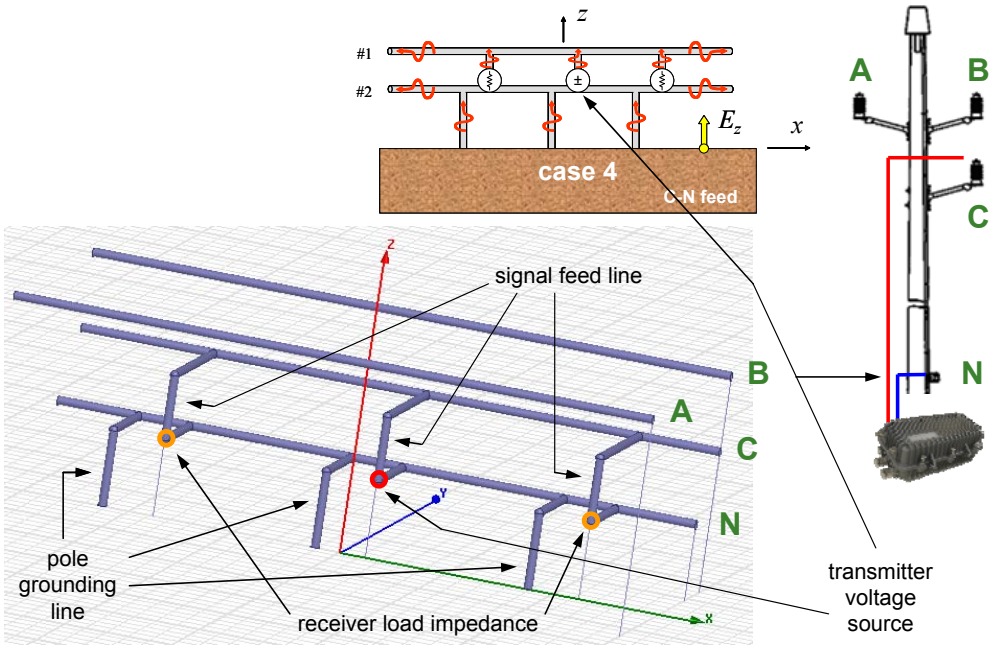

Figure 5.3 Side, end, and 3D perspective views of case 4 canonical model concept for TX-RX systems configuration.

5.4 Results and Observations

In this section, the assumptions from Section 3.4 continue to be applied along with the following:

- The power line endpoints for the TX-RX model are $35\lambda_0$ at 30 MHz (≈ 350 meters) away from the central utility pole where the transmitter is located.
- The utility poles hosting the receivers are located $20\lambda_0$ at 30 MHz (≈ 200 meters) away from the central utility pole on both sides.
- "(σ, ε)" refers to the selected values of $\sigma = 0.1$ S/m and $\varepsilon'_{r,earth} = 8$.
- "large σ" refers to the selected value of $\sigma = 4 \cdot 10^7$ S/m.
- The outer boundary far-field criterion [28] is based on dimensions of the single cell TX-only model, where the largest dimension would be the power lines (≈ 400 meters from $x < 0$ endpoint to $x > 0$ endpoint). This leads the threshold radial distance to be approximately 3.2 and 32 km, with selected radial distances of 10 and 100 km, for 3 and 30 MHz, respectively.

Unless there are indications to the contrary, these assumptions are expected to provide sufficiently general conditions from which observations can be made.

Results are first shown assuming a TX-only (transmitting BPL source only and no receivers) structure. This is the case shown in Figure 3.5. Later, results are shown for the TX-RX structure of Figure 5.3, which has receivers.

Figure 5.4 show the magnitude of the vertical field E_z along the surface of the earth ($z = 0$) on the $y > 0$ side of the FCC lines at 3 MHz decomposed into its constituent parts from the various components of the current on the system. Including the total E_z field ("sum"), the figure shows the following E_z fields:

- Vertical currents ("verticals") from the vertical connector wire and the vertical ground wire.
- Horizontal currents ("horizontals") from the horizontal wires that connect the vertical signal feed line and grounding wires to the power lines.
- Traveling-wave currents ("traveling") on the power lines (A, B, C, N).
- Space-wave currents ("space") on the power lines (A, B, C, N).

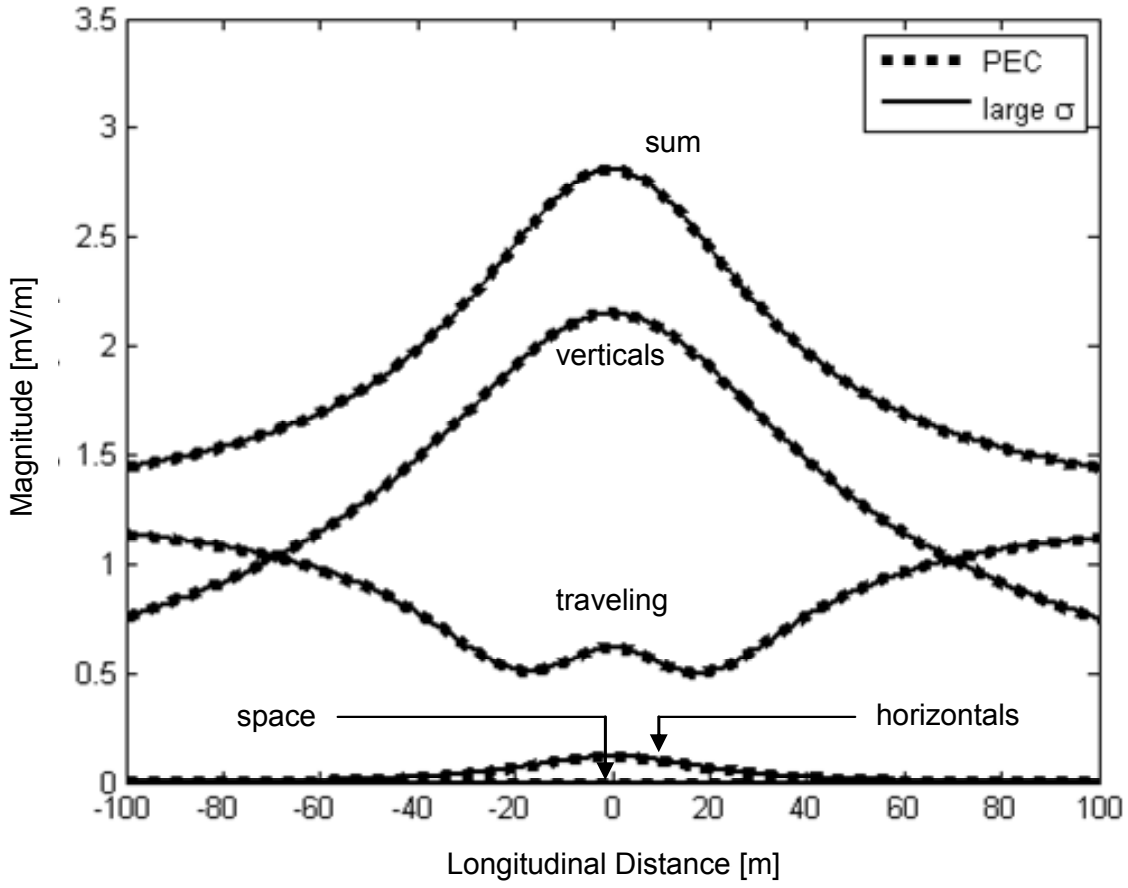

Figure 5.4 Vertical electric field of the TX-only configuration at 3 MHz along the earth ($z = 0$) on the $y > 0$ side of the FCC lines comparing between PEC and large σ earth models.

A comparison is made between results obtained using a PEC earth model (which uses image theory) and an earth model that uses a finite but very large conductivity. The latter model requires the SDI method, though the results should be in agreement with those of the PEC model due to the large value assumed for the conductivity. The good agreement seen in Figure 5.4 is thus a validation of the models.

Analogous to Figure 5.4, Figure 5.5 shows a comparison between the PEC earth model and a realistic earth model using a finite conductivity, as discussed in Chapter 2 (σ and ε_r' for the earth region are 0.1 S/m and 8, respectively). It is seen that at this low frequency, the earth has negligible effects on the fields. Near the utility pole (i.e., for smaller longitudinal distances along x), the field is dominated by the field from the vertical wires (i.e., the vertical connector wire and the vertical ground wire). However, farther from the pole (i.e., larger distances x), the field of the horizontal wires (A, B, C, N) becomes dominant. This is expected, since the field form the vertical wires is radiation type of field, while the field from the horizontal wires consists of not only a radiation type of field but a transmission-line type of field as well, which does not decay with distance.

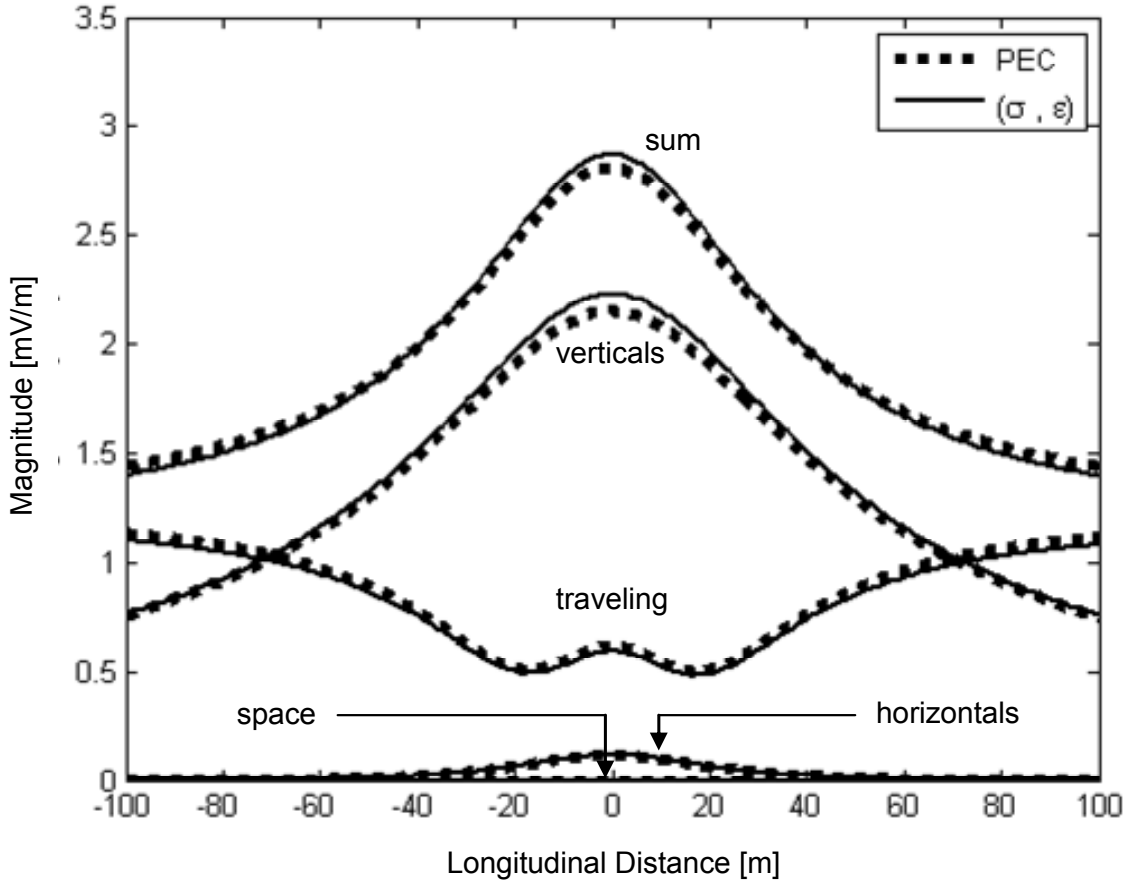

Figure 5.5 Same as Figure 5.4, except comparing with finite σ earth model.

Figure 5.6 shows the same set of results as in Figure 5.4 except that the frequency is at 30 MHz. The field from the space-wave current is noticeably stronger, as is the field from the horizontal connector wires. This is consistent with the fact that the amplitude of the space wave is expected to increase in frequency, as well as the fact that a horizontal current will radiate more as the electrical distance above a conducting ground increases.

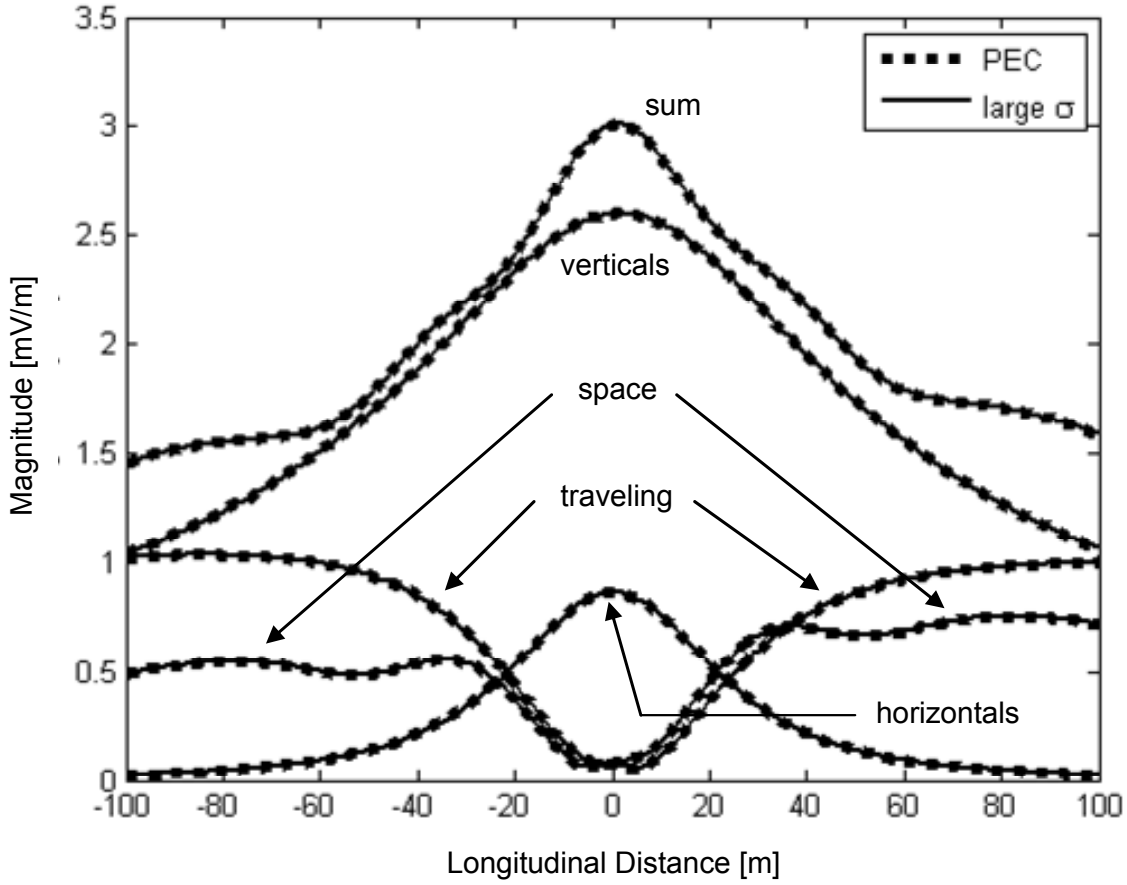

Figure 5.6 Same as Figure 5.4, except at 30 MHz.

Figure 5.7 shows a comparison between results for a PEC earth and a realistic earth at 30 MHz. In order to avoid overcrowding the figure, results are shown only for the total field and the fields due to the vertical currents and the horizontal currents. At 30 MHz there is a noticeable affect due to the realistic earth, although difference in profile is still not dramatic. This is perhaps expected, since the loss tangent of the realistic earth at this frequency is still fairly high, around 7.5.

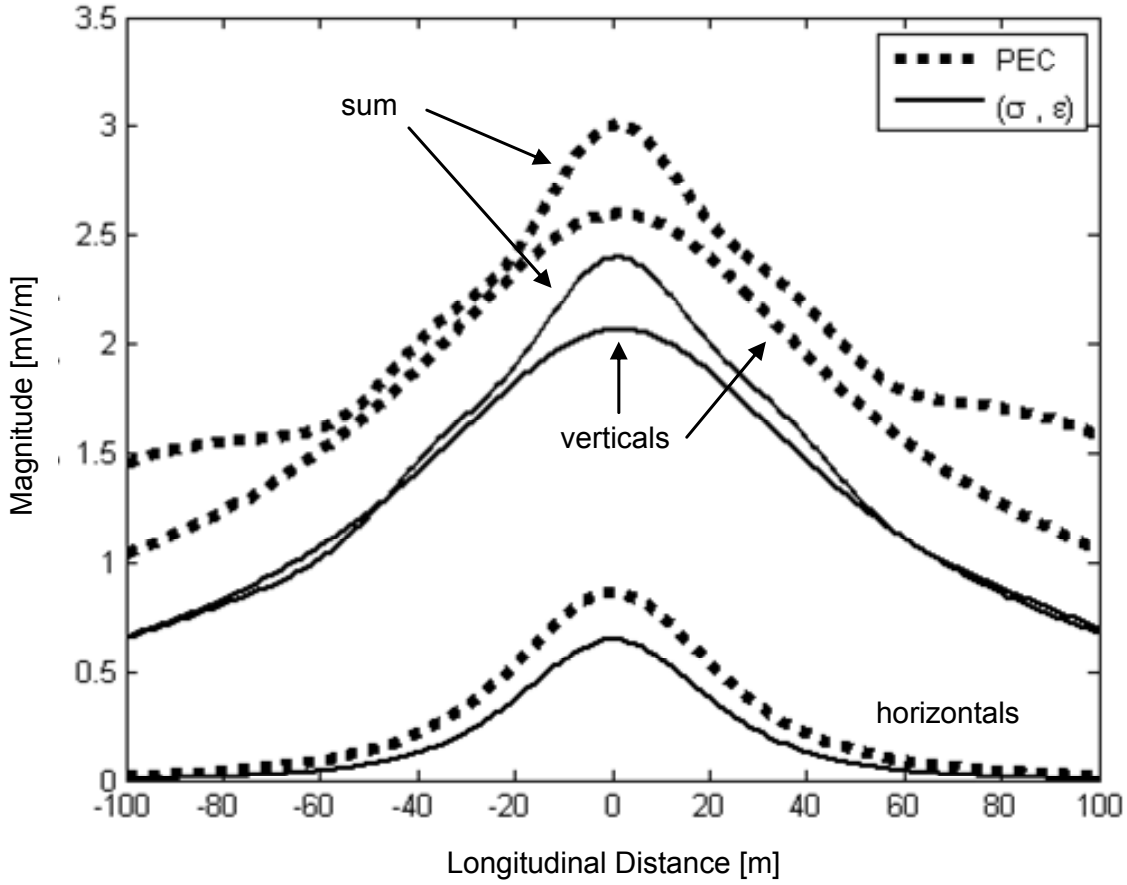

Figure 5.7 Same as Figure 5.5, except at 30 MHz without the fields of the space-wave currents and traveling-wave currents.

In Figures 5.8 and 5.9, the total E_z field is once again shown, comparing with the field of the traveling-wave current in Figure 5.8 and the space-wave current in Figure 5.9. The finite conductivity of the realistic earth has a pronounced effect of the fields of the space-wave currents and the traveling-wave currents when the longitudinal distance (i.e., the distance x from the BPL source) gets large. The profile differs from the effect of the finite conductivity on the fields from the vertical wires, which is much less dramatic.

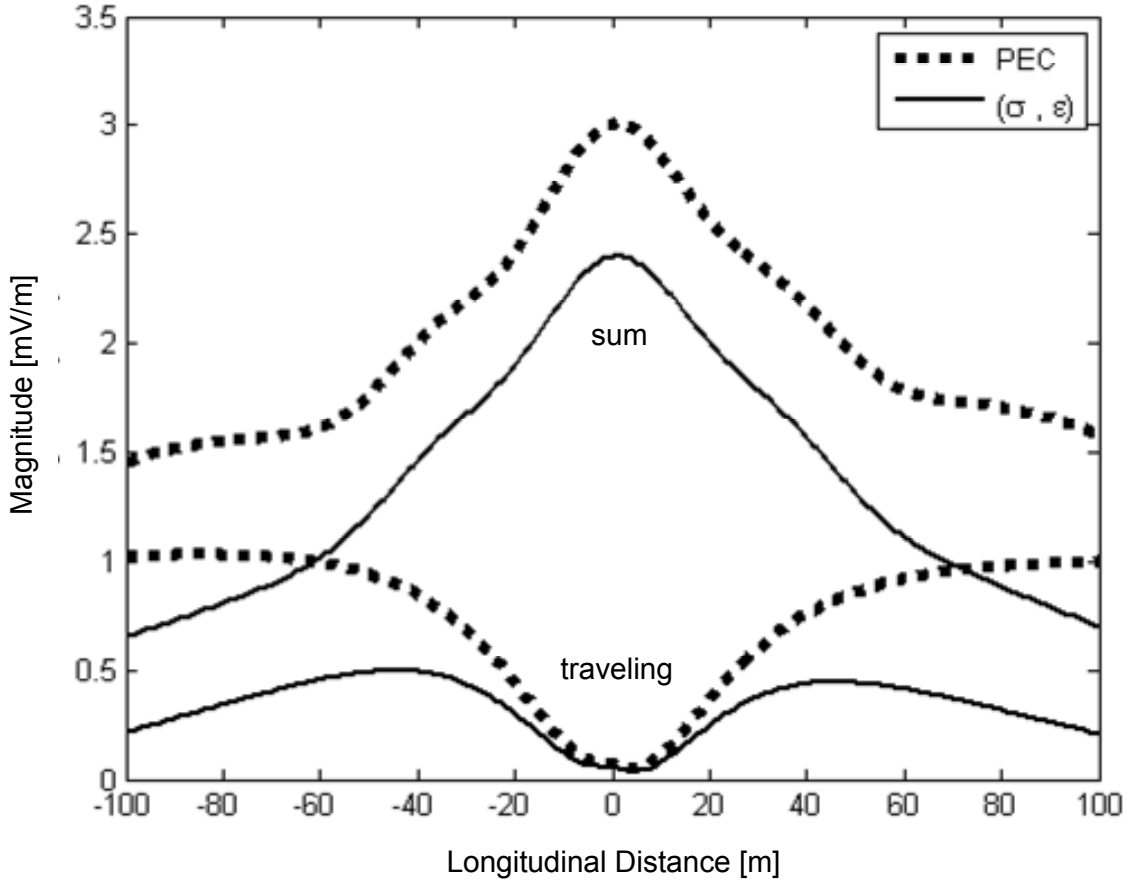

Figure 5.8 Same as Figure 5.7, except only the total vertical field is shown along with the field of the traveling-wave currents.

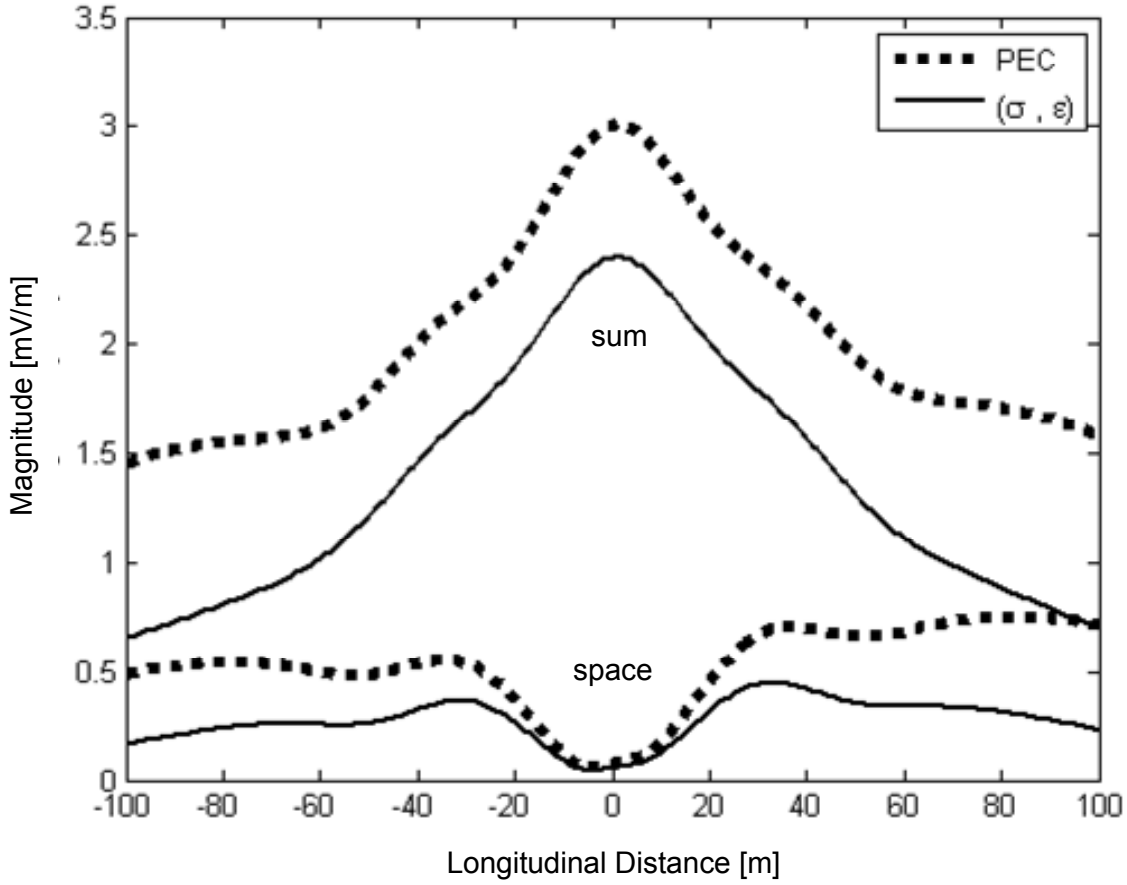

Figure 5.9 Same as Figure 5.8, except for the field of the space-wave currents.

Figures 5.10 through 5.12 compare the currents from moment method 2 between PEC and finite-conductive earth models. Figure 5.10 shows the 3 and 30 MHz currents along the vertical signal feed line and grounding wire. Figure 5.11 illustrate the power line currents at 3 MHz while Figure 5.12 pertains to 30 MHz. Note the similarity in profile of vertical currents between PEC and finite conductive earth models, with the most apparent earth effect being the difference in magnitude of the 3 MHz grounding wire current. As can be seen, the likeness between earth models also persists on the power line currents with exception to the neutral wire at 30 MHz. Since the noticeable

difference in power line current only exists along the neutral wire that has a less intense current than wire C and monotonically decreases in intensity, this indicates the presence of radiation. Thus, the total current along the neutral wire can be viewed as possessing two space-wave currents, one corresponding to the air region and the other to the semi-infinite region representing the finite conductive earth.

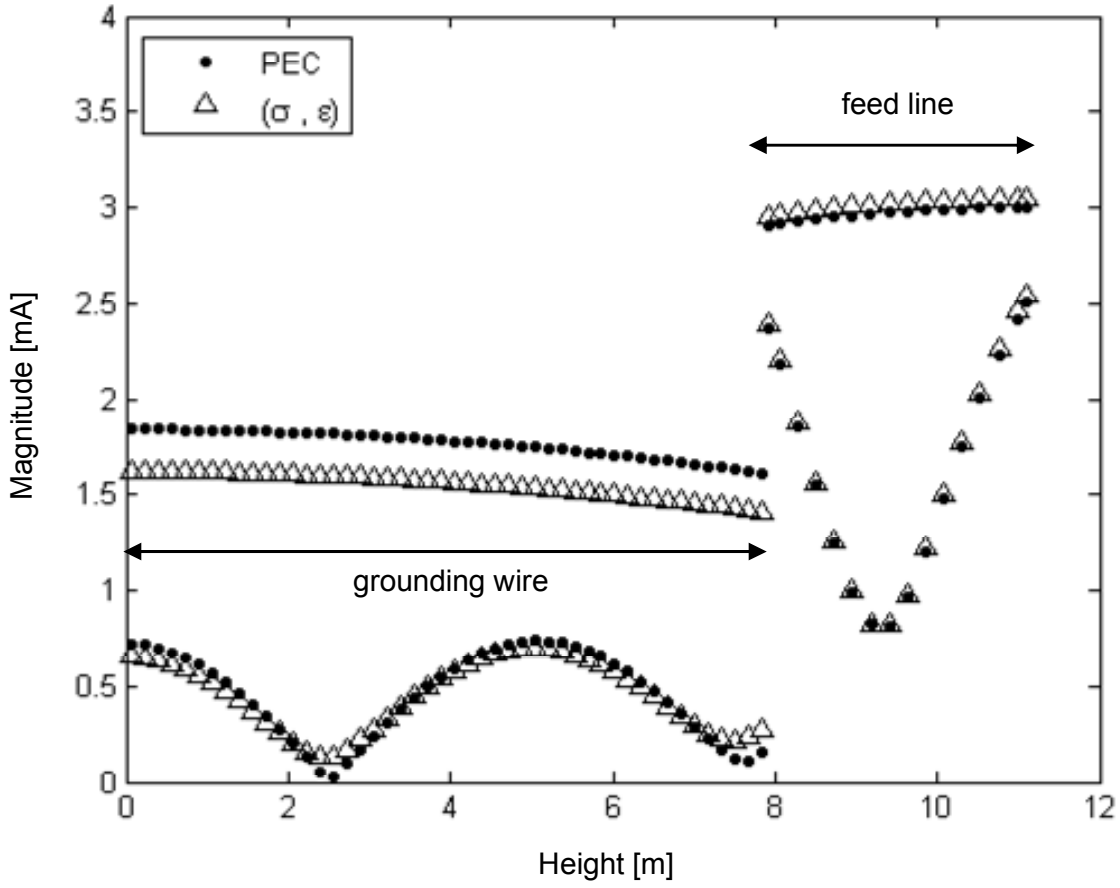

Figure 5.10 Currents along vertical signal feed line and grounding wire from moment method 2 comparing between PEC and finite σ earth models at 3 and 30 MHz.

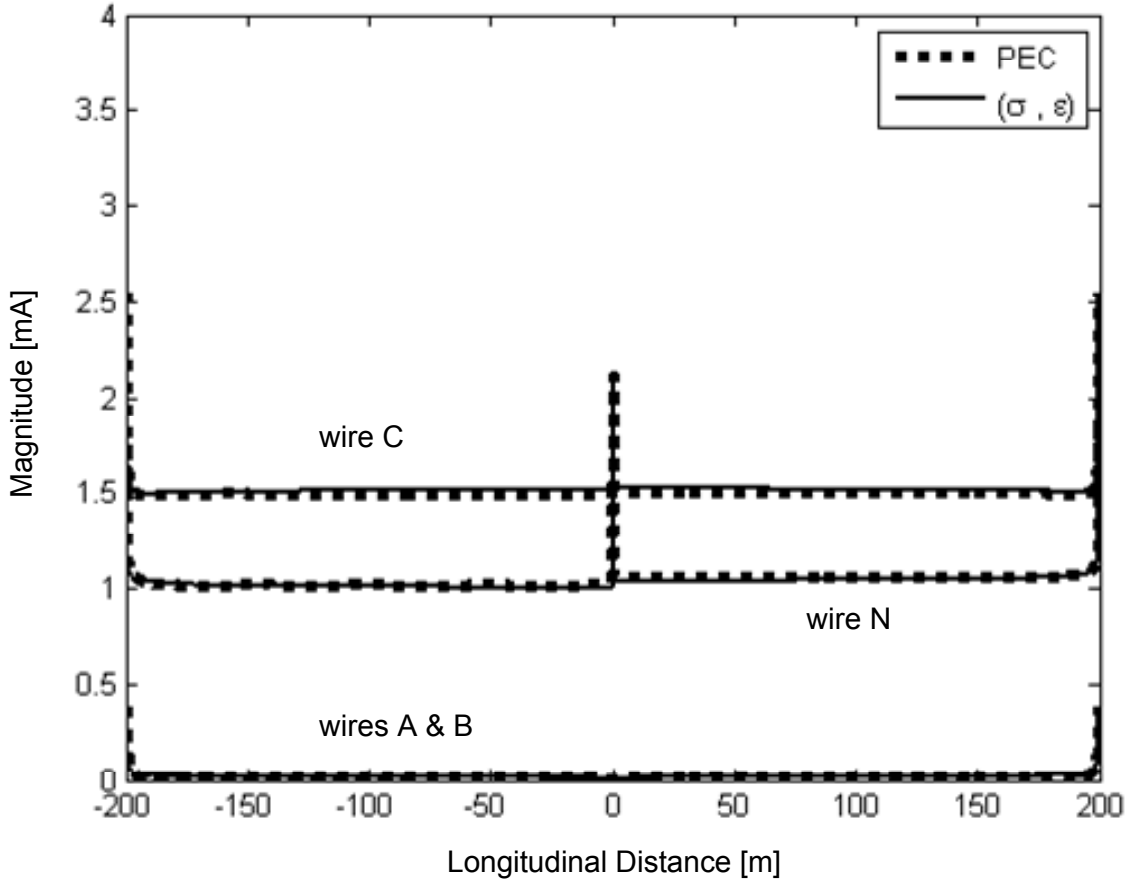

Figure 5.11 Same as Figure 5.10, except for the power line currents at 3 MHz.

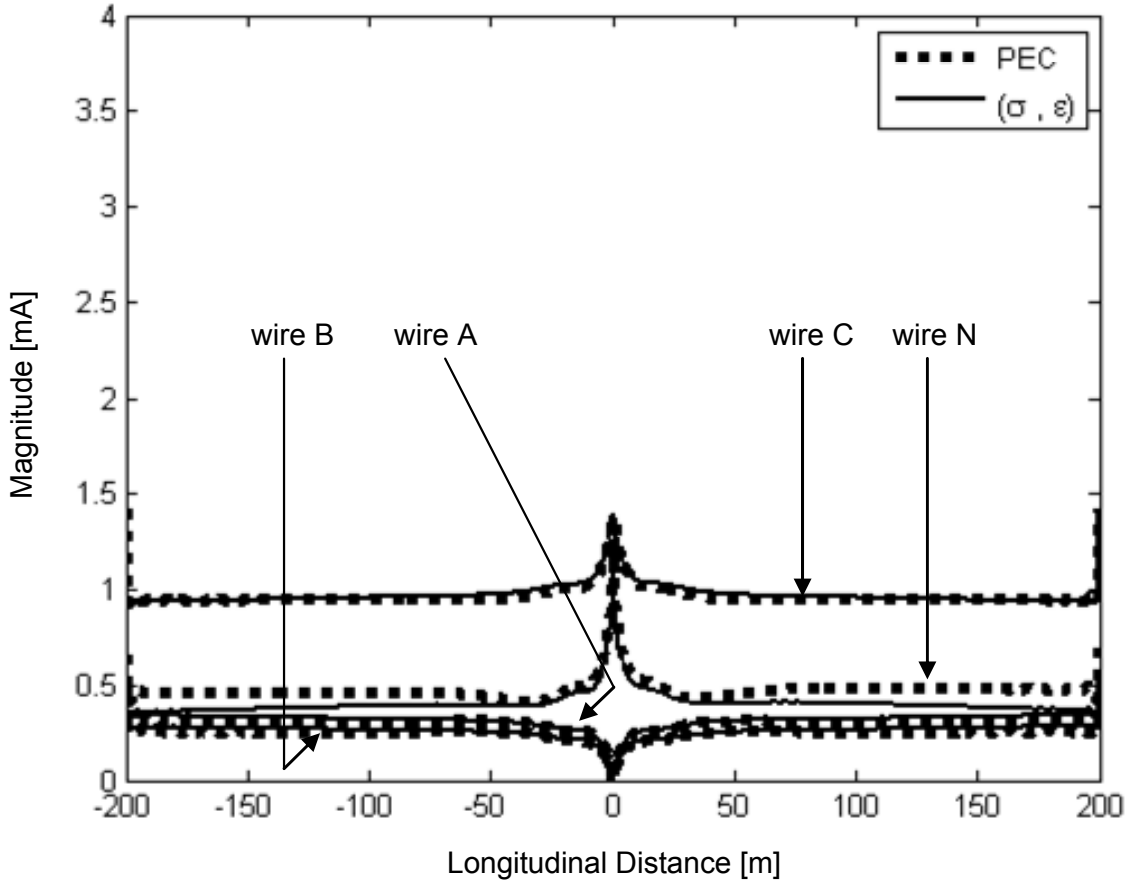

Figure 5.12 Same as Figure 5.11, except at 30 MHz.

Table 5.1 summarizes the various properties for the case 4 TX-only configuration at 3 and 30 MHz. Included in the table is the current at the BPL source (which is needed to calculate the power provided by the 1V source), the power provided by the 1V source, the peak electric field along earth at the FCC lines (parallel to and 30 meters horizontally away from the nearest power lines). Also included in the last column of the table is the BPL source power that would be necessary to marginally meet the FCC regulation, i.e., produce a maximum field level of 30 μV/m along the FCC line. These values were obtained from a simple scaling of the field levels obtained from the 1V source, using the

source power information of the 1V source. It is seen that the power of the source must be restricted to less than 138 nW at 3 MHz, and less than 64 nW at 30 MHz, based on the data-fitted method. Results based on using moment method 2 were a bit different, but not dramatic.

Table 5.1 TX-only device terminal properties from moment method 2 and the data-fitted model at 3 and 30 MHz.

		mtd	current [mA]	power [mW]	peak E-field [mV/m]	power [nW] (for FCC)
3 MHz	PEC	fit	2.54 – j 1.44	1.27	2.81	144
		2	2.58 – j 1.34	1.29	2.89	139
	finite σ	fit	2.54 – j 1.44	1.27	2.87	138
		2	2.69 – j 1.23	1.34	2.78	157
30 MHz	PEC	fit	1.29 + j 1.95	0.647	3.01	64.3
		2	1.47 + j 1.85	0.735	3.36	58.5
	finite σ	fit	1.29 + j 1.95	0.647	2.40	101
		2	1.47 + j 1.89	0.734	2.84	82.2

Figures 5.13 and 5.14 show surface plots of the vertical field level for case 4 at 3 MHz and 30 MHz, respectively, over a PEC earth, an earth with a large conductivity (provided again for validation), and a finite-conductive earth. Note the similarity in the region near the utility pole between the PEC scenario of Figures 5.13 and 5.14 to their respective counterparts in Figures 3.32 and 3.33, which does not have the passive conductor wires A and B. This further supports the effects of the passive wires first mentioned with Figures 4.3 and 4.4. It is seen in Figures 5.13 and 5.14 that the field level is higher at 30 MHz than at 3 MHz as expected, and that the finite-conductive earth lowers the field level somewhat when compared with the PEC earth.

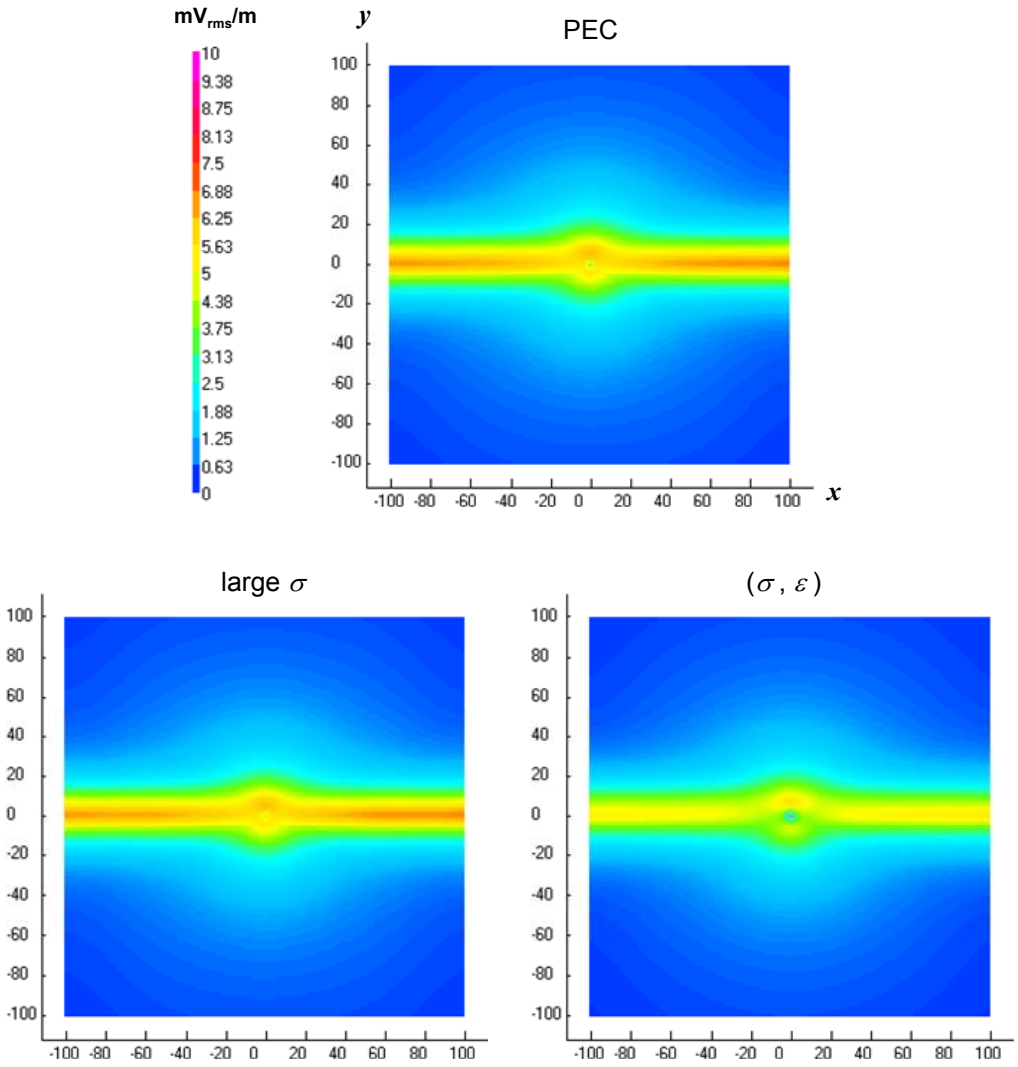

Figure 5.13 Surface plots from moment method 2 for the TX-only BPL cell comparing the total electric field along earth ($z = 0$) between various earth models at 3 MHz.

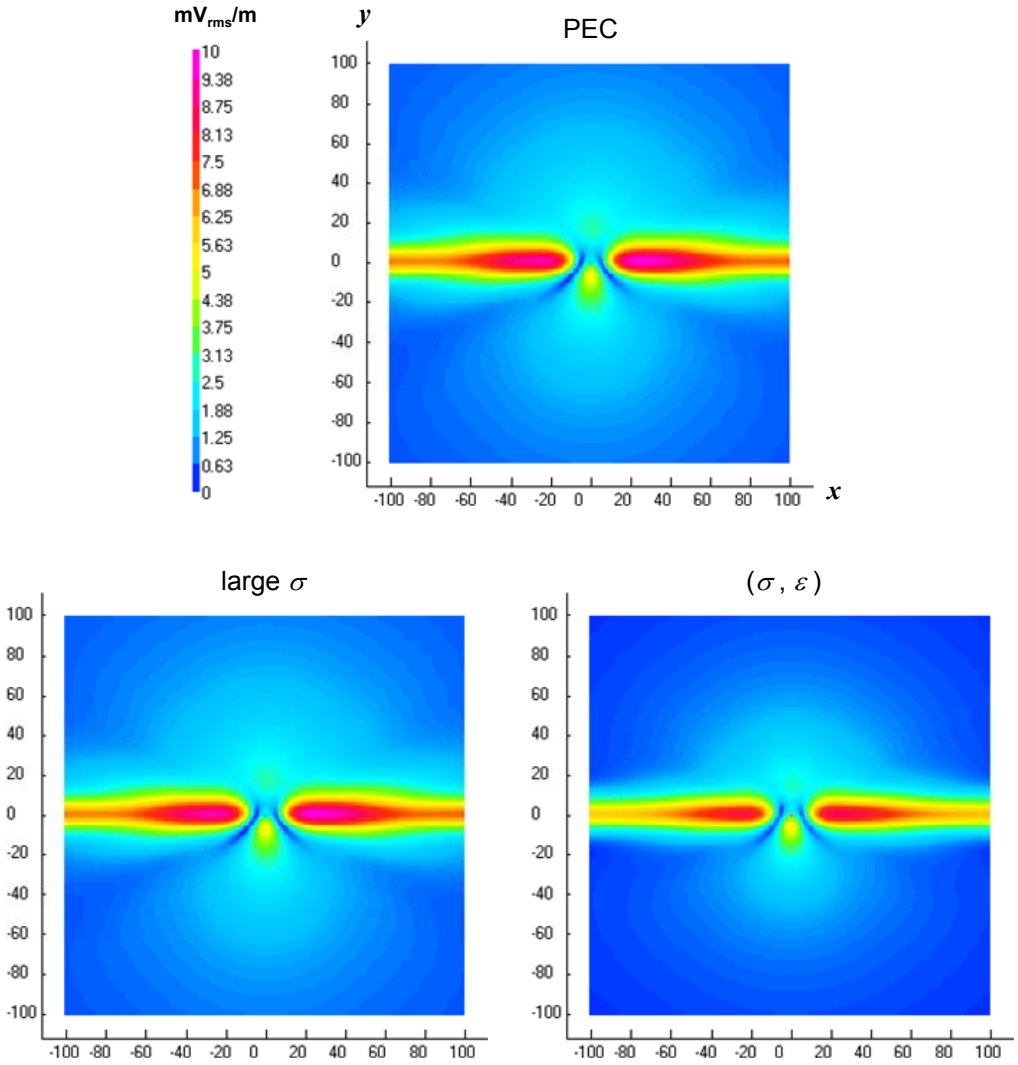

Figure 5.14 Same as Figure 5.13, except at 30 MHz.

Figures 5.15 and 5.16 show 3 MHz far-field polar plots of the field emission at a large distance of 10 km from the origin in spherical coordinates. This is essentially examining the antenna properties of the TX-only BPL cell, looking at the far-field radiation characteristics. The "E-plane" pattern (the *xz* plane) shows a multi-lobed pattern, as expected, since the horizontal lines are essentially acting as traveling-wave antennas in this plane. In the "H-plane" (the *yz* plane) there is no such multi-lobing. This

is expected from antenna theory, since the array factor for a long horizontal wire (giving the far-field pattern relative to a single horizontal electric dipole) does not have an angular variation in the H-plane. The strong resemblance to a vertical dipole is apparent in the H-plane, illustrating the extent of influence by the currents along the vertical feed line and grounding wire. Also noticeable is the fact that the finite-conductive earth significantly modifies the far-field pattern near the "horizon" (the surface of the earth) but has little effect at other angles. This is consistent with the theory of radiation from sources in layered media, which predicts that along an interface the field must decay with distance as $\frac{1}{r^2}$ instead of the usual $\frac{1}{r}$.

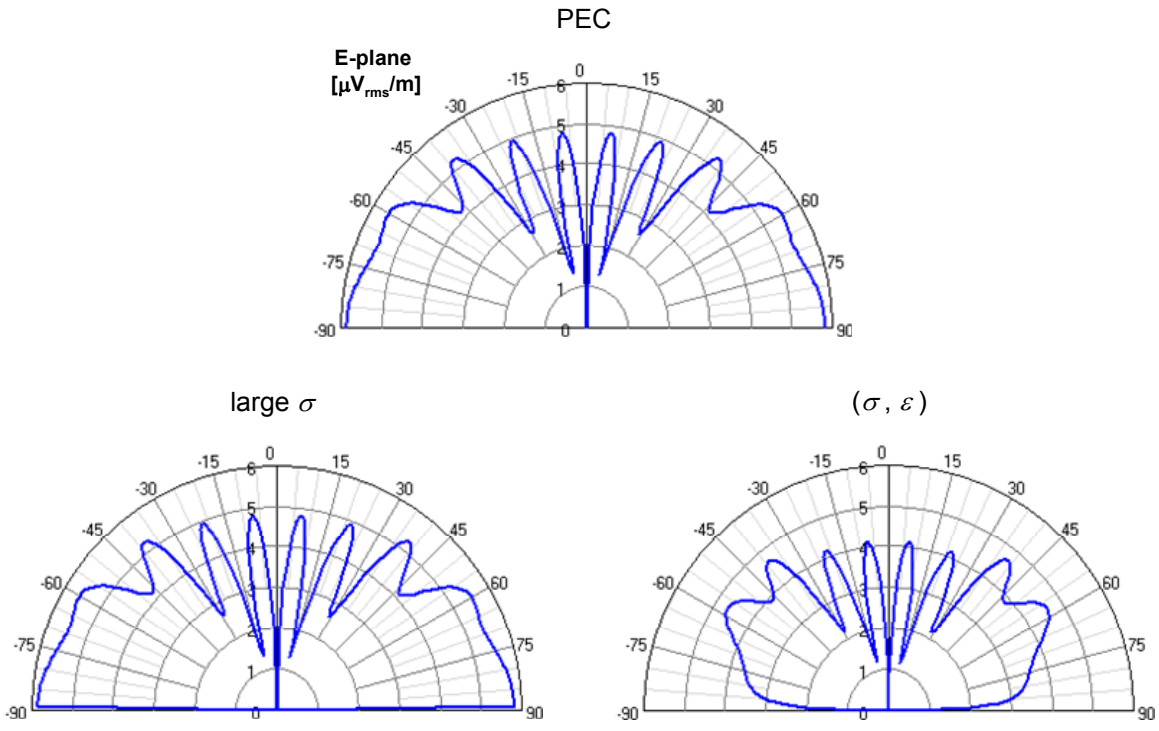

Figure 5.15 Polar plots from moment method 2 of the far-field pattern for the TX-only BPL cell comparing electric fields between various earth models with a radial distance of 10 km for $\phi = 0^\circ$ at 3 MHz.

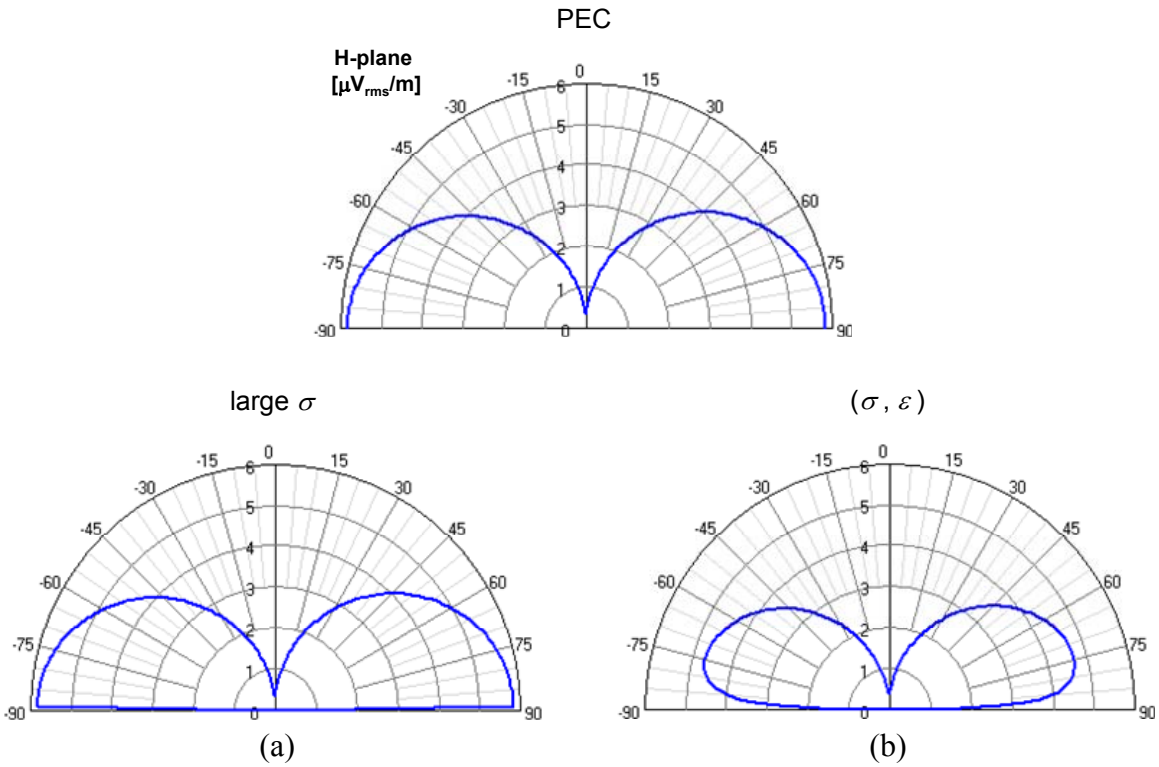

Figure 5.16 Same as Figure 5.15, except being $\phi = 90^{\circ}$.

Figures 5.17 and 5.18 show 30 MHz far-field patterns at a large distance of 100 km from the origin in spherical coordinates. Note the difference in scale between the figures. This indicates a greater influence of the power line currents when compared with the vertical feed line and grounding wire at 30 MHz. At this higher frequency, the E-plane patterns have become more endfire directed and illustrate the BPL cell to be an effective antenna system since the scale between Figures 5.17 and 5.15 is the same while being 10 times the distance and at about half the input power. The H-plane patterns show more skewing, which is likely due to the asymmetry in the feeding system with respect to the *y* direction. Similar to the 3 MHz scenario, the finite-conductive earth significantly modifies the pattern near the horizon but has little effect at other angles.

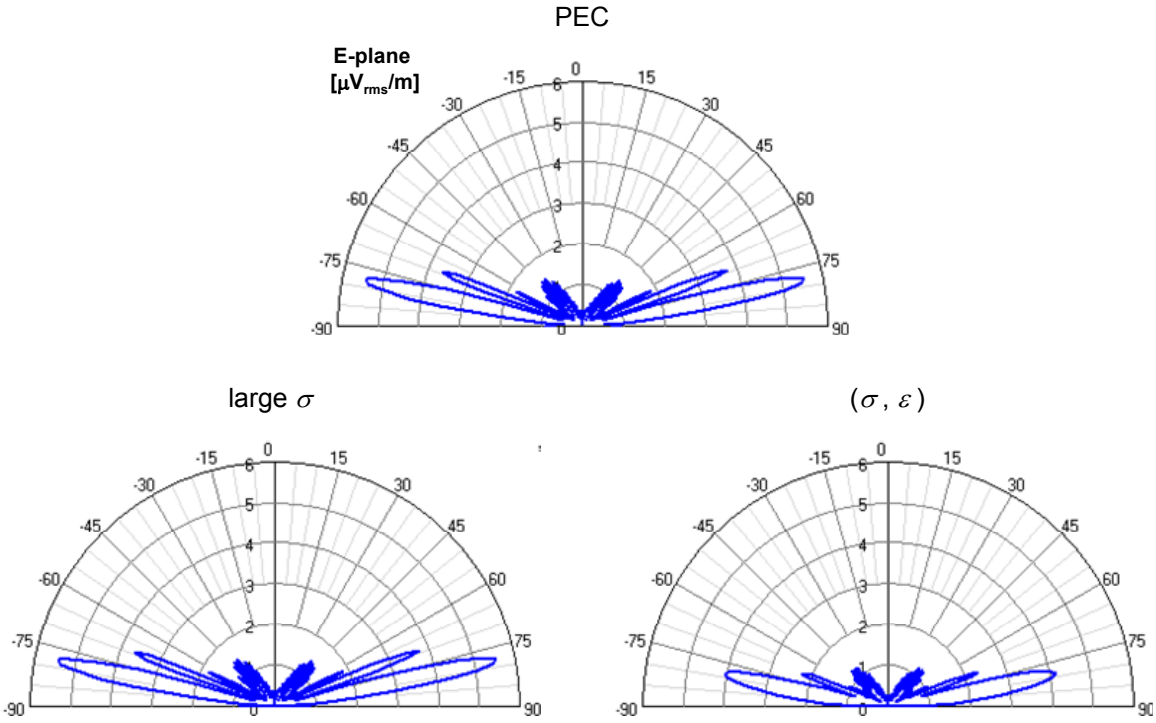

Figure 5.17 Same as Figure 5.15, except with a radial distance of 100 km at 30 MHz.

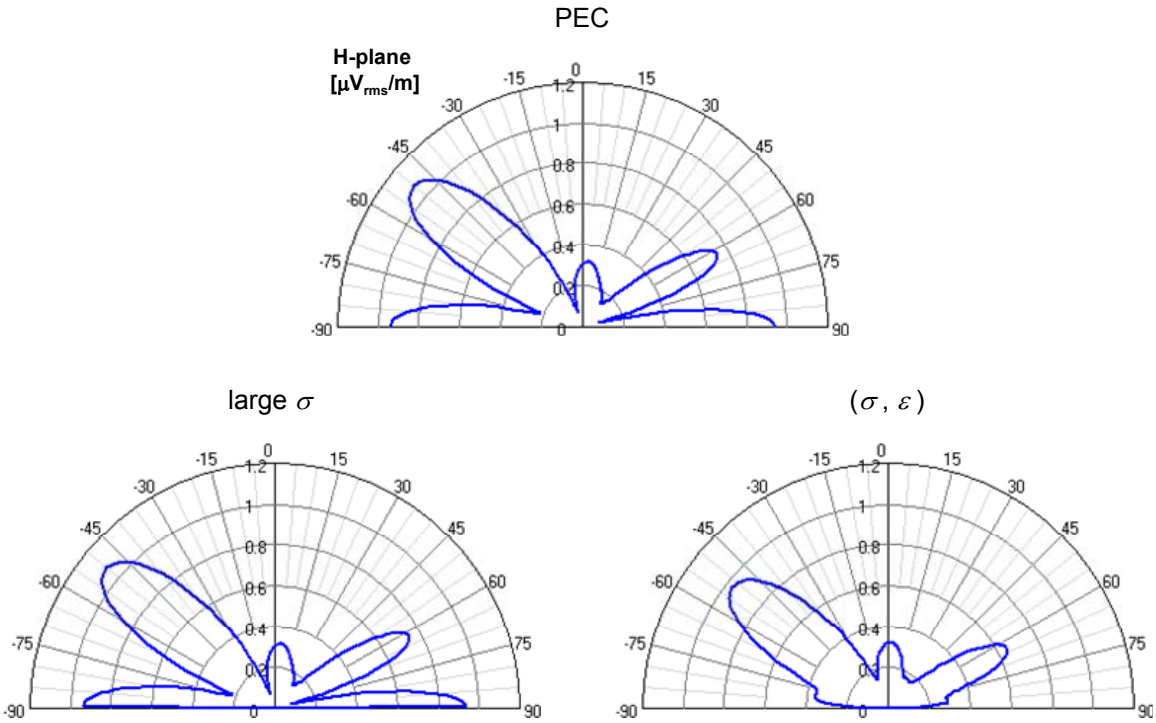

Figure 5.18 Same as Figure 5.17, except being $\phi = 90^{\circ}$.

Figures 5.19 and 5.20 show far-field azimuth pattern of a TX-only BPL cell from moment method 2 at the angle of the main lobe when the finite-conductive earth model is applied. Figure 5.19 compares the 3 MHz pattern between earth models with a large distance of 10 km from the origin at the angle $\theta = 74^{\circ}$ (angle of the main lobe) in spherical coordinates. Analogously, Figure 5.20 is for the 30 MHz earth model comparison at 100 km with $\theta = 79^{\circ}$ as the angle of the main lobe. Again, the pattern at the 30 MHz is quite evident to be endfire directed while only somewhat directional at 3 MHz. When Figure 5.20 is considered along with Figure 5.17, it is apparent that the BPL cell at 30 MHz produces a bi-directional pencil beam. Though there are some differences in magnitude, note that the effect on the pattern profile by the finite-conductive earth is not dramatic.

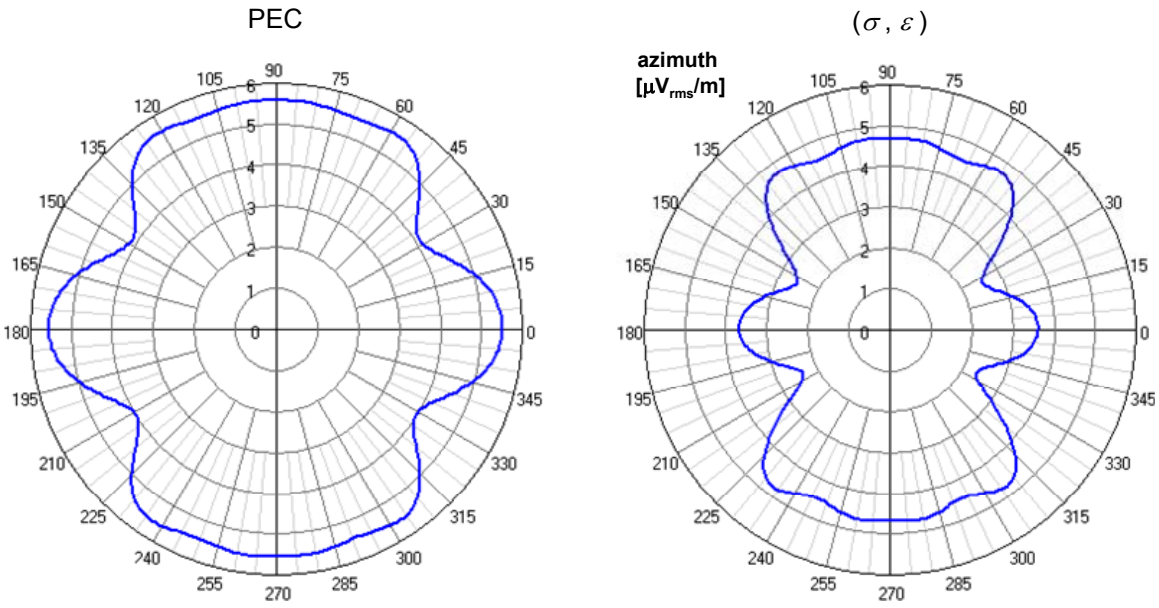

Figure 5.19 Polar plots from moment method 2 of the far-field pattern for the TX-only BPL cell comparing electric fields between PEC and finite σ earth models with a radial distance of 10 km for $\theta = 74^{\circ}$ at 3 MHz.

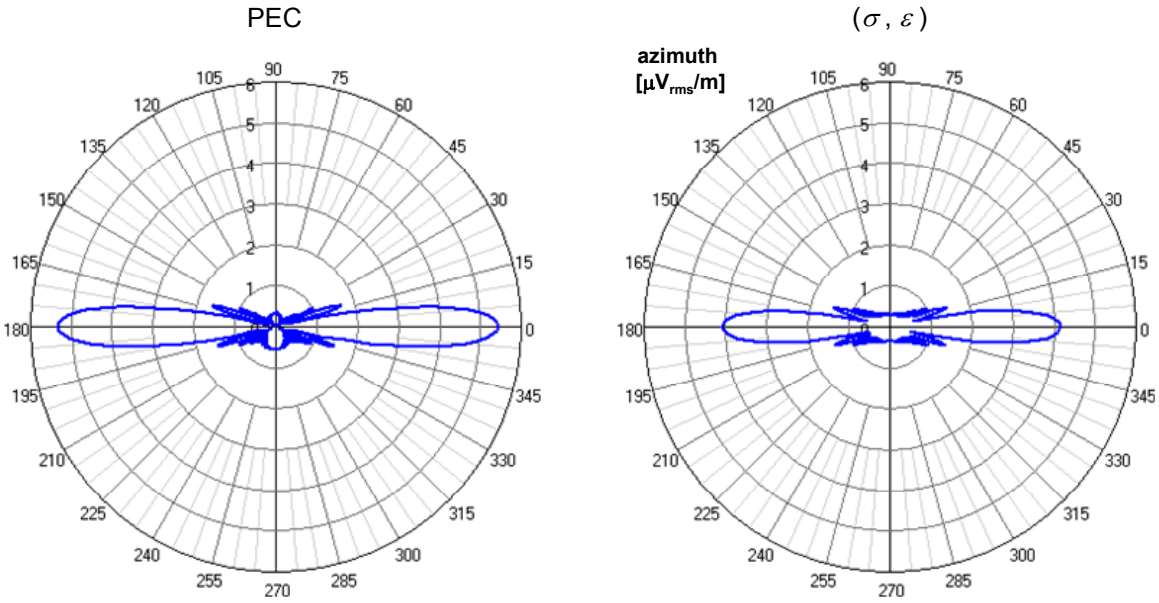

Figure 5.20 Same as Figure 5.19, except with a radial distance of 100 km for $\theta = 79^{\circ}$ at 30 MHz.

Figures 5.21 and 5.22 show results for case 4 with the presence of receivers illustrated in Figure 5.3. Figure 5.21 are for the vertical currents (i.e., the currents on the vertical connectors and the current on the ground wire) at 3 MHz while Figure 5.22 is for 30 MHz. Note the likeness in profile between the currents at $x = 0$ (the utility pole) to the corresponding TX-only plots of Figures 4.3, with magnitudes that greatly differ at 3 MHz and with a closer degree of similarity at 30 MHz. These attributes suggest that the TX-RX configuration can be viewed as a TX-only cell with a cascade connection to a RX-only cell on both ends, furthering the benefits of the single cell approach. The profile of the currents at the $x = \pm 200$ meters utility pole illustrates the effect due to the presence of a source along the feed line as oppose to a load impedance. As can be seen, the profiles of the grounding wire currents among the three utility poles are similar since none have a source.

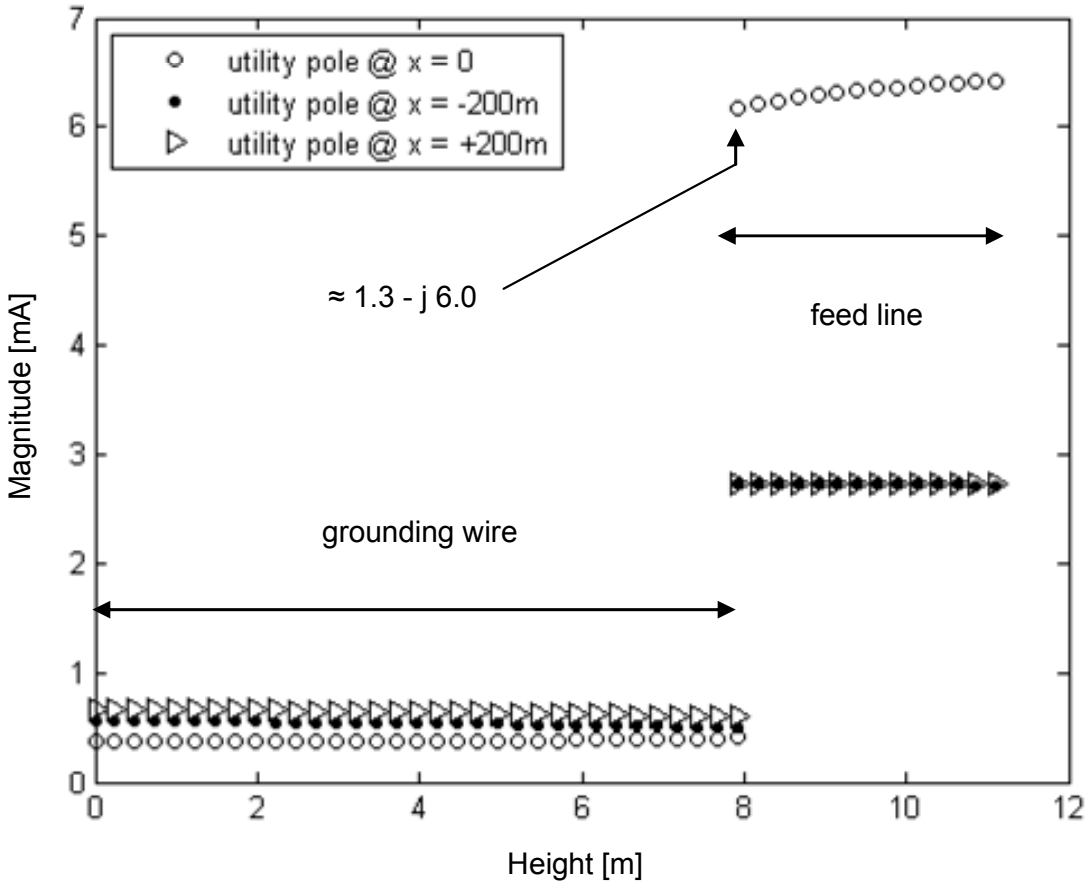

Figure 5.21 Vertical currents of TX-RX configuration at 3 MHz from moment method 1 for a PEC earth.

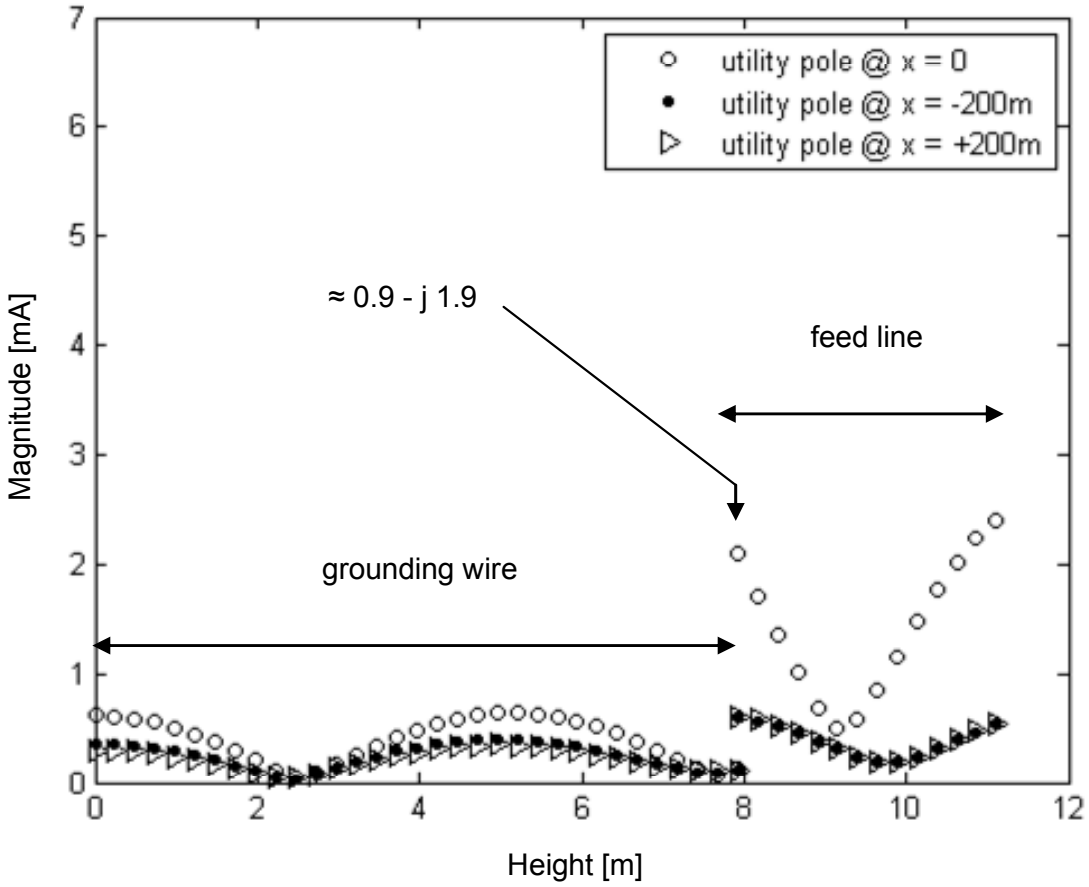

Figure 5.22 Same as figure 5.16, except at 30 MHz.

Figures 5.23 through 5.26 shows the currents on the horizontal lines (wires A, B, C, N) for case 4 with the presence of receivers. The main effect seen is the current on the horizontal wires, exhibiting a significant standing-wave pattern between receivers, in spite of the use of voltage sources at the end of the lines to minimize reflections. This is due to reflected currents being set up on the lines by the receiver system as is apparent at 3 MHz in Figure 5.23 and somewhat illustrated in Figure 5.24 for 30 MHz. The expanded view of Figure 5.24 in Figures 5.25 and 5.26 better depicts the presence of 30 MHz standing waves. When compared with the TX-only currents in Figures 4.7 and 4.8,

it can be seen that the forward propagating current beyond the receivers is reduced as a consequence of the partial reflection of the transmitter's forward propagating current.

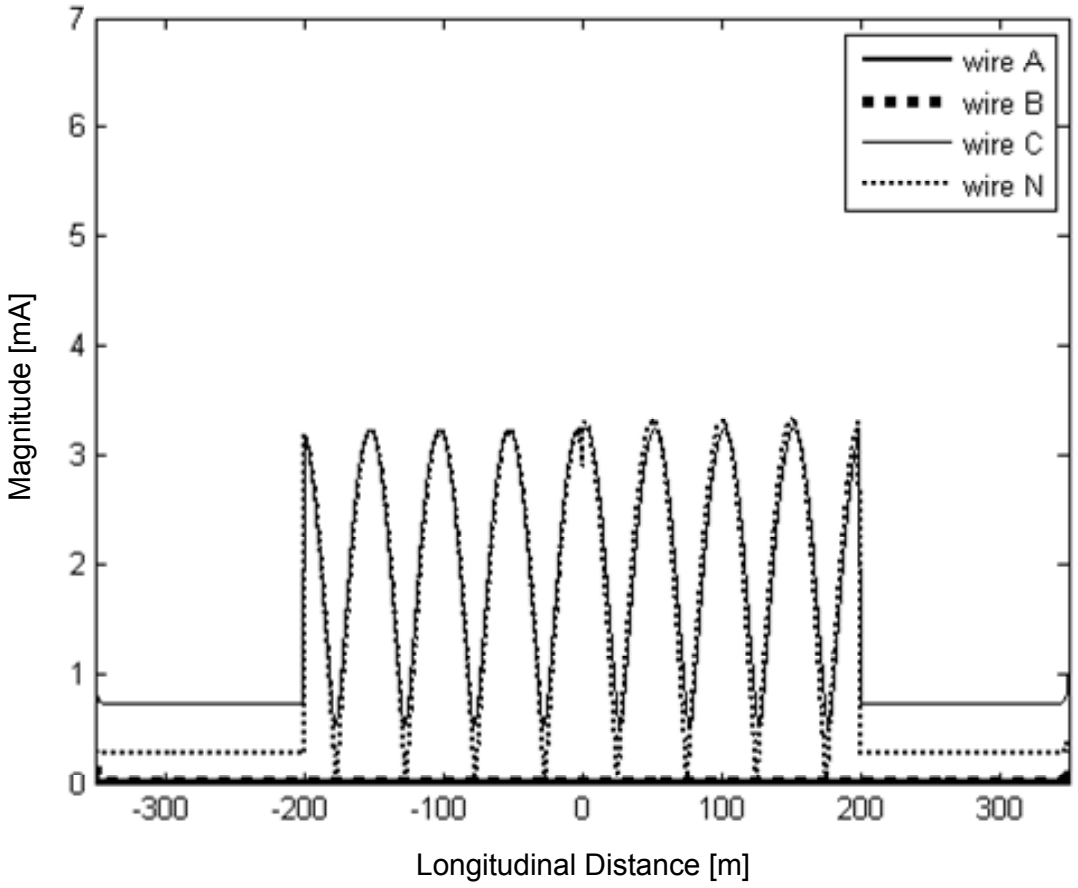

Figure 5.23 Power line currents of TX-RX configuration at 3 MHz for a PEC earth.

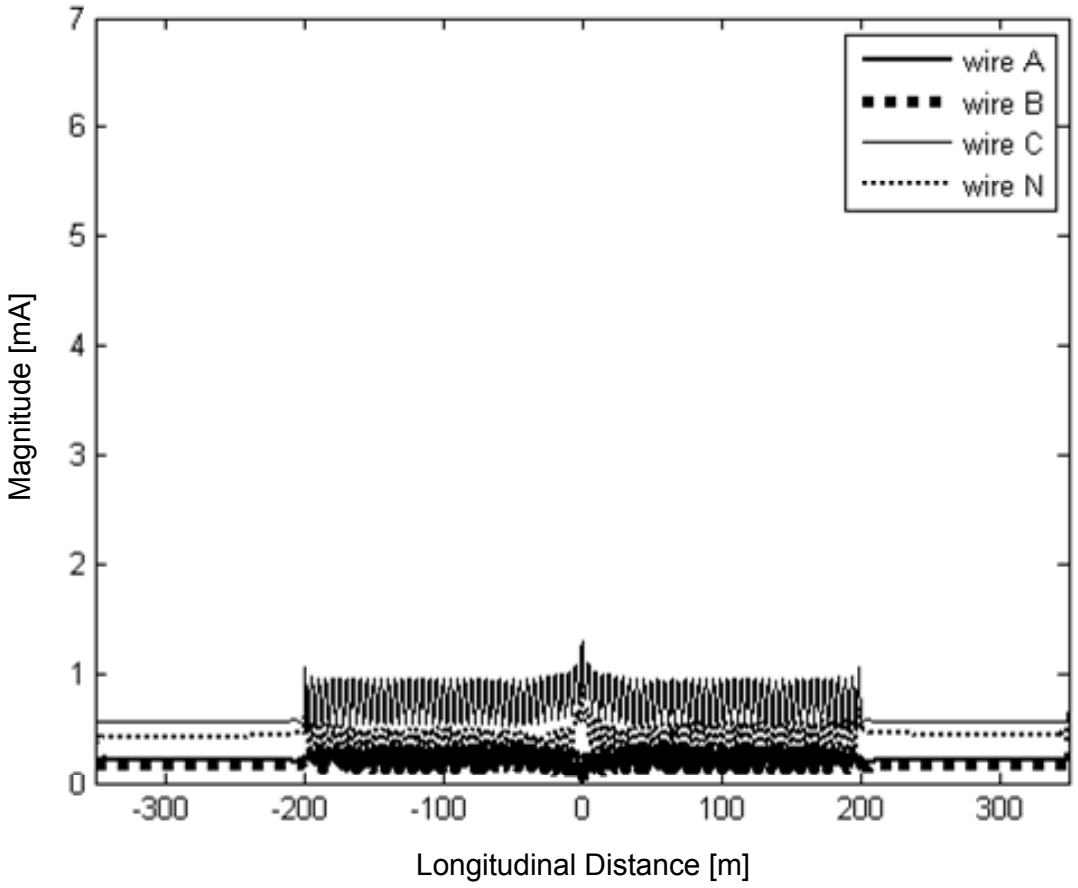

Figure 5.24 Same as Figure 5.23, except at 30 MHz.

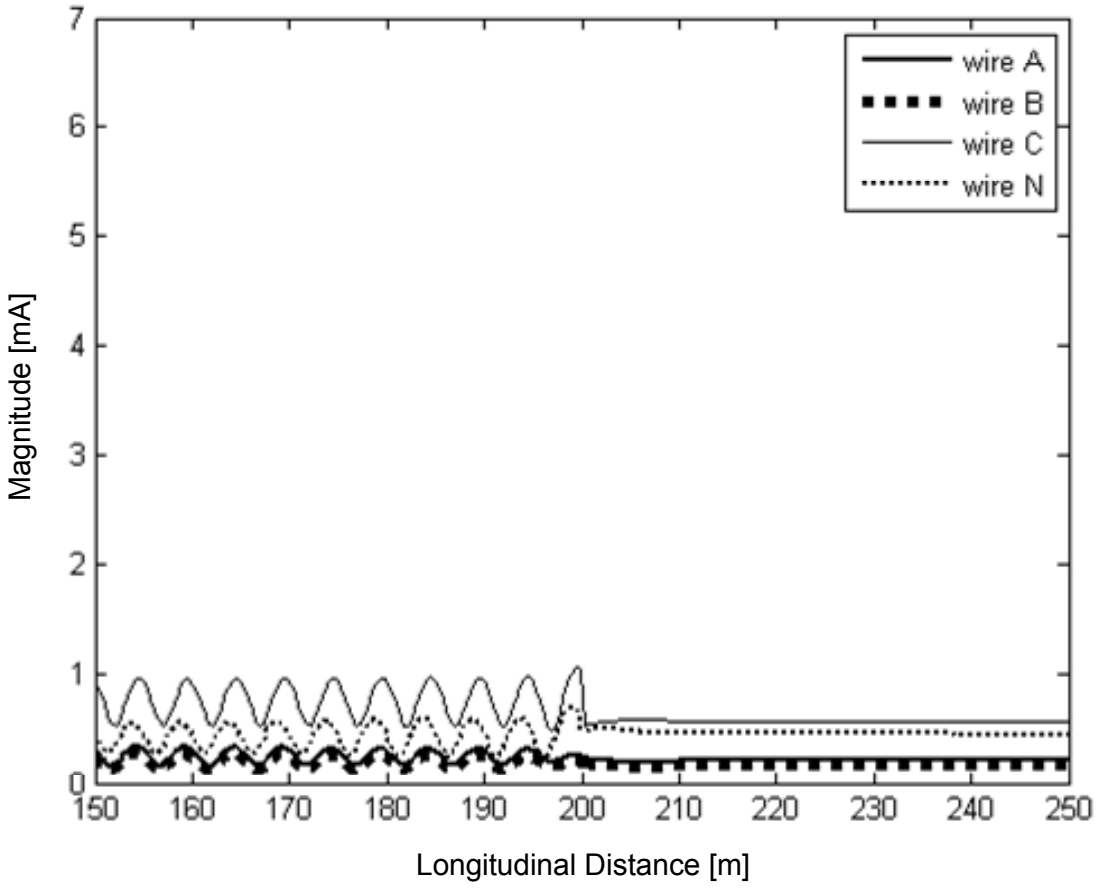

Figure 5.25 Expanded view along longitudinal distance of Figure 5.24 about the $x \approx +200$ meters utility pole.

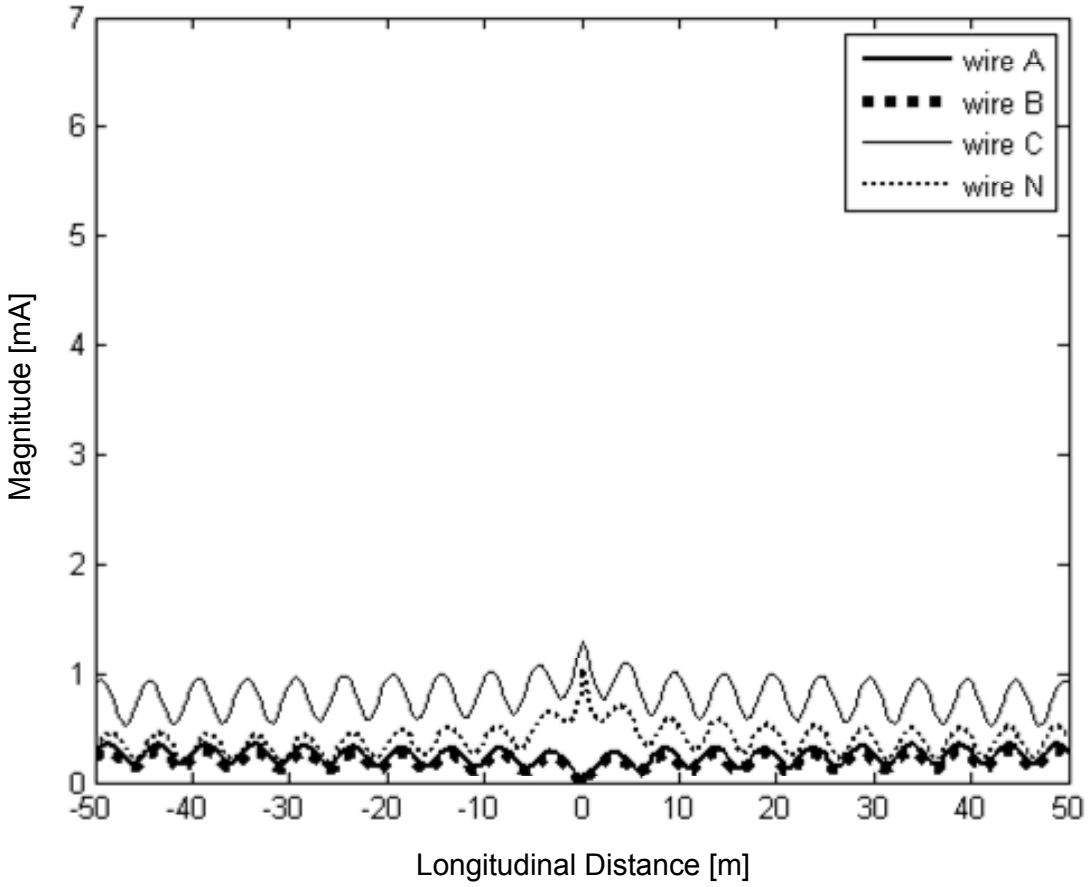

Figure 5.26 Expanded view along longitudinal distance of Figure 5.24 about the $x = 0$ utility pole.

Figures 5.27 through 5.32 show the field level along the FCC line from the different components of the current in the TX-RX configuration. It is still seen that the vertical currents are the main contributors to the total field fairly close to the utility pole (smaller longitudinal distance x) where the field level is the strongest. Farther away from the pole (larger longitudinal distance x) the field from the horizontal lines (A, B, C, N) again becomes dominant. Overall, the inclusion of the receivers has not drastically affected the peak field emission.

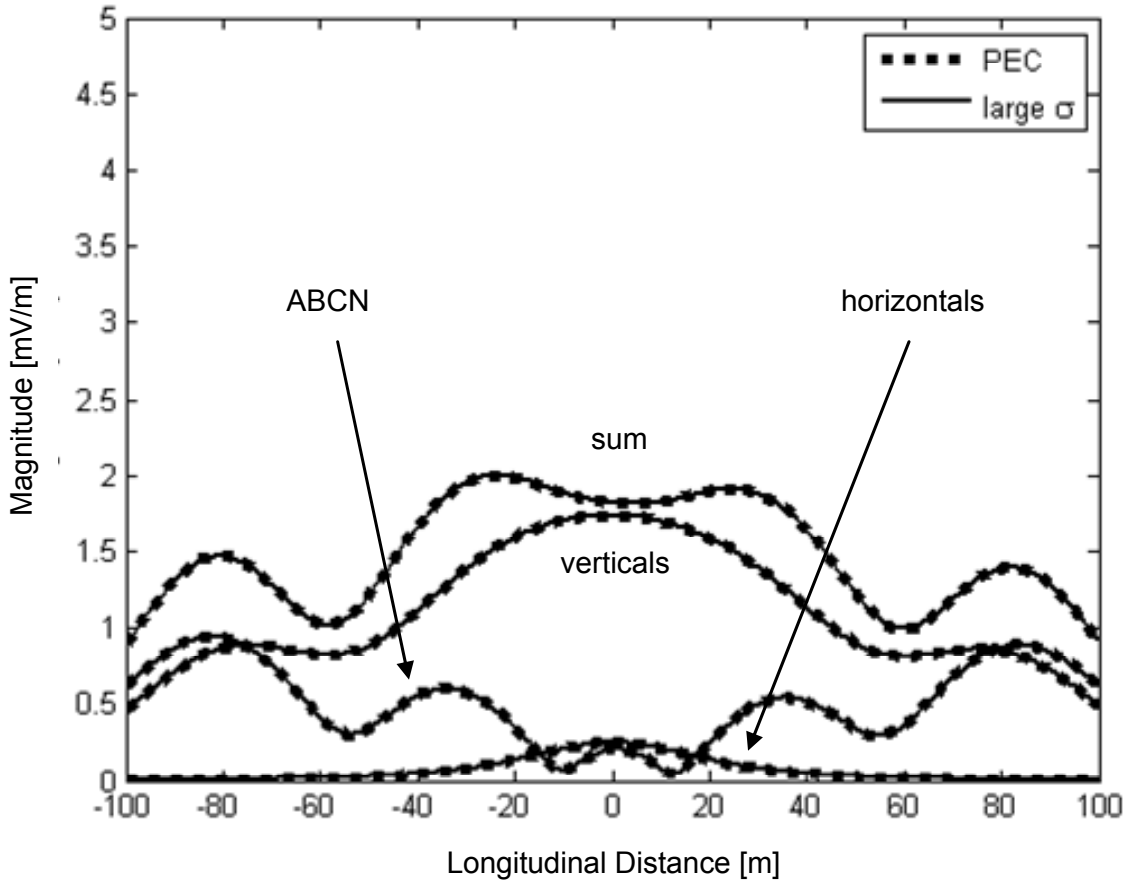

Figure 5.27 Vertical field of the TX-RX configuration along the earth ($z = 0$) on the $y > 0$ side of the FCC lines comparing between PEC and large σ earth at 3 MHz.

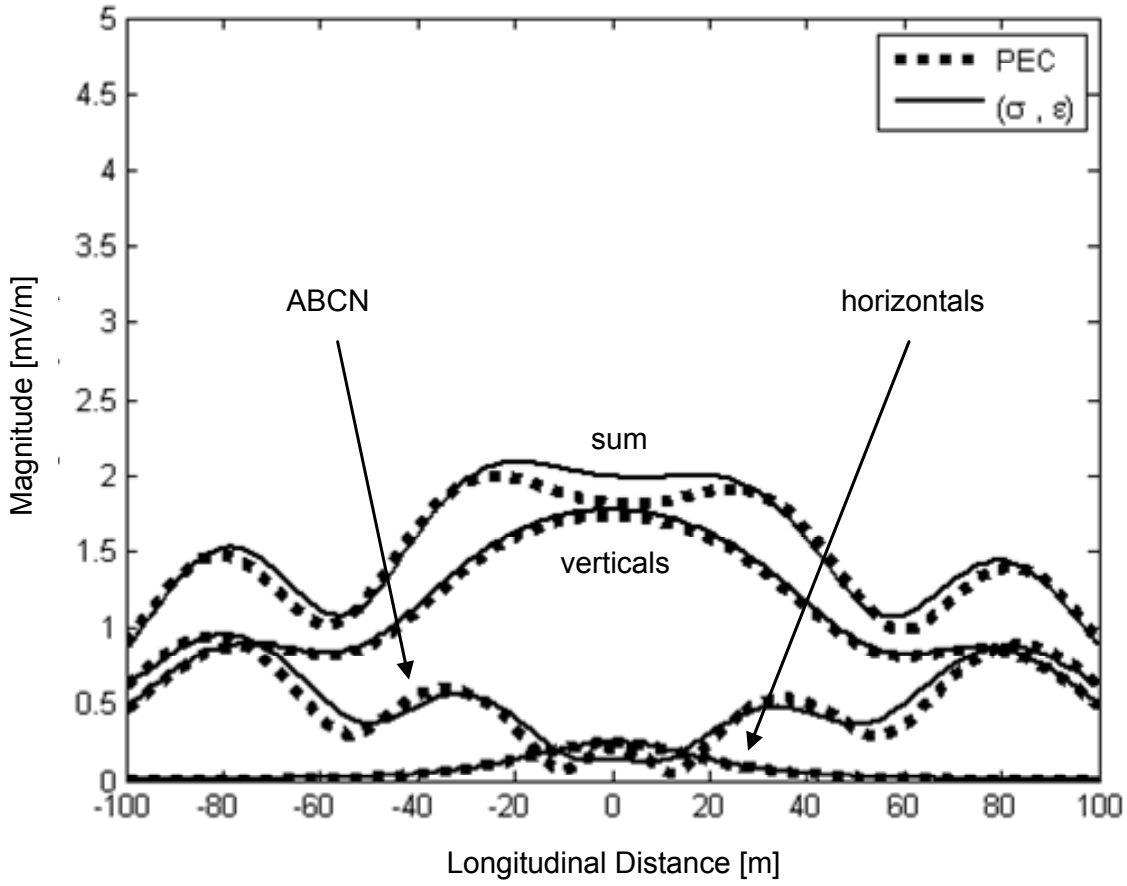

Figure 5.28 Same as Figure 5.27, except comparing with a finite σ earth.

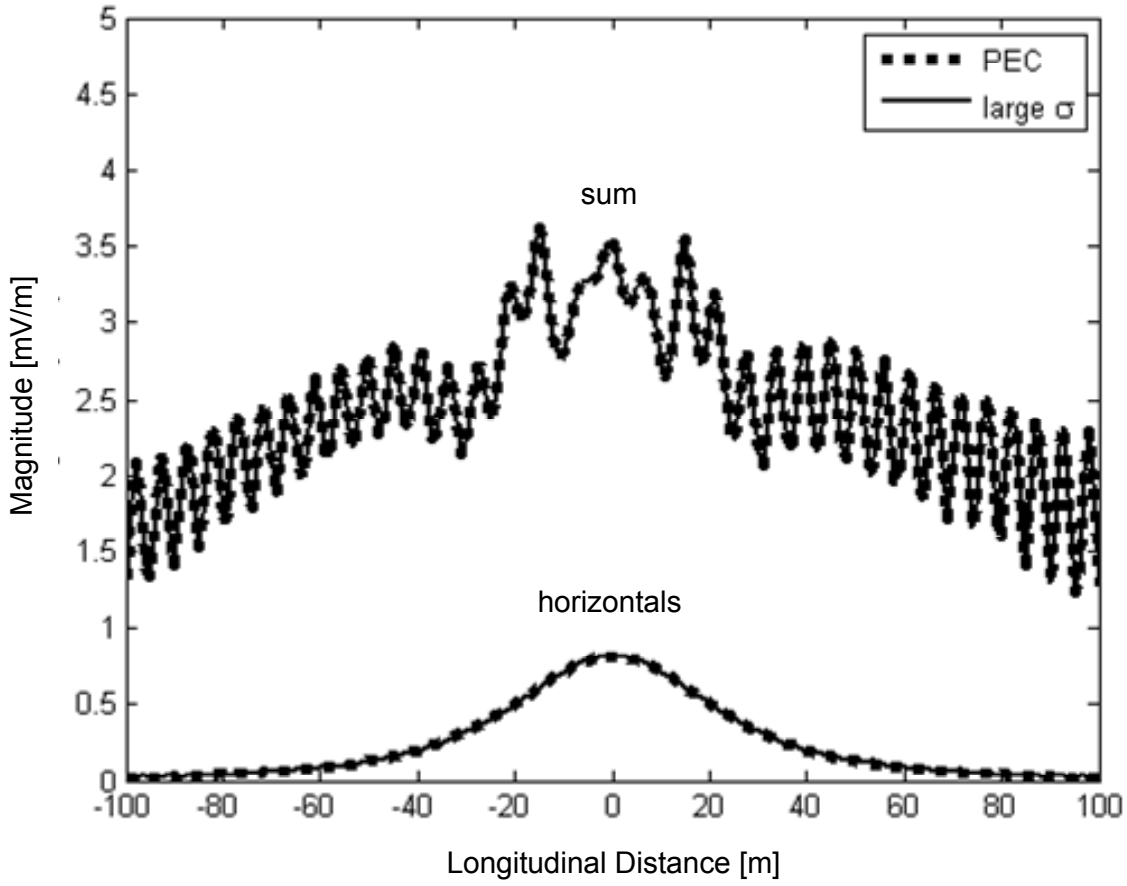

Figure 5.29 Same as Figure 5.27, except at 30 MHz, showing the total field and the field of the horizontal connector wires.

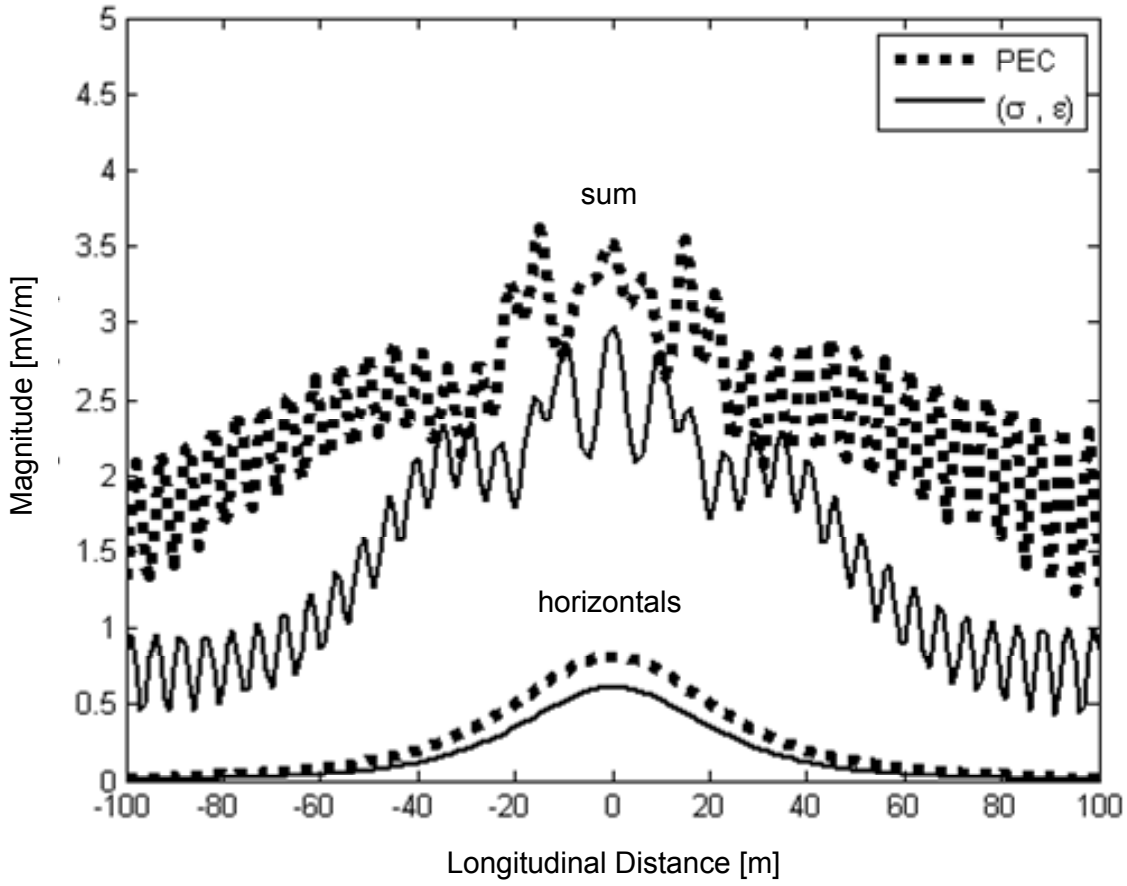

Figure 5.30 Same as Figure 5.28, except comparing with a finite σ earth model.

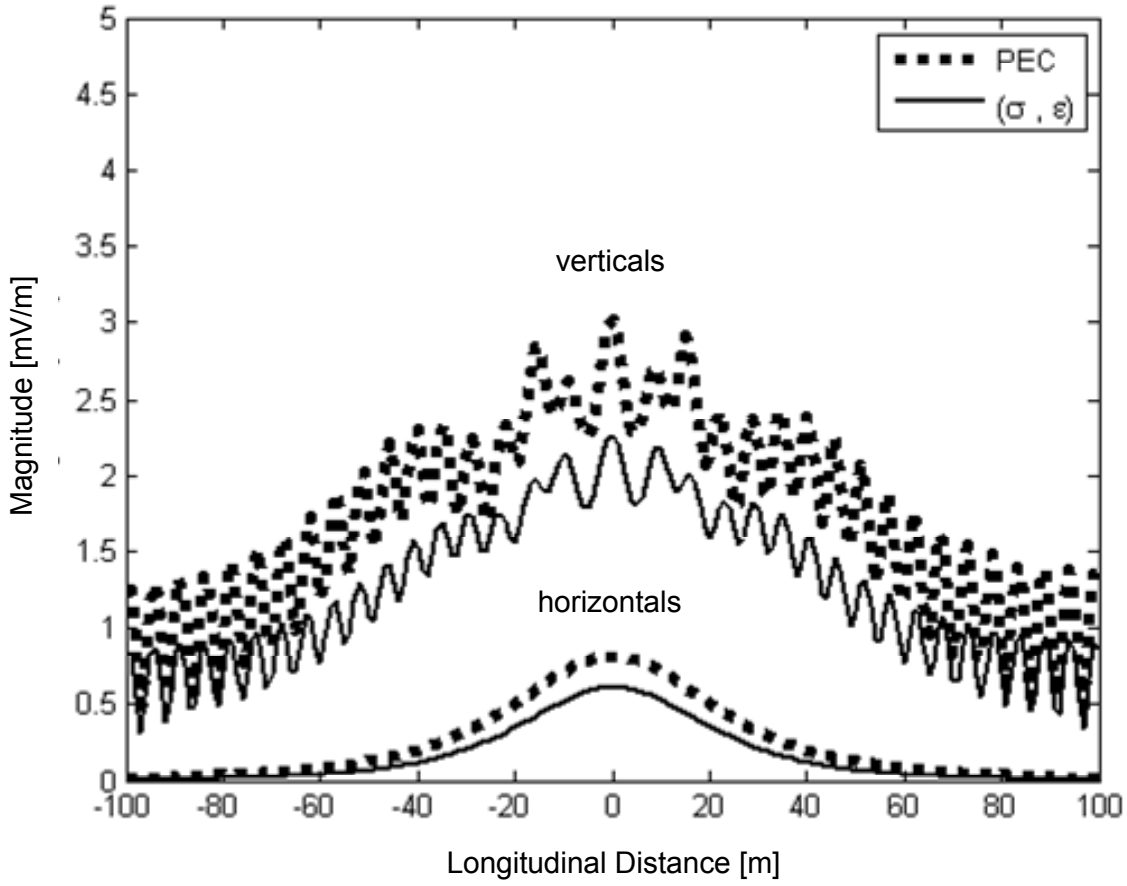

Figure 5.31 Same as Figure 5.30, except comparing with the field of the vertical currents.

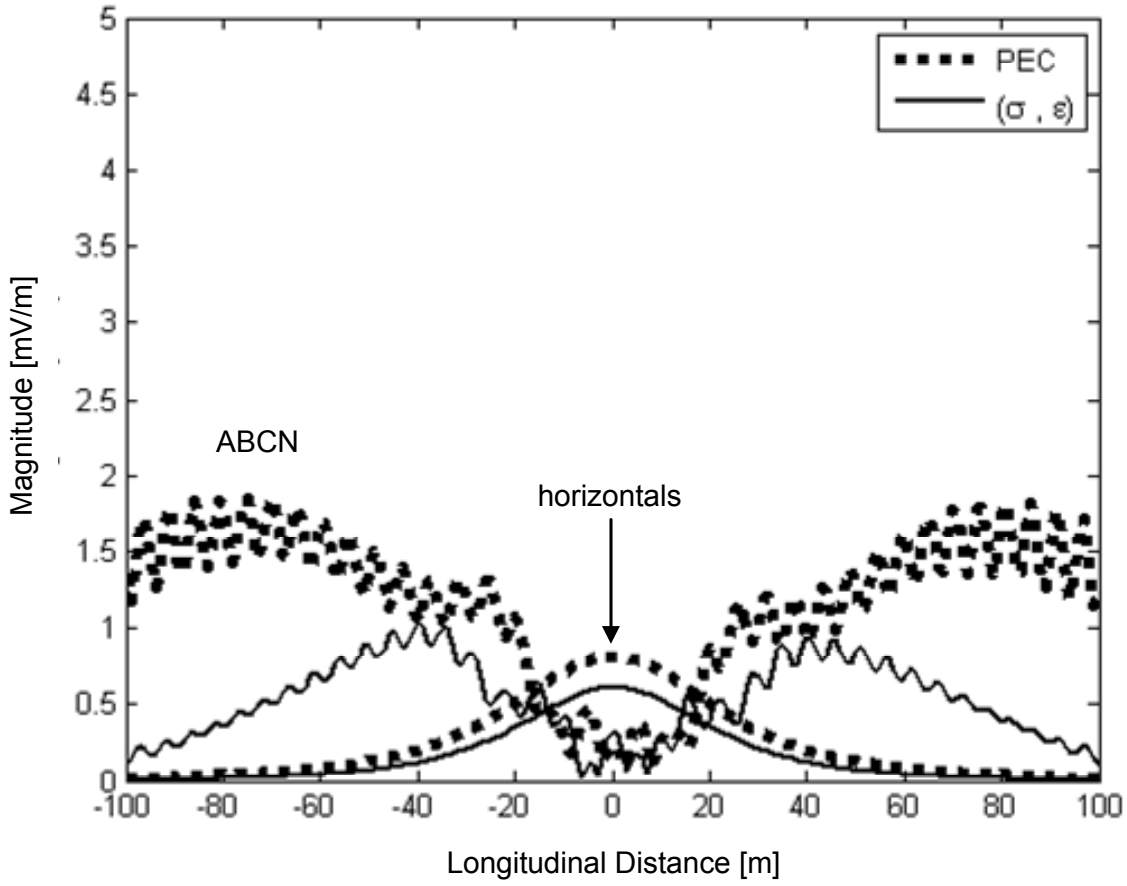

Figure 5.32 Same as Figure 5.30, except comparing with the field of the power line currents.

5.5 Summary

A summary of this chapter is presented in this section. The main concepts portrayed in this chapter are as follows:

1) There is a minimal effect by a finite σ earth on the near fields at 3 MHz.
2) There is reduction of the near-field field level along earth at 30 MHz.
3) A finite σ earth has a greater impact on the near fields from the power line currents (traveling-wave currents and space-wave currents) than with the other components of current.
4) The far-field patterns show a lobing effect in the E plane (the *xz* plane, parallel to the power line wires), but not in the H plane. Also, the presence of a finite σ earth affects the far-field pattern near the horizon, causing the pattern to have a null in this direction. Away from the horizon, the finite σ earth has minimal effect.
5) Power levels below 138 nW and 64 nW, for 3 and 30 MHz, respectively, would satisfy FCC regulations for a finite σ earth.
6) The presence of a receiver system causes standing-wave currents along the power line, which introduces spatial oscillations in the field level, though the overall level of the emitted field is not drastically changed.

Chapter 6

Conclusions

The canonical problem of a broadband over power line (BPL) source connected via feed lines to existing power lines over the earth has been investigated. In BPL, a radio-frequency source is used to transmit information over the existing power line infrastructure. This is an important practical problem since BPL transmission is being considered for various applications, while the FCC places a strict limit on the level of the emitted field from the BPL system. In particular, the field level at the BPL frequencies (typically raging from about 3 MHz to 30 MHz) is 30 μV/m at a distance of 30 meters away from the nearest power lines.

Although BPL sources on power lines have been studied in the past, this work has examined various practical connection schemes, i.e., different manners in which a BPL source can be connected to power lines in practical scenarios. The inclusion of the connecting feed lines from the BPL source to the power lines in important, as it was shown here that a significant amount of field emission from the BPL system emanates from the connector wires. Furthermore, the presented work compared the different feeding scenarios to ascertain which cases have the highest field emission and which have the lowest. This is a significant contribution as it allows for a practical assessment of realistic deployment schemes. Although most of the results were obtained by using a simple 1V BPL source for convenience, the results for the emitted fields can easily be scaled to reflect any value of the BPL voltage source that is desired. In this way, it can be determined what the maximum power level is of a BPL source, in order to conform to the FCC guidelines.

Throughout the dissertation, results have been provided for two particular frequencies, 3 MHz and 30 MHz. These frequencies represent the low and high ends of what is considered to be a typical frequency range for a BPL system.

Results were obtained for two different models of the earth. The earth has been modeled both as a PEC and as a semi-infinite region with a finite conductivity and a permittivity. For the case of a PEC earth, image theory is used, which simplifies the analysis. The spectral-domain immittance method had been employed to account for the finite conductivity and permittivity of the earth. This rigorous solution allowed us to examine the field along the earth at 3 and 30 MHz and to see the effects of the finite conductivity on the emitted fields.

Two different software packages were used to numerically solve for the currents on the entire system (including the power lines, the connecting wires that connect the BPL source to the power lines, and the grounding wire that is present on the utility pole). One is the software tool EMPACK 2000, and the other is the software tool 4nec2. Both use the method of moments to numerically solve the electric field integral equation (EFIE), treating the wires as perfect conductors, in order to obtain the currents on all of the conducting wires. Although both software packages use the same basic approach, their implementation in terms of basis functions is quite different, and so it is reasonable to use both packages to provide validation of the results. Results obtained with both packages show excellent agreement in most cases, providing confirmation that the currents on the system are accurate.

Once the currents have been obtained, the field radiated (emitted) by the currents were then found. Results have shown that the finite conductivity of the earth has little

effect on the currents at the low frequencies investigated here. This is especially true at 3 MHz, where the loss tangent of typical earth (modeled with a relative permittivity of 8, and a conductivity of 0.1 S/m) is about 75. For the higher frequency of 30 MHz, the loss tangent is about 7.5. Because of this, most of the currents were found by assuming the earth to be modeled as a PEC. The finite conductivity of the earth also has a negligible effect of the field level emitted by the BPL system at 3 MHz. At 30 MHz there is more of an effect, and the effect is the most noticeable on the field emitted by the traveling-wave and space-wave currents on the horizontal lines. The effect also becomes more pronounced for larger distance from the BPL source.

The finite conductivity of the earth is significant in modifying the field along the surface of the earth when the distance from the source becomes large. This is most pronounced in the far-field patterns of the system. It is seen that the finite conductivity modifies the far-field pattern shape near the surface of the earth, causing the pattern to have a null along the "horizon" (in the horizontal plane containing the surface of the earth). This is consistent with other layered media problems, as it is well known that the far-field of a source in a layered media generally has a far-field pattern null at the layer interface, a fact that can be shown using standard asymptotic analysis. The finite conductivity of the earth has little effect on the far-field pattern away from the horizon. It also has little effect on the emitted fields fairly close to the BPL source, which is of interest for the FCC guidelines.

All of the results were based on using one particular utility pole configuration, referred to as a "12 kV delta tangent" pole configuration by Centerpoint Energy. This configuration has a neutral wire running along the pole, roughly halfway up the pole.

The three phase lines (A, B, C) are near the top of the pole, with the pole being roughly 15.24 meters (50 feet) in height. The phase wire C is the lowest to the ground, with phase lines A and B above it. While the presented data is for this one particular pole configuration, one can apply the approach and principles discussed herein to any other specific installation.

Five different feeding scenarios, i.e., different practical ways to connect a BPL source to the various lines, were investigated. Case 1 places an inductive coupler directly on phase line C, and this is modeled as in inline voltage source. Phase C is chosen as it is closest to the ground, and would most likely be selected in a actual system that uses such a coupler. Cases 2-5 assume capacitive couplers, so that two feed wires coming from the BPL source make RF contact (via the capacitive connectors) with two different lines on the pole (out of the three phase lines and the neutral line), in essence creating a two-wire transmission using the two selected lines. Cases 2 and 3 use the BPL source to feed two of the three phase lines. Case 2 has the feed wires from the BPL source running vertically up the utility pole and then feeding phase wires B and C, with line B directly above line C. Case 3 has the two feed lines running vertically up the pole and then feeding phase lines A and B, which are both at the same height above the earth (both above phase line C). Cases 4 and 5 have the BPL source feeding the lowest phase wire, phase C, and the neutral wire. It is unlikely that a BL source would be used to feed an upper phase wire and the neutral wire. In case 4 the two feed lines from the BPL source run vertically up the utility pole until the height of the neutral wire is reached. The feed lines then branch off, with one connecting to the neutral wire and the other running further up the pole to connect to phase wire C. Hence, in this scenario the BPL source is

assumed to be mounted on the utility pole below the neutral wire. In case 5, the BPL source is also mounted on the utility pole, but one feed wire runs down the pole to connect to ground, while the other feed wire runs up the pole to connect to phase wire C.

Several interesting findings have been presented. First, it was concluded that case 4 gives the highest level of field emissions, when observed along the surface of the earth at the FCC lines. This assumes that the BPL source has a fixed voltage level. If the power level of the BPL source is fixed, then it is case 5 that actually has the highest emissions. This is due to a change in input impedance seen by the source in the two different cases. The difference between cases 4 and 5 is not large however, and these two cases may be taken as the worst-case scenarios for field emission. Case 3 has the lowest level of field emission.

It was shown that radiation from the BPL system is larger at the higher frequency (30 MHz), as expected. The reason would be that, at the higher frequency, there is a larger separation of the wires relative to a wavelength. Furthermore, currents naturally radiate more as the frequency is increased.

It was also shown that the emitted fields from the vertical feed wires and the vertical grounding wire on the pole cannot be neglected relative to the fields emitted from the horizontal power lines that are being excited by the BPL source. Even though the horizontal lines are much longer than the vertical wires, radiation is coming from the discontinuities (an infinite transmission line carrying a TEM transmission line wave will not radiate, even though there will be near fields in the surrounding region). Also, vertical currents in general tend to radiate more when placed over a conducting medium. Hence, even though they are shorter, the vertical wires (feed line and grounding wire) are

important. Near the utility pole, the field along the FCC lines is dominated by the field from the vertical currents. As the distance from the utility pole increases (increasing longitudinal distance x) the field from the horizontal lines becomes dominant. This is expected from transmission line theory, where far away from the pole the radiation fields will vanish and the remaining field will be a transmission-line field.

The far-field pattern exhibits multi-lobing in the E plane (the xz plane, parallel to the power lines) but not in the H plane (yz plane). In the E plane the field is primarily endfire directed. The presence of a finite-conductive earth causes the field to decay along the surface of the earth much more rapidly, and thus introduces a null in the far-field pattern at the horizon. Away from the horizon, the far-field pattern is not significantly affected by the finite conductivity.

The influence of receivers in the system was also studied. It was shown that the presence of receivers causes a standing-wave pattern to exist on the horizontal lines, as expected, due to a mismatch at the ends of the lines cased by the receivers. However, the overall level of the field emissions was not significantly increased by the presence of the receivers.

A practical conclusion from the results presented is that a signal generator that provides a power on the order of roughly 100 nanowatts or less should be able to meet the FCC regulation imposed on the field level (less than 30 μV/m at a horizontal distance of 30 meters away from the nearest line). Thus, the classification of being a current-carry system under FCC part 15 regulations regarding unlicensed devices can be satisfied.

The presented content is intended to provide a greater understanding of the various electromagnetic mechanisms and behaviors involved with BPL systems to

facilitate installation-specific analyses and technical approaches to address emission issues while increasing bandwidth utilization. The concepts discussed enable an engineering solution which would provide the greatest benefit for a broad range of applications.

References

[1] "Promoting Innovation and Economic Security Through Broadband Technology," The White House, 26 Apr. 2004. Web. Jan. 2, 2007.

[2] OSTP, CEQ, DOE, USDA, DOI, NIST. *Administration Announces Grid Modernization Initiatives to Foster a Clean Energy Economy and Spur Innovation*. Building the 21st Century Grid. Washington, D.C.: GPO, 13 June 2011.

[3] "First Draft for IEEE P1901™ Broadband Over Power Lines Standard Created by Working Group," IEEE Standards Association, 30 July 2009. Web. 25 Jan. 2011.

[4] Eileen O'Grady. "Texas Finalize Plan to Expand Wind Line," *Reuters*, 29 Jan. 2009. Web. 13 Nov. 2011.

[5] "Why Amateur Radio is Concerned about Its Deployment," ARRL, Mar. 2005. Web. 7 Nov. 2011.

[6] "IEEE EMC Society Standards Development Committee Withdraws as Cosponsor of IEEE BPL EMC Standard," ARRL, 18 Jan. 2011. Web. 7 Nov. 2011.

[7] "FCC Tightens BPL Interference Rules -- But Not By Enough," ARRL, 27 Oct. 2011. Web. 7 Nov. 2011.

[8] J. C. Richards and J. V. Williams. *Potential Interference from Broadband Over Power Line (BPL) Systems to Federal Government Radiocommunication Systems at 1.7 - 80 MHz: Phase 2 Study*. Washington, D.C.: U.S. Dept. of Commerce, NTIA, 5 Oct. 2007.

[9] R. G. Olsen, "Technical Considerations for Broadband Powerline (BPL) Communication," WA: WA State UP, Feb. 2005.

[10] FCC. *47 CFR Ch.1*. Washington, D.C.: GPO, 1 Oct. 2011.

[11] Ed Hare. *Methods of Feeding Overhead Electrical Power-Line Distribution Lines With BPL Signals and the Relationship of These Methods to the Radiated Emissions of the Conductors*. Newington: ARRL, 7 July 2003.

[12] Ed Hare. *Electric and Magnetic Fields Near Physically Large Radiators*. Newington: ARRL, 7 July 2003.

[13] Ed Hare. *Power Lines as Antennas From 100 kHz to 50 MHz*. Newington: ARRL, 7 July 2003.

[14] S. Cerwin, "Modeling Signal Leakage Characteristics of Broadband Over Power Line (BPL) using NEC with Experimental Verification", San Antonio: SWRI, 2006.

[15] Nachum. *Broadband Power Line Carrier Couplers*. Lawrence: Amperion Inc., Sept. 2011.

[16] "Couplers." Powerline Technologies Limited, 2004. Web. 13 Nov. 2011.

[17] *Corinex Medium Voltage Gateway*, Corinex Communications Corp., Nov. 2012.

[18] D. M. Pozar, *Microwave Engineering*, 3rd Ed. Hoboken, NJ: John Wiley & Sons, 2005.

[19] R. F. Harrington, *Time-Harmonic Electromagnetic Fields*, Hoboken, NJ: John Wiley & Sons, 2001.

[20] T. Itoh, "Spectral Domain Immittance Approach for Dispersion Characteristics of Generalized Printed Transmission Lines," *IEEE Trans. Microwave Theory and Techniques*, vol. 28, no. 7, pp. 733-736, July 1980.

[21] Facilities Joint Use Section. *Pole Attachment Guidelines and Procedures*. Houston, TX: CenterPoint Energy, 26 July 2007.

[22] M. N. Soutsos, "Dielectric Properties of Concrete and Their Influence on Radar Testing," *NDT & E International*, vol. 34, no. 6, pp. 419-425, Sept. 2001.

[23] G. E. Mueller and W. A. Tyrrell, "Polyrod Antennas," *Bell Syst. Tech. J.*, vol. 26, pp.837 -851, 1947.

[24] R. F. Harrington, *Field Computation by Moment Methods*, New York: IEEE press, 1993.

[25] W. A. Johnson , D. R. Wilton, and R. M. Sharpe, "Modeling scattering from and radiation by arbitrary shaped objects with the Electric Field Integral Equation Surface Patch Code," *Electromagnetics*, vol. 10, pp. 41-63, 1990.

[26] G. J. Burke and A. J. Poggio. *Numerical Electromagnetics Code (NEC)-Method of Moments*. LLNL, Jan. 1981.

[27] F. Mesa, D. R. Jackson, and M. J. Freire, "High-Frequency Leaky-Mode Excitation on a Microstrip Line," *IEEE Trans. Microwave Theory and Techniques*, vol. 49, no. 12, pp. 2206-2215, Dec. 2001.

[28] C. A. Balanis, *Antenna Theory: Analysis and Design*, 3rd Ed. Hoboken, NJ: John Wiley & Sons, 2005.

[29] K. A. Michalski and D. Zheng, "Electromagnetic Scattering and Radiation by Surfaces of Arbitrary Shape in Layered Media, Part I: Theory," *IEEE Trans. on Antennas and Propagation*, vol. 38, no. 3, pp. 335-344, Mar. 1990.

[30] L.F. Shampine "Vectorized Adaptive Quadrature in MATLAB," *Journal of Computational and Applied Mathematics*, vol. 211, no. 2, pp.131-140, Feb. 2008.

Appendix A: Formulation of E_z for Vertical Current Segment

This appendix presents the derivation of Equation (2.10) that had been noted in Section 2.3 regarding the E_z field component due to a vertical (z directed) segment of electric current along $z_2 \le z_i \le z_1$ with respect to the Figure 1.1 coordinate system. It is essentially the spatial integral of the SDI formulation similar to [29] for E_z due to a vertical electric dipole.

Since E_z for a vertical segment of current is based on the E_z from a dipole, the E_z field component for a dipole located at z_i shall first be obtained. In general, the approach would be to express an incident space domain E_z from a dipole source as a collection of spectral plane waves propagating normal to a xy-plane interface between different media. As each spectral plane wave interacts independently with the interface, the TEN model can be applied to obtain the overall spectral wave that includes any reflection and transmission due to the different media. With the collection of overall spectral plane waves, the E_z field is obtained via inverse Fourier transform back into the space domain.

In a source free region, Ampere's Law in the frequency domain is

$$\nabla \times \vec{H} = j\omega\varepsilon\vec{E} \ , \tag{A.1}$$

which means that

$$E_z = \frac{1}{j\omega\varepsilon}\left(\frac{\partial H_y}{\partial x} - \frac{\partial H_x}{\partial y}\right) . \tag{A.2}$$

A spatial Fourier transform of Equation (A.2) in the xy plane effectively brings E_z from the space domain into the spectral domain and can be expressed as

$$\tilde{E}_z = \frac{1}{j\omega\varepsilon}\left(-jk_x\tilde{H}_y + jk_y\tilde{H}_x\right) = \frac{1}{\omega\varepsilon}\left(-k_x\tilde{H}_y + k_y\tilde{H}_x\right) . \tag{A.3}$$

In anticipation of using a TEN that has a different impedance formulation between TM_z and TE_z waves, let $\hat{u}$ and $\hat{v}$ represent unit vectors in the direction where their corresponding component for a general sheet current would launch TM_z and TE_z waves, respectively. As implied, $\hat{u}$ is perpendicular to $\hat{v}$. Not unexpectedly, the sheet current component in the k_ρ direction launches TM_z waves and so $\hat{u}$ is the unit vector associated with k_ρ, which is defined in Equation (2.9). This allows the spectral domain magnetic field components to be written as

$$\tilde{H}_x = \left(\hat{u}\cdot\hat{x}\right)\tilde{H}_u + \left(\hat{v}\cdot\hat{y}\right)\tilde{H}_v = \left(\frac{k_x}{k_\rho}\right)\tilde{H}_u + \left(\frac{-k_y}{k_\rho}\right)\tilde{H}_v \tag{A.4}$$

and

$$\tilde{H}_y = \left(\hat{u}\cdot\hat{y}\right)\tilde{H}_u + \left(\hat{v}\cdot\hat{y}\right)\tilde{H}_v = \left(\frac{k_y}{k_\rho}\right)\tilde{H}_u + \left(\frac{k_x}{k_\rho}\right)\tilde{H}_v \ . \tag{A.5}$$

Applying Equations (A.4) and (A.5), Equation (A.3) becomes

$$\begin{aligned}\tilde{E}_z &= \frac{1}{\omega\varepsilon}\left(-k_x\left[\left(\frac{k_y}{k_\rho}\right)\tilde{H}_u + \left(\frac{k_x}{k_\rho}\right)\tilde{H}_v\right] + k_y\left[\left(\frac{k_x}{k_\rho}\right)\tilde{H}_u + \left(\frac{-k_y}{k_\rho}\right)\tilde{H}_v\right]\right)\\ &= \frac{1}{\omega\varepsilon}\left(\frac{-k_x^2}{k_\rho}\tilde{H}_v + \frac{-k_y^2}{k_\rho}\tilde{H}_v\right)\\ &= \frac{1}{\omega\varepsilon}\frac{-\left(k_x^2+k_y^2\right)}{k_\rho}\tilde{H}_v\end{aligned}$$

and this simplifies into

$$\tilde{E}_z = \frac{-1}{\omega\varepsilon}k_\rho\tilde{H}_v \tag{A.6}$$

with the use of Equation (2.9). The appearance of only $\tilde{H}_v$ in Equation (A.6) show that the *uv*-coordinate system is a better fit for $\tilde{E}_z$ than the *xy*-coordinate system. Given that

the TEN model for $\tilde{H}_v$ corresponds to I^{TM}, with TEN current representing the TM_z spectral-domain magnetic field, Equation (A.6) becomes

$$\tilde{E}_z\left(k_\rho, z, z_i\right) = \frac{-1}{\omega\varepsilon} k_\rho I^{TM}\left(k_\rho, z, z_i\right) \tag{A.7}$$

in a more descriptive form.

Obtaining the expression for I^{TM} can be systematically achieved by decomposing it into magnitude and transmission-line propagation components. The magnitude component is specific to the excitation source of interest, which would be a vertical dipole at $z = z_i$. For a single vertical electric dipole of amplitude $I^{vert}\left(z_i\right) \cdot \delta\left(z_i\right)$, only the surface current

$$J_z^i = I^{vert}\left(z_i\right) \cdot \delta\left(x\right)\delta\left(y\right)\delta\left(z_i\right) \tag{A.8}$$

exists and TM_z fields are produced. After a spatial Fourier transform in the *xy* plane, the space domain J_z^i becomes

$$\tilde{J}_z^i = I^{vert}\left(z_i\right) \cdot \delta\left(z_i\right) \tag{A.9}$$

in the spectral domain. By mapping the frequency-domain Maxwell's equations onto the *uv*-coordinate system then matching like terms of TM_z fields to the frequency-domain Telegrapher's equation, it is apparent that the differential inline voltage would be

$$V_s^{TM}\left(k_\rho\right) = \left(\frac{k_\rho}{\omega\varepsilon}\right)\tilde{J}_z^i = \left(\frac{k_\rho}{\omega\varepsilon}\right) \cdot I^{vert}\left(z_i\right) \tag{A.10}$$

since a vertical electric dipole does not have an M_v^i (magnetic surface current). Assuming that the electric dipole is directed in the positive *z* direction, V_s^{TM} would also be directed in the positive *z* direction. Like any differential inline voltage source along a

transmission line, an inline current is excited and would propagate away from V_s^{TM}. Denoted as I_v^{TM}, it represents the propagation of a TEN transmission-line current due to a differential inline unit voltage source. Thus, the TEN current representing TM_z spectral-domain magnetic fields can be expressed as

$$I^{TM}\left(k_\rho, z, z_i\right) = I_v^{TM}\left(k_\rho, z, z_i\right) \cdot V_s^{TM}\left(k_\rho\right) = I_v^{TM}\left(k_\rho, z, z_i\right) \cdot \left(\frac{k_\rho}{\omega\varepsilon}\right) \cdot I^{vert}\left(z_i\right) , \quad \text{(A.11)}$$

where I_v^{TM} is defined by Equation (5.25).

Having found Equation (A.11), all the necessary components to obtain the E_z are in place. Applying Equation (A.11), Equation (A.7) becomes

$$\tilde{E}_z\left(k_\rho, z, z_i\right) = \frac{-1}{\omega\varepsilon} k_\rho \cdot I_v^{TM}\left(k_\rho, z, z_i\right) \cdot \left(\frac{k_\rho}{\omega\varepsilon}\right) \cdot I^{vert}\left(z_i\right) . \quad \text{(A.12)}$$

An inverse Fourier transform of Equation (A.12) in the $k_x k_y$ plane effectively brings $\tilde{E}_z$ from the spectral domain back into the space domain and can be expressed as

$$E_z^{dip}\left(x, y, z, z_i\right) = \frac{1}{\left(2\pi\right)^2} \int_{-\infty}^{\infty}\int_{-\infty}^{\infty} \frac{-1}{\omega\varepsilon} k_\rho \cdot I_v^{TM}\left(k_\rho, z, z_i\right) \cdot \left(\frac{k_\rho}{\omega\varepsilon}\right) \cdot I^{vert}\left(z_i\right) e^{-j\left(k_x x + k_y y\right)} dk_x dk_y , \quad \text{(A.13)}$$

where the superscript "dip" indicate that the E_z is due to a dipole source. It would be computationally advantageous to represent Equation (A.13) as a single integral and the progression to such a form can be seen as

$$\begin{aligned} E_z^{dip}\left(x, y, z, z_i\right) &= \frac{1}{\left(2\pi\right)^2} \int_{-\infty}^{\infty}\int_{-\infty}^{\infty} \frac{-1}{\omega\varepsilon} k_\rho \cdot I_v^{TM}\left(k_\rho, z, z_i\right) \cdot \left(\frac{k_\rho}{\omega\varepsilon}\right) \cdot I^{vert}\left(z_i\right) e^{-j\left(k_x x + k_y y\right)} dk_x dk_y \\ &= \frac{-I^{vert}\left(z_i\right)}{\left(2\pi\omega\varepsilon\right)^2} \int_{-\infty}^{\infty}\int_{-\infty}^{\infty} k_\rho^2 \, I_v^{TM}\left(k_\rho, z, z_i\right) e^{-j\left(k_x x + k_y y\right)} dk_x dk_y \\ &= \frac{-I^{vert}\left(z_i\right)}{\left(2\pi\omega\varepsilon\right)^2} \int_{0}^{\infty}\int_{0}^{2\pi} k_\rho^2 \, I_v^{TM}\left(k_\rho, z, z_i\right) e^{-j\left[k_\rho \cos\left(\phi_{k_\rho}\right)\cdot\rho\cdot\cos(\phi) + k_\rho \sin\left(\phi_{k_\rho}\right)\cdot\rho\cdot\sin(\phi)\right]} k_\rho dk_\rho d\phi_{k_\rho} \end{aligned}$$

$$E_z^{dip}(x,y,z,z_i) = \frac{-I^{vert}(z_i)}{(2\pi\omega\varepsilon)^2}\int_0^{\infty}\int_0^{2\pi} k_\rho^2\, I_v^{TM}(k_\rho,z,z_i)\; e^{-j\left[k_\rho\cos\left(\phi_{k_\rho}\right)\cdot\rho\cdot\cos(\phi)+k_\rho\sin\left(\phi_{k_\rho}\right)\cdot\rho\cdot\sin(\phi)\right]} k_\rho dk_\rho d\phi_{k_\rho}$$

$$= \frac{-I^{vert}(z_i)}{(2\pi\omega\varepsilon)^2}\int_0^{\infty} k_\rho^3\, I_v^{TM}(k_\rho,z,z_i)\left[\int_0^{2\pi} e^{-jk_\rho\cos\left(\phi_{k_\rho}-\phi\right)} d\phi_{k_\rho}\right] dk_\rho$$

$$= \frac{-I^{vert}(z_i)}{(2\pi\omega\varepsilon)^2}\int_0^{\infty} k_\rho^3\, I_v^{TM}(k_\rho,z,z_i)\left[\int_{0-\phi}^{2\pi-\phi} e^{-jk_\rho\cos(\alpha)} d\alpha\right] dk_\rho$$

$$= \frac{-I^{vert}(z_i)}{(2\pi\omega\varepsilon)^2}\int_0^{\infty} k_\rho^3\, I_v^{TM}(k_\rho,z,z_i)\cdot 2\pi J_0(k_\rho\rho)\, dk_\rho$$

to become

$$E_z^{dip}(x,y,z,z_i) = \frac{-I^{vert}(z_i)}{2\pi(\omega\varepsilon)^2}\int_0^{\infty} J_0(k_\rho\rho)\; I_v^{TM}(k_\rho,z,z_i)\; k_\rho^3 dk_\rho \ , \qquad \text{(A.14)}$$

where J_0 denotes the zero-order Bessel function. Therefore, the E_z field component due to a vertical segment of electric current along $z_2 \le z_i \le z_1$ is obtained by

$$E_z = \int_{z_2}^{z_1} E_z^{dip}(x,y,z,z_i)\, dz_i = \int_{z_2}^{z_1} \frac{-I^{vert}(z_i)}{2\pi(\omega\varepsilon)^2}\int_0^{\infty} J_0(k_\rho\rho)\; I_v^{TM}(k_\rho,z,z_i)\; k_\rho^3 dk_\rho dz_i \ . \qquad \text{(A.15)}$$

Appendix B: Sufficiency of Wire Conductivity for PEC

This appendix presents the validation for sufficiency of wire conductivity mentioned in Section 2.4 to treat the wires involved with BPL models as PEC. Though the use of PEC for the wires is not essential, it is appealing in being able to minimize extraneous complexities and enabling a focus on more beneficial aspects of the analyses.

To begin, suppose there exists in air a wire composed of material with conductivity σ and relative permittivity $\varepsilon'_{r,wire}$ that has an equivalent surface current as illustrated in Figure 2.3(e). At an infinitesimal distance above a differential surface on the wire, the surface may be considered flat. From Section 2.4, it was noted that the skin depth is significantly smaller than the wire radius. This permits the region below the differential wire surface to be modeled as a semi-infinite lossy medium from the perspective of the plane waves since the wave is expected to diminish quickly within the wire. Thus, the scenario is basically a two layer medium involving a surface current on the air portion of the interface.

For such a situation, the tangential electric field can be obtained via SDI method. This implies the use of a transverse equivalent network (TEN) model similar in principle to Figure 2.2 as transmission line theory is involved. One difference is that both TM and TE components are needed to find the total tangential field. Aside from the source, the TEN model for the noted scenario would entail a lossless transmission line segment representing air terminated by a lossy transmission line representing the wire.

The reflection on the air side of the interface for such a setup can be expressed as

$$\Gamma^P\left(k_t\right)=\frac{Z_1^P\left(k_t\right)-Z_0^P\left(k_t\right)}{Z_1^P\left(k_t\right)+Z_0^P\left(k_t\right)}\ , \tag{B.1}$$

where the superscript "P" denotes either "TM" or "TE" while $Z_0^P(k_t)$ and $Z_1^P(k_t)$ would be the spectral wave impedance corresponding to air and wire, respectively. The spectral variable k_t, from a computational perspective, is essentially an integrating variable needed in the SDI method. The reflection experienced by the TM component can be found by combining Equation (B.1),

$$\varepsilon_{r,wire} = \varepsilon'_{r,wire}\left(1 - j\tan\delta_{wire}\right) = \varepsilon'_{r,wire} - j\frac{\sigma}{\omega\varepsilon_0}\ , \tag{B.2}$$

and using Equations (5.15) through (5.19) after substituting "ρ" with "t" (representing properties tangential to the differential wire surface), "z" with "n" (representing properties normal to the differential wire surface), as well as "*earth*" with "*wire*". The progression can be seen as

$$\begin{aligned}
\Gamma^{TM}(k_t) &= \frac{Z_1^{TM}(k_t) - Z_0^{TM}(k_t)}{Z_1^{TM}(k_t) + Z_0^{TM}(k_t)} \\
&= \frac{\dfrac{k_{n1}(k_t)}{\omega\varepsilon_0}\dfrac{1}{\varepsilon_{r,wire}} - \dfrac{k_{n0}(k_t)}{\omega\varepsilon_0}}{\dfrac{k_{n1}(k_t)}{\omega\varepsilon_0}\dfrac{1}{\varepsilon_{r,wire}} + \dfrac{k_{n0}(k_t)}{\omega\varepsilon_0}} \\
&= \frac{k_{n1}(k_t) - \varepsilon_{r,wire}k_{n0}(k_t)}{k_{n1}(k_t) + \varepsilon_{r,wire}k_{n0}(k_t)} \\
&= \frac{\sqrt{k_0^2\left(\varepsilon'_{r,wire} - j\dfrac{\sigma}{\omega\varepsilon_0}\right) - k_t^2} - \left(\varepsilon'_{r,wire} - j\dfrac{\sigma}{\omega\varepsilon_0}\right)\sqrt{k_0^2 - k_t^2}}{\sqrt{k_0^2\left(\varepsilon'_{r,wire} - j\dfrac{\sigma}{\omega\varepsilon_0}\right) - k_t^2} + \left(\varepsilon'_{r,wire} - j\dfrac{\sigma}{\omega\varepsilon_0}\right)\sqrt{k_0^2 - k_t^2}} \\
&= \frac{\sqrt{\left(\varepsilon'_{r,wire} - j\dfrac{\sigma}{\omega\varepsilon_0}\right) - \bar{k}_t^2} - \left(\varepsilon'_{r,wire} - j\dfrac{\sigma}{\omega\varepsilon_0}\right)\sqrt{1 - \bar{k}_t^2}}{\sqrt{\left(\varepsilon'_{r,wire} - j\dfrac{\sigma}{\omega\varepsilon_0}\right) - \bar{k}_t^2} + \left(\varepsilon'_{r,wire} - j\dfrac{\sigma}{\omega\varepsilon_0}\right)\sqrt{1 - \bar{k}_t^2}}
\end{aligned}$$

to become

$$\Gamma^{TM}\left(k_t\right)=\frac{1-\left(\varepsilon'_{r,wire}-j\frac{\sigma}{\omega\varepsilon_0}\right)\sqrt{\frac{1-\overline{k}_t^{\,2}}{\left(\varepsilon'_{r,wire}-j\frac{\sigma}{\omega\varepsilon_0}\right)-\overline{k}_t^{\,2}}}}{1+\left(\varepsilon'_{r,wire}-j\frac{\sigma}{\omega\varepsilon_0}\right)\sqrt{\frac{1-\overline{k}_t^{\,2}}{\left(\varepsilon'_{r,wire}-j\frac{\sigma}{\omega\varepsilon_0}\right)-\overline{k}_t^{\,2}}}}\ , \tag{B.3}$$

where $\overline{k}_t$ is k_t normalized by k_0. At 30 MHz, aluminum ($\sigma \approx 3.5\cdot 10^7$ S/m) gives $\frac{\sigma}{\omega\varepsilon_0}\approx 2.1\cdot 10^{10}$, which means that $\Gamma^{TM}\left(k_t\right)\approx -1$ along any given path of integration on the complex k_t plane involved with the SDI method. The reflection experienced by the TE component can be found by combining Equations (B.1) and (B.2) along with

$$Z_0^{TE}\left(k_t\right)=\frac{\omega\mu_0}{k_{n0}\left(k_t\right)} \tag{B.4}$$

and

$$Z_1^{TE}\left(k_t\right)=\frac{\omega\mu_1}{k_{n1}\left(k_t\right)}=\frac{\omega\mu_0\mu_{r,wire}}{k_{n1}\left(k_t\right)}=\frac{\omega\mu_0}{k_{n1}\left(k_t\right)}\ , \tag{B.5}$$

where $\mu_{r,wire}=1$. The progression can be seen as

$$\begin{aligned}\Gamma^{TE}\left(k_t\right)&=\frac{Z_1^{TE}\left(k_t\right)-Z_0^{TE}\left(k_t\right)}{Z_1^{TE}\left(k_t\right)+Z_0^{TE}\left(k_t\right)}\\&=\frac{\frac{\omega\mu_0}{k_{y1}\left(k_t\right)}-\frac{\omega\mu_0}{k_{y0}\left(k_t\right)}}{\frac{\omega\mu_0}{k_{y1}\left(k_t\right)}+\frac{\omega\mu_0}{k_{y0}\left(k_t\right)}}\\&=\frac{k_{y0}\left(k_t\right)-k_{y1}\left(k_t\right)}{k_{y0}\left(k_t\right)+k_{y1}\left(k_t\right)}\end{aligned}$$

$$\Gamma^{TE}\left(k_t\right)=\frac{k_{y0}\left(k_t\right)-k_{y1}\left(k_t\right)}{k_{y0}\left(k_t\right)+k_{y1}\left(k_t\right)}$$
$$=\frac{\sqrt{k_0^2-k_t^2}-\sqrt{k_0^2\left(\varepsilon'_{r,wire}-j\frac{\sigma}{\omega\varepsilon_0}\right)-k_t^2}}{\sqrt{k_0^2-k_t^2}+\sqrt{k_0^2\left(\varepsilon'_{r,wire}-j\frac{\sigma}{\omega\varepsilon_0}\right)-k_t^2}}$$
$$=\frac{\sqrt{1-\overline{k}_t^2}-\sqrt{\left(\varepsilon'_{r,wire}-j\frac{\sigma}{\omega\varepsilon_0}\right)-\overline{k}_t^2}}{\sqrt{1-\overline{k}_t^2}+\sqrt{\left(\varepsilon'_{r,wire}-j\frac{\sigma}{\omega\varepsilon_0}\right)-\overline{k}_t^2}}$$

to become

$$\Gamma^{TE}\left(k_t\right)=\frac{1-\sqrt{\frac{\left(\varepsilon'_{r,wire}-j\frac{\sigma}{\omega\varepsilon_0}\right)-\overline{k}_t^2}{1-\overline{k}_t^2}}}{1+\sqrt{\frac{\left(\varepsilon'_{r,wire}-j\frac{\sigma}{\omega\varepsilon_0}\right)-\overline{k}_t^2}{1-\overline{k}_t^2}}}\ . \tag{B.6}$$

At 30 MHz, $\frac{\sigma}{\omega\varepsilon_0}\approx 2.1\cdot 10^{10}$ for aluminum, which means that $\Gamma^{TE}\left(k_t\right)\approx -1$ along any given path of integration on the complex k_t plane involved with the SDI method.

Since $\Gamma^{TM}\left(k_t\right)$ and $\Gamma^{TE}\left(k_t\right)$ are essentially -1 for aluminum at 30 MHz, the TM and TE components of the TEN at the differential surface would be effectively zero. Thus, the tangential fields at the differential surface are also zero, which is a defining property of a PEC surface. Note that for a larger value of σ or a smaller frequency, the value of $\frac{\sigma}{\omega\varepsilon_0}$ would increase. This makes the reflection even more close to -1 and further improves the PEC approximation. Thus, the wire conductivities mentioned in Section 2.4 are sufficient at 3 and 30 MHz to allow treatment as PEC.

Appendix C: Formulation to Compute E_z^{dip} Near the Dipole

This appendix presents the derivation to facilitate the computation of E_z^{dip} for observations near the dipole source. It is convenient since there are BPL cell models that involve a grounding wire, which makes a direct connection to the earth. For example, Figure 4.3 illustrate that the vertical grounding wire current is not zero at the interface and so the lower limit of Equation (A.15) in the outer integral, z_2, would be zero. On various surface plots, such as Figure 5.14, the vertical electric field were observed along the earth ($z = 0$) and presents a computational complication when near the grounding wire. Even with the use of Gauss-Kronrod quadrature [30] on Equation (A.15), there are sampling points of z_i very close to $z = 0$. The complication for such sampled z_i points arises primarily with Equation (A.14) when $z - z_i \approx 0$ since the lower decay rate of the integrand also means a slower integration convergence. Thus, the E_z^{dip} formulation is arranged to better utilize computational resources when observing vertical fields near the dipole source to enable the same for grounding wire currents.

To begin, suppose the integral of Equation (A.14) is separated at $k_\rho = a$ into two parts as

$$E_z^{dip}\left(x,y,z,z_i\right) = \frac{-I^{vert}\left(z_i\right)}{2\pi\omega\varepsilon}\cdot\left(\mathrm{I}_{0\to a} + \mathrm{I}_{a\to\infty}\right) , \tag{C.1}$$

where

$$\mathrm{I}_{0\to a} = \frac{1}{\omega\varepsilon}\int_0^a J_0\left(k_\rho\rho\right)\, I_v^{TM}\left(k_\rho,z,z_i\right)\, k_\rho^3 dk_\rho \tag{C.2}$$

and

$$\mathrm{I}_{a\to\infty} = \frac{1}{\omega\varepsilon}\int_a^\infty J_0\left(k_\rho\rho\right)\, I_v^{TM}\left(k_\rho, z, z_i\right)\, k_\rho^3 dk_\rho \ . \tag{C.3}$$

Expanding Equation (C.3) with Equation (5.25),

$$\mathrm{I}_{a\to\infty} = \frac{1}{\omega\varepsilon}\int_a^\infty J_0\left(k_\rho\rho\right)\, \frac{T_i^{TM}\left(k_\rho, z, z_i\right)}{Z_0^{TM}\left(k_\rho\right) + Z_{in}^{TM}\left(k_\rho, z_i\right)}\, k_\rho^3 dk_\rho \ . \tag{C.4}$$

After applying Equations (5.12) through (5.15) followed by some simplification,

$$\mathrm{I}_{a\to\infty} = \int_a^\infty J_0\left(k_\rho\rho\right)\cdot\left[\frac{1}{k_{z0}\left(k_\rho\right)}\left(e^{jk_{z0}\left(k_\rho\right)\cdot z} - \Gamma^{TM}\left(k_\rho\right)e^{-jk_{z0}\left(k_\rho\right)\cdot z}\right)e^{-jk_{z0}\left(k_\rho\right)\cdot z_i}\right]k_\rho^3 dk_\rho \ . \tag{C.5}$$

When a is sufficiently large, $k_{z0} \simeq -jk_\rho$ and $\Gamma^{TM} \simeq \dfrac{1-\varepsilon_{r,earth}}{1+\varepsilon_{r,earth}}$. Hence, the asymptotic form of Equation (C.5) would be

$$\mathrm{I}_{a\to\infty} \simeq \tilde{\tilde{\mathrm{I}}}_{a\to\infty} = j\int_a^\infty J_0\left(k_\rho\rho\right)\cdot\left(e^{-k_\rho\left(z_i - z\right)} - \frac{1-\varepsilon_{r,earth}}{1+\varepsilon_{r,earth}}e^{-k_\rho\left(z_i + z\right)}\right)k_\rho^2 dk_\rho \ , \tag{C.6}$$

after rearranging and simplifying some terms.

Note that Equation (C.6) has strong similarity to an inverse Laplace transform. To ease the recognition of form, let $s = k_\rho$, $\alpha_1 = z_i - z$, and $\alpha_2 = z_i + z$ so that

$$\tilde{\tilde{\mathrm{I}}}_{a\to\infty} = j\int_a^\infty s^2 J_0\left(\rho\cdot s\right)\cdot\left(e^{-\alpha_1 s} + \frac{\varepsilon_{r,earth}-1}{\varepsilon_{r,earth}+1}e^{-\alpha_2 s}\right)ds \ . \tag{C.7}$$

By defining

$$f = \int_0^\infty s^2 J_0\left(\rho\cdot s\right)e^{-\alpha s}ds \ , \tag{C.8}$$

Equation (C.7) can be expressed as

$$\tilde{\tilde{\mathrm{I}}}_{a\to\infty} = j\cdot\sum_{elem}\left\{\begin{array}{c} f_1+\dfrac{\varepsilon_{r,earth}-1}{\varepsilon_{r,earth}+1}f_2 \\ -\displaystyle\int_0^a s^2 J_0\left(\rho\cdot s\right)\cdot\left(e^{-k_\rho\alpha_1}+\dfrac{\varepsilon_{r,earth}-1}{\varepsilon_{r,earth}+1}e^{-k_\rho\alpha_2}\right)ds \end{array}\right\}, \tag{C.9}$$

where f_1 and f_2 corresponds to α_1 and α_2. Note that $\sum_{elem}$ represents the summation of all contents between the braces. The progression to show that the function f is an inverse Laplace transform would be

$$\begin{aligned} f &= \int_0^\infty s^2 J_0\left(\rho\cdot s\right)e^{-\alpha s}ds \\ &= \mathcal{L}^{-1}\left\{F\left(s\right)=s^2 J_0\left(\rho\cdot s\right)\right\} \\ &= \left(-1\right)^2\frac{\partial^2}{\partial\alpha^2}\left(\mathcal{L}^{-1}\left\{F\left(s\right)=J_0\left(\rho\cdot s\right)\right\}\right) \\ &= \frac{\partial^2}{\partial\alpha^2}\left(\alpha^2+\rho^2\right)^{-1/2} \end{aligned}$$

to become

$$f = 3\alpha^2\left(\alpha^2+\rho^2\right)^{-5/2}-\left(\alpha^2+\rho^2\right)^{-3/2}\ . \tag{C.10}$$

When Equations (C.7) through (C.10) are considered, Equation (C.6) becomes

$$\mathrm{I}_{a\to\infty}\simeq j\sum_{elem}\left\{\begin{array}{c} 3\alpha_1^2\left(\alpha_1^2+\rho^2\right)^{-5/2}-\left(\alpha_1^2+\rho^2\right)^{-3/2} \\ \dfrac{\varepsilon_{r,earth}-1}{\varepsilon_{r,earth}+1}\left[3\alpha_2^2\left(\alpha_2^2+\rho^2\right)^{-5/2}-\left(\alpha_2^2+\rho^2\right)^{-3/2}\right] \\ -\displaystyle\int_0^a k_\rho^2 J_0\left(k_\rho\rho\right)\cdot\left(e^{-k_\rho\left(z_i-z\right)}+\dfrac{\varepsilon_{r,earth}-1}{\varepsilon_{r,earth}+1}e^{-k_\rho\left(z_i+z\right)}\right)dk_\rho \end{array}\right\}. \tag{C.11}$$

Combining Equations (C.2) and (C.11), Equation (C.1) becomes

$$E_z^{dip}\left(x,y,z,z_i\right)=\frac{-I^{vert}\left(z_i\right)}{2\pi\omega\varepsilon}\sum_{elem}\left\{\begin{array}{c} 3\alpha_1^2\left(\alpha_1^2+\rho^2\right)^{-5/2}-\left(\alpha_1^2+\rho^2\right)^{-3/2} \\ \frac{\varepsilon_{r,earth}-1}{\varepsilon_{r,earth}+1}\left[3\alpha_2^2\left(\alpha_2^2+\rho^2\right)^{-5/2}-\left(\alpha_2^2+\rho^2\right)^{-3/2}\right] \\ -\int_0^a k_\rho^2 J_0\left(k_\rho\rho\right)\cdot\sum_{elem}\left\{\begin{array}{c} e^{-k_\rho\left(z_i-z\right)} \\ \frac{\varepsilon_{r,earth}-1}{\varepsilon_{r,earth}+1}e^{-k_\rho\left(z_i+z\right)}\end{array}\right\}dk_\rho \\ \frac{1}{\omega\varepsilon}\int_0^a J_0\left(k_\rho\rho\right)\,I_v^{TM}\left(k_\rho,z,z_i\right)\,k_\rho^3 dk_\rho\end{array}\right\}. \quad \text{(C.12)}$$

The integrals of Equation (C.12) can be combined to give

$$E_z^{dip}\left(x,y,z,z_i\right)\simeq\frac{-I^{vert}\left(z_i\right)}{2\pi\omega\varepsilon}\sum_{elem}\left\{\begin{array}{c} 3\alpha_1^2\left(\alpha_1^2+\rho^2\right)^{-5/2}-\left(\alpha_1^2+\rho^2\right)^{-3/2} \\ \frac{\varepsilon_{r,earth}-1}{\varepsilon_{r,earth}+1}\left[3\alpha_2^2\left(\alpha_2^2+\rho^2\right)^{-5/2}-\left(\alpha_2^2+\rho^2\right)^{-3/2}\right] \\ \int_0^a k_\rho^2 J_0\left(k_\rho\rho\right)\cdot\sum_{elem}\left\{\begin{array}{c} \frac{k_\rho}{\omega\varepsilon}I_v^{TM}\left(k_\rho,z,z_i\right) \\ -e^{-k_\rho\left(z_i-z\right)} \\ -\frac{\varepsilon_{r,earth}-1}{\varepsilon_{r,earth}+1}e^{-k_\rho\left(z_i+z\right)}\end{array}\right\}dk_\rho\end{array}\right\}, \quad \text{(C.13)}$$

where $\alpha_1=z_i-z$ and $\alpha_2=z_i+z$. Note that the upper limit of the integral in Equation (C.13) is no longer infinite, though requiring *a* to be sufficiently large, and the additional terms not in the integral are algebraic. It is also apparent that the integral is accumulating differences between the exact and approximate value of $\frac{k_\rho}{\omega\varepsilon}I_v^{TM}\left(k_\rho,z,z_i\right)$, which would be advantageous when $z-z_i\approx 0$. Therefore, the computation of E_z^{dip} for observations near the dipole source can be facilitated by Equation (C.13).